Radon-induced surface contaminations in neutrinoless double beta decay and dark matter experiments

Luca Pattavina

N° d'ordre 27-2011
LYCEN – T 2011-15

Thèse en co-tutelle
avec l'Université Claude Bernard Lyon-I

présentée

Università degli Studi di Milano - Bicocca

École Doctorale de Physique et d'Astrophysique

pour l'obtention du

DIPLÔME de DOCTORAT
Spécialité : Physique des Particules

(arrêté du 7 août 2006)

par

Luca PATTAVINA

Radon-induced surface contaminations in neutrinoless double beta decay and dark matter experiments

Soutenue le 17 janvier 2011
devant la Commission d'Examen

Jury :	M.	E.	Previtali	Directeur de thèse
	Mme	C.	Augier	Directeur de thèse
	M.	F.	Piquemal	Rapporteur
	M.	C.	Bucci	Rapporteur
	M.	S.	Ragazzi	
	M.	B.	Ille	


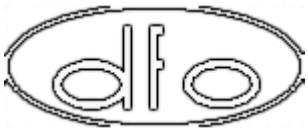

Università degli Studi di Milano – Bicocca


Université Claude Bernard Lyon 1

Radon-induced surface contaminations in neutrinoless double beta decay and dark matter experiments

Supervisor : Prof. Ezio PREVITALI

Prof. Corinne AUGIER

Thesis submitted for the degree of Ph.D.
by

Luca PATTAVINA

UNIVERSITÀ DEGLI STUDI DI MILANO-BICOCCA
UNIVERSITE CLAUDE BERNARD LYON 1

Radon-induced surface contaminations in neutrinoless double beta decay and dark matter experiments

Luca PATTAVINA

Supervisor:

Prof. Corinne AUGIER

Prof. Ezio PREVITALI

A thesis submitted for the
degree of Doctor of Philosophy in Physics and Astronomy
in the
Dipartimento di Fisica "G. Occhialini"
Institut de Physique Nucléaire de Lyon

17 January 2011

luca.pattavina@mib.infn.it

"L'essentiel est invisible pour les yeux."

Le Petit Prince, *Antoine de Saint Exupéry.*

to my looney family.

Contents

List of Figures

List of Tables

Chapter 1

Introduction

In experiments looking for rare events, like neutrinoless double beta decay (DBD) and dark matter search (DM), one of the main issue is to increase the experimental sensitivity through the material selection and the production, minimizing the background contribution coming from the materials used for the detector realization. Moreover the net reduction of the background produced by the bulk part of the apparatus has raised concerns about the background contribution coming from the surfaces.

Materials for the detectors sensitive parts are now realized with very low radioactive contaminants and a great effort was also put into the selection of all the *passive* materials used to realize the support structures of the detector. At the same time has become clear that all the surface treatments need to be performed under really strict constraints. A non-well defined surface treatment can induce an higher increase of the radioactive contamination on the surfaces compare to the bulk one. Many procedures and techniques were developed during the last years in order to remove and to minimize the presence of possible contaminants on detector surfaces. To succeed in this strategy a big effort was put in defining: all possible mechanisms that lead to surface contaminations, specific cleaning procedures which are able to reduce and control the surface radioactivity.

All the possible precautions that are taken during the detector assembly could be completely useless if a great attention is not paid to the environment in which the detector will be assembled. The presence in air and in gases of possible radioactive elements that can stick on the detector surfaces leading to a *recontamination* process that will vanish all the applied cleaning procedures.

As well known in air is normally detectable a net contamination of ^{222}Rn, an isotope that is produced by the ^{238}U chain. Radon is a noble gas, it can emanate from materials that are normally contaminated in ^{238}U and it will diffuse in the air. Depending on the building infrastructures, ventilation, material condition and material properties, the concentration of ^{222}Rn can change strongly from one configuration to another. To avoid, or better minimize, the recontamination process of the detector a specific design of the detector storage and assembly line must be defined. In particular all components must be stored in a clean environment where the presence of ^{222}Rn must be reduced as much as possible to avoid the possible sticking of radioactive atoms on detector material surfaces. A more complex task is the control of the radioactive contaminants in air during the detector assembly phase. Given these constraints the realization of a controlled environment is really tricky and it implies very strong efforts into the isolation of the air volume in which all the assembly procedures will be carried out. To evaluate the real requests of such effort a sizing of the contamination produced by such radioactive mechanisms must be done. The contamination induced by ^{222}Rn is very unsafe mainly because of one of its ^{210}Pb daughter, which has a long half-life time. This isotope has an half-life time of about 22 years and if it is deposited on the detector components, the background contribution induced will remain almost unchanged for all the data taking of the experiments. It is also very crucial to understand the mechanism through which the ^{210}Pb isotope will remain trapped on the material surfaces. It must be taken into account that the net contamination due to this isotope in air can be much higher with respect to the one given by ^{222}Rn. There are two ways in which this contamination is produced: one is linked to the continuous production of ^{210}Pb from the upper part of the decay chain without any decays on the time scale of few days: the typical timescale for a detector mounting. The other mechanism is due to the common presence of ^{210}Pb in the environment.

Cryogenic particle detectors that will be employed for CUORE (DBD) and EDELWEISS (DM) experiments are very sensitive to surface contaminations. These detectors are sensitive in the whole volume without a superficial dead layer that is commonly present in other type of detectors. This implies that such detectors are fully sensitive also on the detector surfaces and in this way they are affected by the contamination of surfaces which are directly facing the sensitive parts of the detector. In this configuration it is mandatory to control and to reduce all the possible radioactive contaminations on the detector surfaces.
To obtain the best background level a detailed analysis and research of the real

surface contamination sources must be carried out. In the specific the background induced by the presence of ^{222}Rn and its progeny in air can be caused directly by the Rn itself. The two different cases will imply different mechanisms in the particle sticking processes, so the understanding of these processes will show us the best way to minimize the Rn contribution to background. An important approach that was adopted to study the real contribution of Rn to surface contaminations is the realization of a Rn chamber where the concentration of the gas in air is artificially increased at a very high level. In this condition the exposure of materials to the contaminated environment will stress all the mechanisms of particle sticking, giving us the possibility to better analyze the main channels that will contribute to the surface contaminations. At the same time in the chamber were placed materials of different kinds and with different surface roughness helping us to better understand what characteristics of the exposed material will dominate in the contamination process. Identifying the correlation between the induced surface contamination and the Rn concentration in air multiplied by exposure time of the samples we will be able to scale the obtained data to the expected contamination induced on the detector during the assembly procedures. Moreover it is possible to define a threshold of Rn concentration that must not be exceeded in order to prevent a net excess in the final background of the experiment. There are also other peculiarities that are strictly related to the cryogenic detector performances; EDELWEISS Ge detectors with the help of the double read-out can greatly help in identifying the possible differences between the interaction of an alpha particle with respect to an electron/gamma particle. This is in principle very useful to identify the Rn induced background that is mainly dominated by the alpha particle released by the decay of the Rn daughters. The possibility to sizing also the contribution of degraded alpha particle in the energy range outside the typical alpha decay energy region (between 4 and 9 MeV) can show the diffusion mechanism that the stuck nuclei will have in the materials after a specific period of time. The diffusion problem is the main issue related to surface contamination due to possible misidentification of the source decay, mixing the background of surface alpha interactions with the bulk induced background produced by gamma rays. The direct comparison of the energy spectra obtained by CUORE and EDELWEISS detectors will give us the possibility to completely discover the various mechanism that generate the surface contaminations starting from the ^{222}Rn concentration in air, and to estimate how much a radon exposure can affect the background of such experiments.

In this thesis, first the physics of rare events (DBD and DM searches) and the

techniques adopted for the background suppression needed to look for this type of physics will be discussed (Chapter 2). In chapter 3 will be presented the tools used for these searches (bolometers), their working principle and the scientific motivation for the study of surface contaminations are studied. Chapter 4 is devoted to the review of the experimental technique used in the Cuoricino (CUORE) detectors. The problem of surface contamiantion as source of the background of the experiment is analyzed, in paticular the contamiantions induced by Radon are studied. Chapter 5 discusses the problem of surface contaminations in the frame of the EDELWEISS experiment, a thourough analysis about the contribution of alpha contaminations in the region of interest of the WIMP search is carried out.

Chapter 2

Physics of rare events

Many open questions in modern physics can only be further faced with techniques able to filter a weak signal out of background and noise. In this case spurious counts resulting, from environmental radioactivity, from intrinsic contamination of the target, detector and shielding material, from airborne activity (e.g. Radon and Krypton), from cosmic rays, or from neutrons can obscure the signal counts in the region of interest.

2.1 Rare events experiments

Many advances have been made in experiments searching for solar neutrinos, double beta decay (**DBD**) and dark matter (**DM**) particles. Here, events are as low as a few per day or even a few per year and lie in different energy regions, from few keV up to few MeV. One common scientific motivation in this class of experiments is the determination of neutrino properties, and the real nature of dark matter.

Interest in double-beta decay (**DBD**) has seen a significant renewal in recent years after evidences for neutrino oscillations were obtained from the results of atmospheric, solar, reactor and accelerator neutrino experiments [21–25]. These results are an impressive proof that neutrinos have a non-zero mass. However, the experiments studying neutrino oscillations are not sensitive to the nature of the neutrino (*Dirac* or *Majorana*) and provide no information on the absolute scale of the neutrino masses, since they are sensitive only to the difference of the masses, Δm^2.

The detection and study of neutrinoless double beta decay (DBD0ν)may clarify the following problems of neutrino physics [26–28]: (i) lepton number non-conservation, (ii) neutrino nature, (iii) absolute mass scale (a measurement or a limit on different neutrino flavors), (iv) the type of neutrino hierarchy (normal, inverted or quasi-degenerate) and (v) CP violation in the lepton sector (measurement of the Majorana CP-violating phases).

The DBD0ν is a second-order weak process in which a nucleus changes its atomic number by two units. Being a very rare process the experimental search for this decay demands a large emitter mass operating in ultra low-background conditions. We look for a *Gaussian-shaped* peak, of a width of about the energy resolution of the detector, at the transition energy of the decay ($Q_{DBD0\nu}$), in the two-electrons summed energy spectrum. Current experimental limits on the half-life of this process range between 10^{21} and 10^{25} years, depending on the source isotope and on the type of detector.

At the same time significant care is dedicated to the problem concerning the real Universe composition. In fact astronomical observations, of the recent decades, unquestionably testify to the fact that the Universe is composed by just a small portion of visible matter, the remaining amount is considered as *dark matter* (manifesting itself only via gravitational interaction) and dark energy (also known as the vacuum energy).

The dark matter enigma has been one of the most intriguing problems of fundamental physics of our days, and the scientific picture of the world in the 21th century may signicantly depend on solving this problem. It has obviously stimulated the development of unique experimental technologies of particle detection and identication [29, 30].

The very convincing astrophysical experimental evidences in favour of the existence of DM known so far are the rotation curve measurement results for objects in spiral galaxies and observation of gravitational lensing effects for distant galaxies caused by galaxy clusters located between them and an observer. These evidences have prompted an intense search for dark matter candidates [31, 32]. Here, low-background detectors with an energy threshold as low as possible are needed in the keV range.

2.2 The DBD and DM quest

Compared to solar neutrino experiments, DBD and DM experiments are still in smaller scale. Both the neutrinoless DBD and DM experiments are exclusion experiments since up to now no positive evidence[1] has been observed in either class of experiments.

The background for a certain energy region from which the exclusions are derived is given as $\mathbf{events{\cdot}keV^{-1}{\cdot}kg^{-1}{\cdot}y^{-1}}$. Since the source of background (unavoidable and avoidable) is still too big with respect to the signals that we look for, this unit of measurement allows us to compare the discovery potential of different experiments. DBD0ν, if it exists, can produce a Gaussian peak, that is more easily recognized than the continuous distribution from nuclear recoil of WIMPs. Due to the type of signal produced by WIMP recoils, different units for measuring the discovery potential can be adopted, as event$\cdot$kg$^{-1}\cdot$y^{-1}, where the normalization of the region of interest is not strictly needed.
In the next section we will have a closer look to the detection principle of DBD0ν and DM.

2.2.1 DBD physics

Double beta decay is an extremely rare nuclear transition from a nucleus (A,Z) to its isobar (A,Z+2). The transition may occur via a Standard Model allowed process in which two electron antineutrinos are emitted along with two electrons: (A,Z) $\rightarrow$ (A,Z+2) + $2e^-$ + $2\overline{\nu}_e$. This decay mode, known as two-neutrino double beta decay (**DBD2ν**), can be thought of as two simultaneous beta decay. The expected rate for **DBD2ν** was first calculated by Goeppert-Mayer in 1935 [34], and the decay has now been observed in many nuclides (see Table 2.1). Double beta decay half-lives for nuclei that undergo the process are very long, since the decay is of the second order in the weak interaction.

In principle, a nucleus (A,Z) can decay by double beta decay as long as the nucleus (A,Z+2) is lighter. However, if the nucleus can also decay by single beta decay to (A,Z+1), the branching ratio for the double beta decay will be so small that it is practically impossible to observe the double beta decays in an experiment due to the overwhelming background rate from single beta decays.

[1] Accepted by the all the scientific community. Special care should be given to [17] and [33].

TABLE 2.1: DBD2ν half-life values for double beta decaying isotopes [15, 16].

Nuclide	$T_{1/2}^{DBD2\nu}$ [y]
^{48}Ca	$4.2^{+2.1}_{-1.0} \times 10^{19}$
^{76}Ge	$(1.5\pm0.1) \times 10^{21}$
^{82}Se	$(9.6\pm1.0) \times 10^{19}$
^{96}Zr	$(2.35\pm0.21) \times 10^{19}$
^{100}Mo	$(7.11\pm0.54) \times 10^{18}$
^{116}Cd	$(2.8\pm0.3) \times 10^{19}$
^{128}Te	$(1.9\pm0.4) \times 10^{24}$
^{130}Te	$(6.9\pm1.3) \times 10^{20}$
^{136}Xe	$\geq 8.1 \times 10^{20}$
^{150}Nd	$(9.1\pm0.7) \times 10^{18}$

Therefore, candidate nuclei for experimental detection of double beta decay are *even-even* nuclei that, due to the nuclear pairing force [35], are lighter than the *odd-odd* $(A,Z+1)$ nuclei, making single beta decay kinematically forbidden. This situation is shown schematically in Fig 2.1.

If the neutrinos are Majorana fermions, there is an additional decay channel: $(A,Z) \rightarrow (A,Z+2) + 2e^-$, with no neutrinos (antineutrinos) emission in the final state. This decay mode (**DBD0ν**) has still never been observed, except for the controversial claim of part of the Heidelberg-Moscow collaboration [17]. The first calculation of the rate for DBD0ν was performed by Furry [36] and yielded to a much faster rate for the disintegration, compared to the DBD2ν. This misleading result was due to the fact that, at that time the chiral nature of weak interaction was not yet known so a severe suppression of DBD0ν was not incorporated in the calculations.

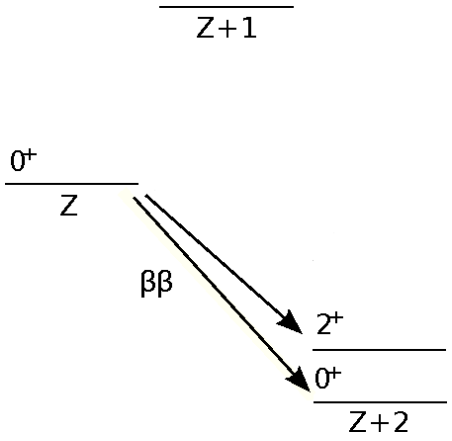

FIGURE 2.1: Diagram of energy levels involved in DBD.

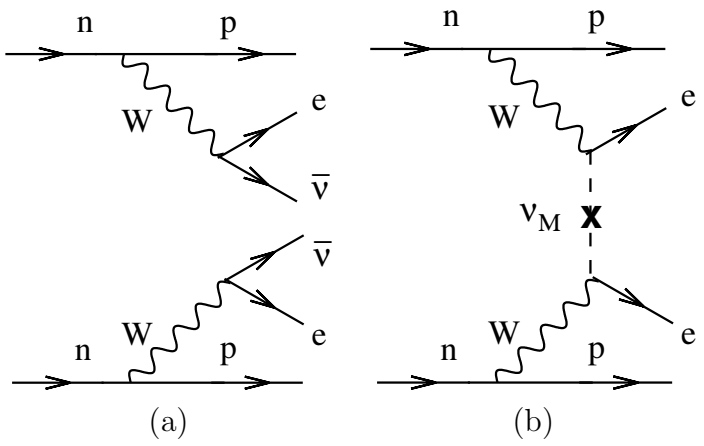

FIGURE 2.2: Feynman diagrams for (a) two neutrino double beta decay and (b) neutrinoless double beta decay

Neutrinoless double beta decay is forbidden by the Standard Model since it manifestly breaks lepton number conservation by two units. Of course lepton number conservation is broken anyway if neutrinos are Majorana particles. If we take a look to the Feynman diagrams for DBD2ν and DBD0ν (see Fig. 2.2) we can notice that in order to observe the DBD0ν a minimum requirement must be fulfilled: the neutrino must be a massive Majorana particle. One can think of the virtual neutrino in this diagram as being produced as an antineutrino (equal to a neutrino, since these are Majorana particles) at one vertex and absorbed as a neutrino at the other vertex. In addition to the Majorana equivalence (neutrino $\equiv$ antineutrino), a non-zero neutrino mass is required to flip the helicity since antineutrinos are right-handed and neutrinos are left-handed. The helicity flip and the smallness of the neutrino mass cause the rate of DBD0ν to be much lower than the rate of DBD2ν.

The DBD0ν rate is given, to a good approximation by:

$$\frac{1}{T_{1/2}^{DBD0\nu}} = G_{0\nu}(Q,Z)|M^{0\nu}|^2 m_{\beta\beta}^2 \tag{2.1}$$

where $G_{0\nu}$(Q,Z) is the two-body phase-space factor including coupling constants, $|M^{0\nu}|$ the nuclear matrix element of the transistion and $m_{\beta\beta}$ is the effective Majorana mass, defined as:

$$m_{\beta\beta} \equiv \left| \sum_{i=1}^{3} U_{ei}^2 \, m_i \right| \tag{2.2}$$

TABLE 2.2: Half-life limits for neutrinoless double beta decaying isotopes. [1] Some members of the Heidelberg-Moscow collaboration made a controversial claim [17]

Nuclide	Q-value [keV]	$T_{1/2}^{DBD0\nu}$ [y]	Reference
^{48}Ca	4271 ± 4	$> 1.4 \times 10^{22}$	[37]
^{76}Ge	2040 ± 1	$> 1.9 \times 10^{25}$	[38] [1]
^{76}Ge	2040 ± 1	$> 1.13 \times 10^{25}$	[39]
^{82}Se	2995 ± 6	$> 1.0 \times 10^{23}$	[40]
^{96}Zr	1145 ± 3	$> 1.0 \times 10^{21}$	[41]
^{100}Mo	3034 ± 3	$> 4.6 \times 10^{23}$	[40]
^{116}Cd	2802 ± 4	$> 1.7 \times 10^{23}$	[42]
^{130}Te	2527 ± 1	$> 3.2 \times 10^{24}$	[43]
^{136}Xe	2479 ± 8	$> 1.2 \times 10^{24}$	[44]
^{150}Nd	3367 ± 2	$> 1.8 \times 10^{18}$	[45]

where U_{ei} represents the Pontecorvo-Maki-Nakagawa-Sakata mixing matrix that describes the mixing between the neutrino mass eigenstates and the neutrino flavor eigenstates, and m_i are the different neurino mass eigenvalues. The information concerning the neutrino mass is contained in $m_{\beta\beta}$. The phase-space factor $G_{0\nu}$(Q,Z) is calculable but the evaluation of the nuclear matrix element is a challenging problem in nuclear theory.

Experiments attempt to measure $T_{1/2}^{DBD0\nu}$, and in the absence of a signal, set a lower limit. Combining the measurements and the calculations, the value of $m_{\beta\beta}$ is deduced or an upper limit is set. Current experimental limits are listed in Table 2.2.

If neutrinos are Majorana particles, measuring or constraining the effective Majorana mass provides information on the neutrino mass scale and hierarchy. This is possible because there is a relationship between the effective Majorana mass and the mass of the lightest neutrino. This relationship depends on whether the hierarchy is normal or inverted because the lightest neutrino mass eigenstate depends on which hierarchy is in nature (see Fig. 2.3).

If we take a closer look to the definition of the effective neutrino mass (equation 2.2), in the case of normal hierarchy mass with m_1 as the lightest mass eigenvalue,

we find [1]:

$$
\begin{aligned}
m_{\beta\beta} &\equiv \left| U_{e1}^2\, m_1 + U_{e2}^2\, m_2 + U_{e3}^2\, m_3 \right| && (2.3)\\
&= \left| U_{e1}^2 m_1 + U_{e2}^2 \sqrt{\Delta m_{12}^2 + m_1^2} + U_{e3}^2 \sqrt{\Delta m_{13}^2 + m_1^2} \right| && (2.4)\\
&= \Big| \cos^2\theta_{12} \cos^2\theta_{13}\, e^{i\alpha_1}\, m_1 + \sin^2\theta_{12} \cos^2\theta_{13}\, e^{i\alpha_2} \sqrt{\Delta m_{12}^2 + m_1^2} && (2.5)\\
&\quad + \sin^2\theta_{13}\, e^{-2i\delta} \sqrt{\Delta m_{13}^2 + m_1^2} \Big| ,
\end{aligned}
$$

where α_1 and α_2 are Dirac phases and δ is a Majorana phase. A similar equation is easily obtained for the inverted mass hierarchy in which m_3 is the lightest mass eigenvalue. Plugging in the measured values of the neutrino mixing angles and mass-squared differences (see Table 2.3) a value for $m_{\beta\beta}$ is obtained for each value of the lightest neutrino mass, m_1 for the normal hierarchy or m_3 for the inverted hierarchy, and for a given set of values for the phases (α_1, α_2 and δ). Fig. 2.4 shows the range of allowed values for the effective mass hierarchy for each value of the lightest neutrino mass, obtained by allowing the unknown phases to vary over their possible values from 0 to 2π.

The most significant sources of uncertainties in calculating the neutrino mass value (or limit) are the nuclear matrix elements. In fact the nuclear matrix element, $M^{0\nu}$, is affected by important theoretical uncertainties. This problem could be solved with a detailed description to the second-order of the weak transition

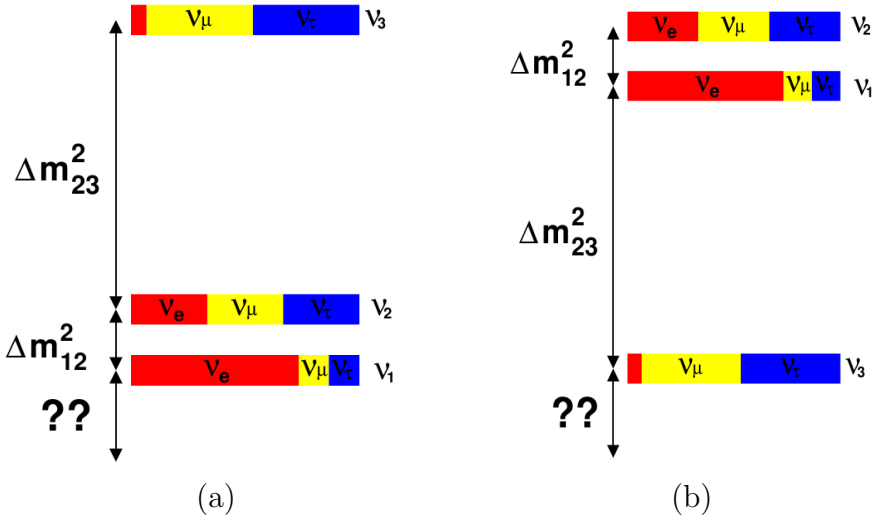

FIGURE 2.3: Neutrino mass eigenstates for (a) normal and (b) inverted hierarchy.

TABLE 2.3: Measured values of neutrino mixing parameter [18].

Parameter	Best Value	2σ C.L.
Δm^2_{12}	7.6×10^{-5} eV^2	$(7.3\text{-}8.1) \times 10^{-5}$ eV^2
Δm^2_{13}	2.4×10^{-3} eV^2	$(2.1\text{-}2.7) \times 10^{-3}$ eV^2
$\sin^2\theta_{12}$	0.32	0.28-0.37
$\sin^2\theta_{23}$	0.50	0.38-0.63
$\sin^2\theta_{13}$	0.007	≤ 0.033

from the parent to the daughter nucleus. Furthermore, the importance of the nuclear matrix element is strictly connected to the fact that, even if the observation of neutrinoless double beta decay of an isotope is enough to make the claim of the discovery, the comparison and confirmation with other isotopes is needed. Different isotopes have different Q-value and different $M^{0\nu}$ (see Fig. 2.5), so a precise evaluation of these parameters allow an exhaustive comparison analysis.

There are two basic approaches for the evaluation of nuclear matrix elements (**NME**): the quasi-particle random phase approximation (**QRPA**) and the nuclear shell model (**NSM**). In principle NSM calculations are more reliable, as they

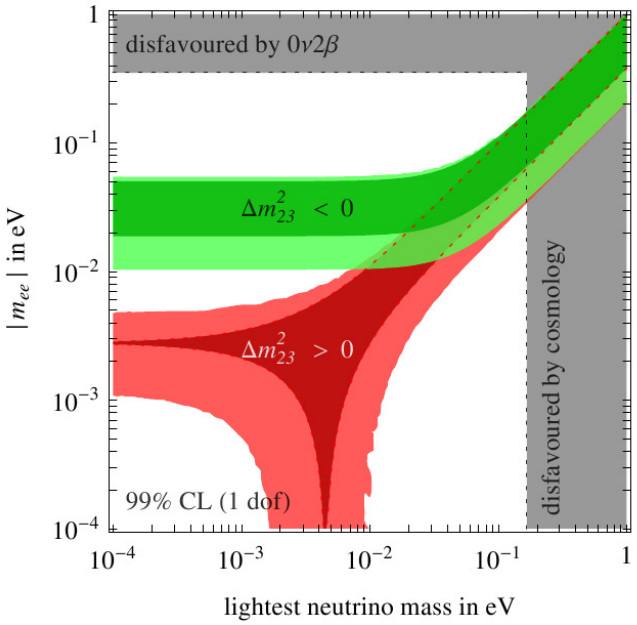

FIGURE 2.4: 99% C.L. expected ranges of effective Majorana mass as function of the lightest neutrino mass. The red region corresponds to normal hierarchy and the green one to the inverted hierarchy. The darker regions show how the ranges would shrink if the present best-fit values of oscillation parameters were confirmed with negligible error. The grey bands represent the parameter space that is excluded by current double beta decay experiments and by cosmological observations [1].

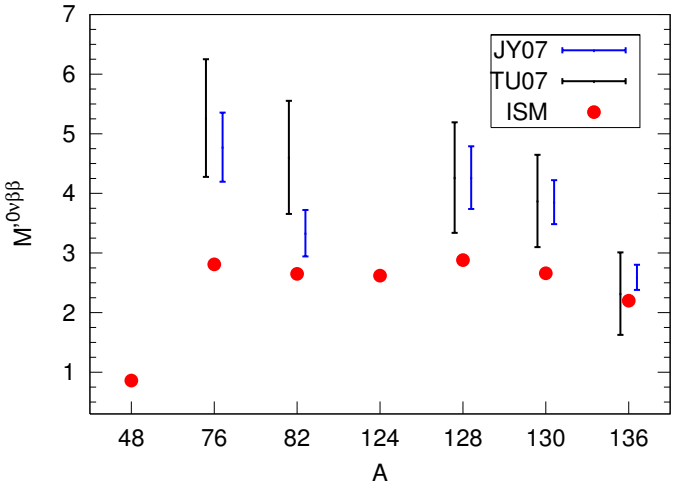

FIGURE 2.5: Nuclear matrix element calculations for several DBD0ν isotopes using QRPA (black and blue bars) and NSM (red dots) [2].

require few approximations, however such calculations are computationally intensive, which places a practical limit on the number of single-particle valence states that can be considered. For this reason the QRPA approach is usually preferred expecially for nuclei of large Z. QRPA calculations use a larger valence space with respect to NSM, but the interaction strengths are parametrized, and only a subset of the possible configurations are taken into account.

2.2.2 DBD0ν detection

Direct counting experiments search for double beta decay by measuring the sum of the electron energies. The total decay energy (Q-value) is shared among all the final state particles. The amount of energy which is shared with the daughter nucleus is negligible, due to mass considerations. In the spectrum of the summed electrons, the DBD2ν appears as a continuum from 0 up to the Q-value of the decay, since the energy is shared among all the particles emitted. In the DBD0ν electrons carry away almost all the decay energy. The energy given to the recoil energy is negligible, thus this disintegration produces a monocromatic line at the Q-value in the spectrum considering m_ν much smaller than m_e (see Fig. 2.6).

The two principal requirements of an experiment designed to observe this peak are: a very low-background level and the capability to identify the electrons and to measure the energies with high energy resolution. The identification of the various types of events (e.g. electrons, positrons, alpha) helps in understanding not only the signal but also the background sources. A low-background level is required to

make a statistically significant discovery of DBD0ν, which is expected to be very small considering the limits set by previous experiments. A high energy resolution prevents the tail of the DBD2ν to leak into the region of interest and burying the small signal of the DBD0ν. Thus an improvement in the energy resolution directly reduces the background level by narrowing the region of interest in which the signal is expected.

The sensitivity of an experiment is an important parameter which allows comparing the discovery potential of an experiment considering the variables that describe the detector. The sensitivity is defined as the half-life corresponding to the minimum number of signal events observable above the background at a given statistical significance. For DBD experiments it can be expressed as:

$$S^{0\nu}(n_\sigma) = C^{te}\frac{\eta}{A}\cdot N_a\cdot\epsilon\cdot\sqrt{\frac{M\cdot t}{B\cdot\Gamma}} \tag{2.6}$$

where ϵ is the detection efficiency, N_a the Avogadro number, η is the isotopic abundance of the candidate nucleus in the source, A the atomic mass number, M is the total detector mass, t is the live time of the experiment, Γ is the detector energy resolution in the region of interest and B is the background expressed in events·keV^{-1}·kg^{-1}·y^{-1}. So, in order to maximize the sensitivity one of the main goal of DBD experiments is to reduce the background in the region of interest as much as possible. This is done through a suitable choice of the candidate nucleus. Isotopes with high Q-value are preferred for several reasons. First the background from natural radioactivity decreases with increasing Q. An important energy peak

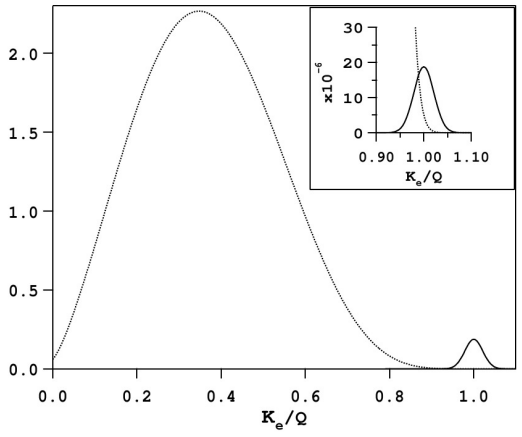

FIGURE 2.6: Illustration of the summed kinetic energy of the two electrons, K_e emitted in the case of DBD2ν (dotted line) and DBD0ν (solid line). The small upper section shows how a poor energy resolution of the detector can modify the shape of the DBD0ν monocromatic peak.

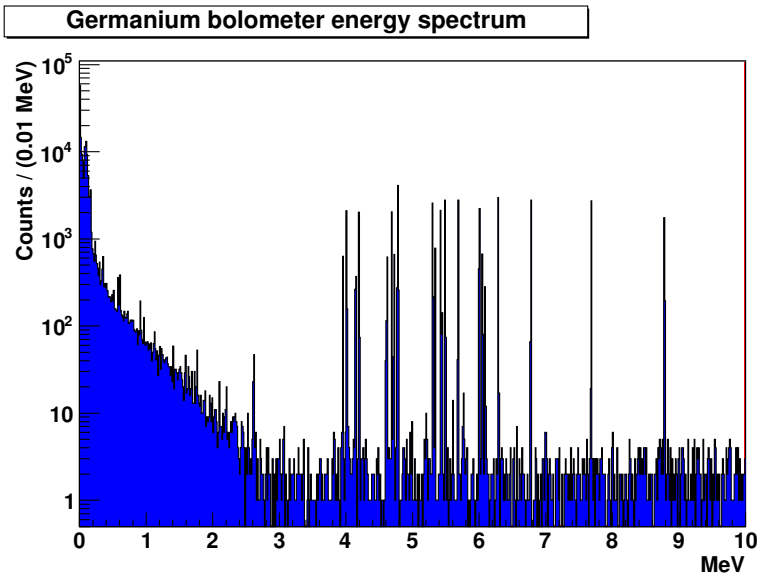

FIGURE 2.7: Simulated energy spectrum of a Germanium bolometer with a source of ^{238}U and ^{232}Th.

is the gamma emitted by the ^{208}Tl (element of the Thorium decay chain), at 2615 keV, which is one of the highest gamma line from natural radioactivity. Isotopes with Q-value above 2615 keV and lower than 4 MeV (alpha region) benefit of a much lower background level (see Fig. 2.7). At the same time isotopes with high Q-values imply larger phase spaces and the detector becomes less efficient for detecting the DBD decay products.

2.2.3 DM physics

The first interest for a matter which can only be observed by its gravitational effects dates back to 1915, when Öpik studied the dynamical matter density in the Solar vicinity [46]. The definition of this type of matter appears for the first time in 1933 and it has been defined as *dark matter* by Zwicky [47]. Since then astrophysical evidences about the presence of a *mass excess* compared to the visible fraction of matter have grown in number. Let's have a look at the most significant ones.

Evidence at galactic scale

The most direct evidence for DM, at galactic scales, comes from the observation of the rotation curves of galaxies and of cluster of galaxies. A simple newtonian

evaluation of the circular velocity of a galaxy is expected to be:

$$v_c(r) = \sqrt{\frac{GM(r)}{r}} \tag{2.7}$$

where:

$$M(r) \equiv 4\pi \int \rho(r) r^2 dr \tag{2.8}$$

and $\rho(r)$ is the mass density profile, which should be falling as $1/\sqrt{r}$ outside the optical disc. Experimental data (see Fig. 2.8) show that $v_c(r)$ is approximately constant out of the optical disc. This implies the existence of a halo with $M(r) \propto r$ and $\rho(r) \propto 1/r^2$.

Another evidence, at galaxy scale, is the dark matter content in the inner halos of massive disk galaxies. It has been argued that barred galaxy [48] can not contain substantial amounts of dark matter out to the outermost extent of the observed bars, otherwise the rapidly rotating bars would have slowed down due to dynamical friction on the dark matter. One counterargument is the assertion that bars may be dynamically young systems and hence poor dynamical probes. Despite the uncertainties of the form of the innermost region of galaxies, rotation curves of disk galaxies provide strong evidence for the existence of a spherical dark matter halo. In any case the total amount of DM present is difficult to quantify.

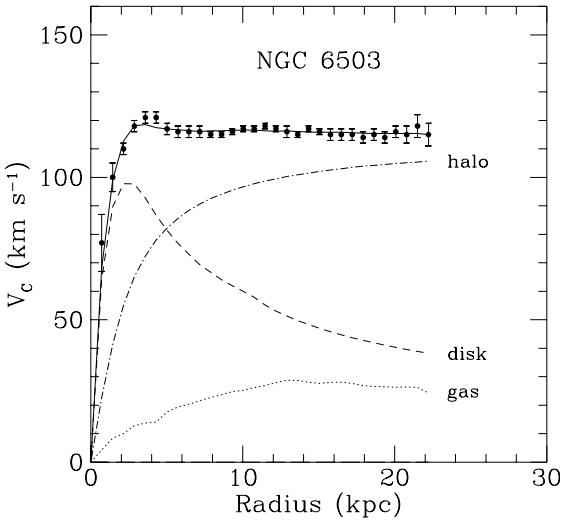

FIGURE 2.8: Rotation curve of the galaxy NGC 6503. The dotted, dashed and dash-dotted lines are respectively the expected contribution of gas, disk and dark matter [3].

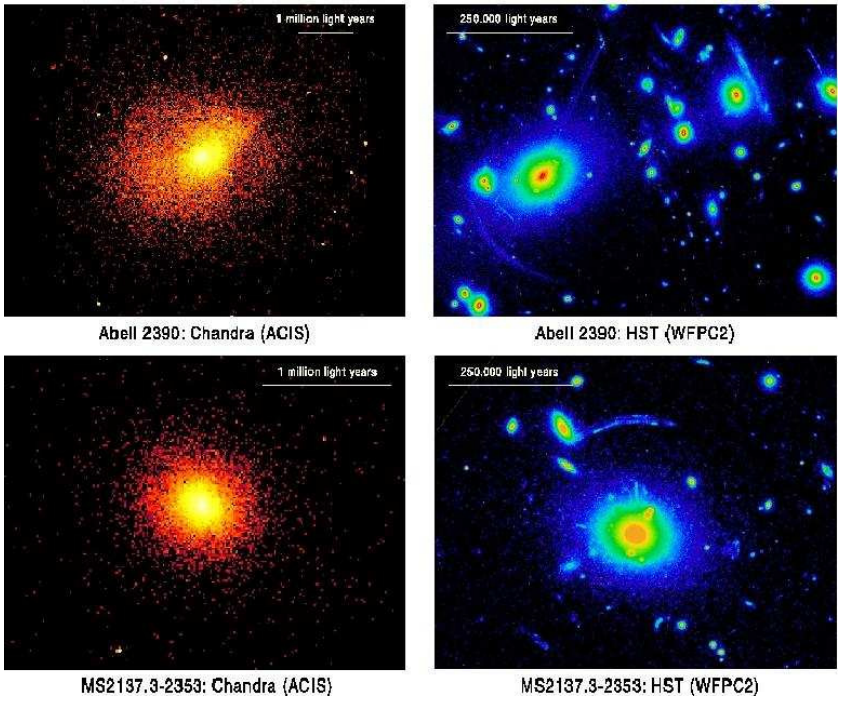

FIGURE 2.9: Chandra X-ray (left) and Hubble Space Telescope Wide Field Planetary optical (right) images of Abell 2390 (z=0.230) and MS2137.3-2353 (z=0.313). Note the clear gravitational arcs in the Hubble images due to the gravitational lensing effect. [4].

Evidence at galaxy cluster scale

In 1933, Zwicky inferred, from measurements of the velocity dispersion of galaxies in the Coma cluster, a mass to light ratio exceeding the ratio in the solar neighborhood. The mass of a cluster can be determined via several methods: by weak gravitational lensing, by studying the profile of X-ray emission, and many others. While the value of the temperature (and hence the light) can be estimated through thermodynamical and baryonic mass profile consideration. Unfortunately the disparity obtained between the theoretical temperature and the corresponding observed temperature suggests the existence of a substantial amount of dark matter in clusters.

These conclusions can be checked with estimations from gravitational lensing data (see Fig. 2.9). Following Einstein's theory of general relativity, light propagates along geodesics which deviate from straight line when passing near intense gravitational fields. The distortion of the images of background objects due to the gravitational mass of a cluster can be used to infer the shape of the potential and thus the mass of the cluster.

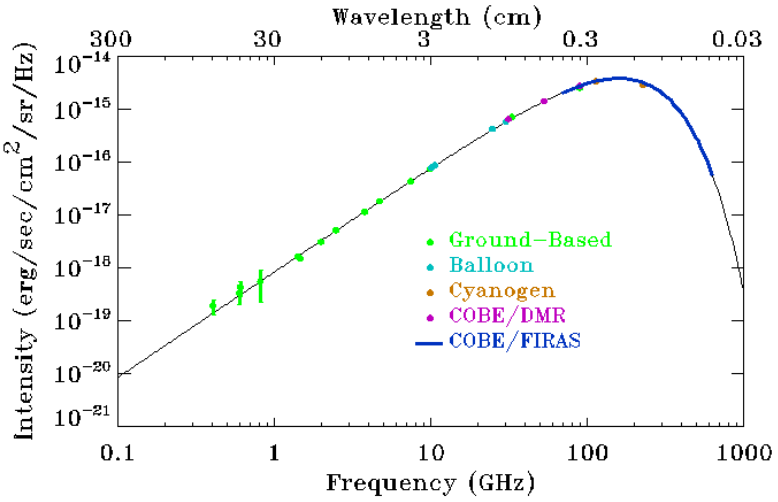

FIGURE 2.10: Intensity of the cosmic microwave background (colored points) compared to a perfect blackbody curve (thin black line) [5].

Evidence at cosmological scale

The galactic and intergalactic observations do not allow evaluating the amount of dark matter in the Universe. On the other side, this quantity can be determined through observations concerning the Cosmic Microwave Background (**CMB**). The CMB is mainly composed of photons produced when the Universe was about 300,000 years old (when T = 3,000 K). If we are able to detect those photons it is possible to obtain a picture of the Universe at that period. The CMB follows with extraordinary precision the spectrum of a black body corresponding to a temperature of $T = 2.726$ K (not anymore 3,000 K due to the Universe expansion) (see Fig. 2.10). Considering the actual Universe temperature it is possible to derive the cosmic photon abundance:

$$\Omega_r h^2 = 2.45 \times 10^{-5} \approx 0. \tag{2.9}$$

Looking at $\Omega_r h^2$, it is possible to state that at big scale the CMB is homogeneous and isotropic better than 1 part over 10^5. This level of anisotropy provides information about the fluctuations that existed at the matter and radiation decoupling epoch. The satellite **WMAP** (Wilkinson Microwave Anisotropy Probe) analyzed and measured with great precision these anisotropies, giving us a full sky map of the cosmic microwave background (see Fig. 2.11). From WMAP data [49] the

following results for the abundance of baryons and matter were found:

$$\Omega_b h^2 = 0.0224 \pm 0.0009 \quad (2.10)$$

$$\Omega_M h^2 = 0.135^{+0.008}_{-0.009}. \quad (2.11)$$

These values allow obtaining the abundance of non-baryonic dark matter in the Universe:

$$\Omega_{DM} = 0.22 \pm 0.02 \qquad @ \text{ C.L. } 68\%. \quad (2.12)$$

The WMAP results concerning the cosmic microwave background are in agreement with the ones obtained from other previous measurements. The results can be summarized as follows:

- total cosmological density of the Universe ∼1;
- the Universe is made out of ∼27% of matter and the rest is considered *dark energy*;
- only 4% of the Universe is made of baryonic matter;

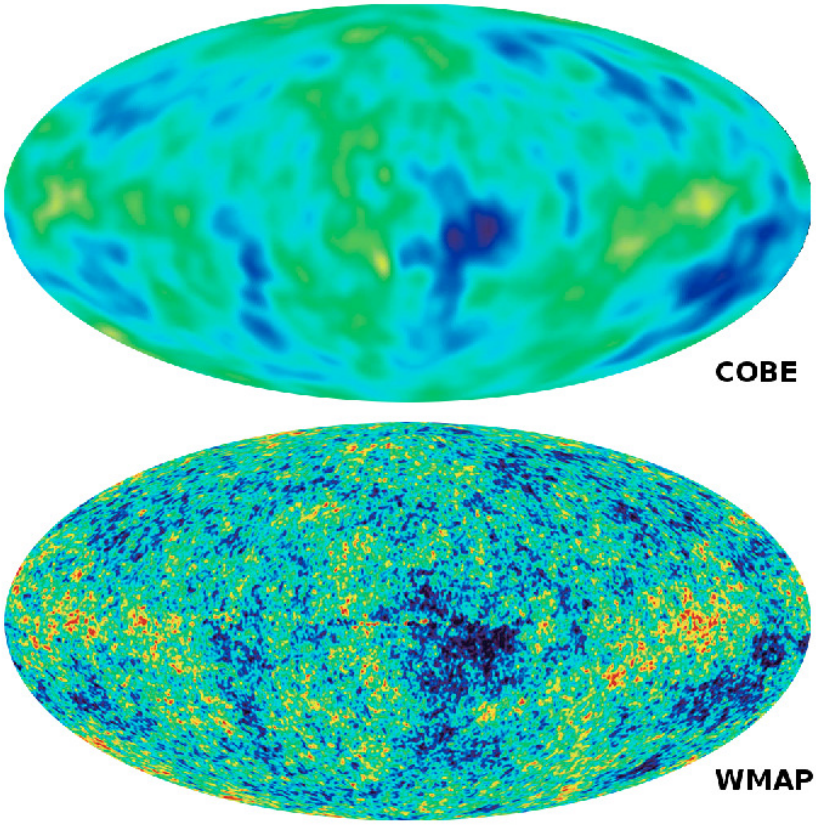

FIGURE 2.11: CMB temperature fluctuations: comparison between COBE and WMAP satellite.

- about 0.5% of the Universe is composed by luminous matter;
- the non-baryonic matter represents ∼23% of the Universe.

2.2.4 Dark matter candidates

The evidence for non-baryonic dark matter is compelling at all observed astrophysical scales. It is therefore natural to ask *what is the dark matter made of?* In this section we will see some of the most interesting dark matter candidates.

There are two types of non-baryonic dark matter: hot dark matter (**HDM**) and cold dark matter (**CDM**). The difference between these two categories lies in the speed of the particles at the moment of the matter-light decoupling. HDM particles were relativistic while CDM were not.

Hot dark matter

The main candidate for non-baryonic hot dark matter is the *neutrino*. The neutrino density in the Universe is high and the rate production in the early Universe was intense. The overall contribution to the HDM is strictly connected to the neutrino mass. In fact the more the mass of the neutrino is big the larger is its contribution to the HDM. In any case, since a precise measurement of the neutrino mass has not still be performed, the lower limit for the neutrino relic density is given by WMAP results [49]: $\Omega_\nu h^2 < 0.0067$ at 95% confidence level.

Cold dark matter

The cold dark matter candidates should be divided into two categories. The first class consists of particles produced through non-thermic processes:

- **Axions** [50]: first a Goldstone pseudo-boson, used to reduce CP violation in the strong interactions. The experimental and cosmological constraints set a range of masses for the axions of: 10^{-6}-10^{-3} eV·c^{-2}.
- **Wimpzillas** [51]: super-heavy candidate for cold dark matter with a mass of about 10^{10} GeV·c^{-2}.

while the second were in thermal equilibrium at the decoupling moment, these are generally named WIMPs (Weakly Interactive Massive Particles). As specified by the name these are weakly interactive heavy particles. They are stable particles whose relic amount is still present in the Universe. These candidates are often divided in subcategories:

- **LKP** (Lightest Kaluza-Klein Particles) [52]: introduced in dark matter models in the extra dimensions sector. They have masses within 600 GeV·c^{-2} and 1.5 TeV·c^{-2}.
- **Scalar particles** [53]: with a mass range between 1 MeV·c^{-2} and 100 MeV·c^{-2}.
- **Supersymmetric candidates** [54]: particles in models of R-parity conserving supersymmetry (Neutralino, Sneutrino, Gravitino).

2.2.5 Dark matter detection

WIMPs are regarded as the most natural dark matter candidate. They give an important contribution to the overall Universe density, furthermore they can also cluster gravitationally with ordinary matter in the galactic halo. In particular they would be present in our own galaxy, raising the hope of detecting relic WIMPs directly, through elastic scattering of WIMPs off target nuclei or indirectly, looking for signals produced by WIMP-WIMP annihilation.

Direct detection experiments appear today as one of the most promising techniques to detect dark matter particles. The idea is very simple: if the galaxy is filled with WIMPs, then an amount of them should pass through the Earth, making possible to look for the interaction of such particles with ordinary matter.

The key ingredients for the calculation of the signal in direct detection experiments [32] are the density and the velocity distribution of WIMPs in the solar neighborhood and the WIMP-nucleon scattering cross section, $\sigma_{N\chi}$. With this information, it is then possible to evaluate the rate of events expected (e.g. WIMP-nucleon scattering events) per time unit and per detector mass unit in an experiment.

This rate is given by:

$$dR = N\sigma_{N\chi}\, v\, n_{\chi}, \tag{2.13}$$

where

$$N = \frac{\text{Detector mass}}{\text{Atomic mass}} \tag{2.14}$$

is the number of target nuclei in the detector, and

$$n_\chi = \frac{\text{WIMP energy density}}{\text{WIMP mass}} = \frac{\rho_\chi}{M_\chi} \tag{2.15}$$

is the local WIMP density.

In the case of *zero momentum transfer*: $\sigma = \text{constant} = \sigma_0$, then:

$$R = N_0\,\sigma_{0N\chi}\int_0^{v_{esc}} v\,dn = N_0\,\sigma_0\,n_{0\chi}\,\langle v\rangle. \tag{2.16}$$

We define R_0 as the event rate per mass unit for a zero Earth velocity relative to the dark matter distribution (v_E) and an infinite local Galactic escape velocity (v_{esc}) [2]:

$$R_0 = \frac{2}{\pi^{\frac{1}{2}}}\,N_0\,\frac{\rho_\chi}{M_\chi}\,\sigma_0\,v_0; \tag{2.17}$$

and merging this equation with 2.16 leads to:

$$R = R_0\,\frac{\pi^{\frac{1}{2}}}{2}\,\frac{\langle v\rangle}{v_0} \tag{2.18}$$

$$= R_0\,\frac{k_0}{k}\,\frac{1}{2\pi v_0^4}\int v\,f(\overline{v},\overline{v}_E)\,d^3v, \tag{2.19}$$

where k is a normalization constant:

$$k = \int_0^{2\pi} d\phi \int_{-1}^{1} d(\cos\theta)\int_0^{v_{esc}} f(\overline{v},\overline{v}_E)\,v^2\,dv. \tag{2.20}$$

We shall use this result in a differential form:

$$dR = R_0\frac{k_0}{k}\frac{1}{2\pi v_0^4}\,v\,f(\overline{v},\overline{v}_E)\,d^3v. \tag{2.21}$$

The recoil energy of a nucleus, of mass M_N, struck by a dark matter particle of kinetic energy:

$$E = \frac{1}{2}\,M_\chi\,c^2\,\left(\frac{v}{c}\right)^2 \tag{2.22}$$

and scattered at angle θ is given by:

$$E_R = r\,E\,\frac{(1-\cos\theta)}{2} \tag{2.23}$$

[2] We assume a Maxwellian dark matter velocity distribution $f(\overline{v},\overline{v}_E) = e^{-\frac{(\overline{v}+\overline{v}_E)}{v_0^2}}$.

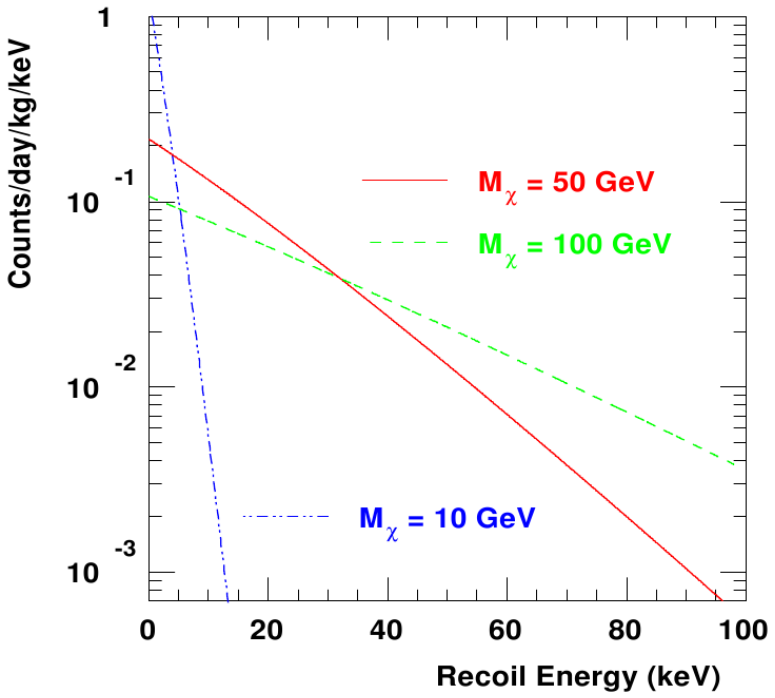

FIGURE 2.12: Theoretical WIMP spectrum for a Germanium detector for different WIMP masses. The following values for the galactic halo have been setted: $\rho_0 = 0.3$ GeV·cm^{-3} and $\overline{v}_E = 270$ km·s^{-1} and $\sigma_{\chi-N} = 7 \times 10^{-6}$ pb.

where

$$r = 4\,\frac{M_\chi\, M_N}{(M_\chi + M_N)^2}. \tag{2.24}$$

Assuming the scattering is isotropic, so that recoils are uniformly distributed in E_R, the differential event rate per recoil energy is:

$$\frac{dR}{dE_R} = \int_{E_{min}}^{E_{max}} \frac{1}{rE}\, dR(E) = \frac{1}{r\,E_0} \int_{v_{min}}^{v_{max}} \frac{v_0^2}{v^2}\, dR(v) \tag{2.25}$$

where $E_{min} = \frac{E_R}{r}$ is the smallest particle energy which can give a recoil energy E_R; $E_0 = \frac{M_\chi v_0^2}{2}$; and v_{min} is the dark matter particle velocity corresponding to E_{min}:

$$v_{min} = \sqrt{\frac{2E_{min}}{M_\chi}} = \sqrt{E_R}\, r\, E_0\, v_0. \tag{2.26}$$

So using 2.21, we have:

$$\frac{dR}{dE_R} = \frac{R_0}{r\,E_0}\,\frac{k_0}{k}\,\frac{1}{2\pi v_0^2} \int_{v_{min}}^{v_{max}} \frac{1}{v}\, f(\overline{v}, \overline{v}_E)\, d^3v. \tag{2.27}$$

This is the WIMP off nuclei scattering rate as a function of the recoil energy, also known as the WIMP spectrum (see Fig. 2.12). For practical purposes the

previous equation is well approximated by:

$$\frac{dR}{dE_R} = c_0 \frac{R_0}{r\,E_0}\, e^{-\frac{c_1\,E_R}{r\,E_0}} \tag{2.28}$$

where c_0 and c_1 are fitting constants. The WIMP spectrum is conventionally expressed in units $\mathrm{keV}^{-1}\cdot\mathrm{kg}^{-1}\cdot\mathrm{d}^{-1}$.
It must be mentioned that this is not the final theoretical spectrum to compare with the experimental one. In fact it must be applied corrections concerning Earth motion effects [55] and nuclear form factor of the detector nuclei (spin-dependent and spin-independent) [32].

So far, direct dark matter search experiments are reporting upper limits on WIMP-nucleon cross section since the signal they try to detect is still below their sensitivity. In order to evaluate the cross section limit we select an interval in the energy recoil spectrum and take as the upper limit the largest cross section (σ_{exp}) that would have a significant probability of giving as few events as were observed, assuming that they are all WIMP candidate signals. Integrating the theoretical spectrum to obtain the WIMP event number expected (μ_σ) for a given WIMP mass and scattering cross section $\sigma_{\chi-N}$. The limit on σ_{exp} is given by:

$$\sigma_{exp} > \frac{\sigma_{\chi-N}\,\mu_{exp}}{\mu_\sigma} \tag{2.29}$$

where μ_{exp} is the upper limit on the number of events that were observed if the cross section is σ_{exp}. In Fig. 2.13 are plotted the most recent cross section for WIMP-nucleon scattering.

2.3 Background sources

In counting experiments as DBD and DM, the sensitivity is, approximately, directly proportional to the signal rate but inversely proportional only to the square root of the background rate:

$$\Sigma \propto \frac{S}{\sqrt{B}}. \tag{2.30}$$

Because signal rates in the experiments mentioned above are mostly limited by parameters (or for economic reasons), the less effective road of background reduction must be followed. Certainly the different sources of background must be thoroughly understood before data taking can start. Each experiment is characterized

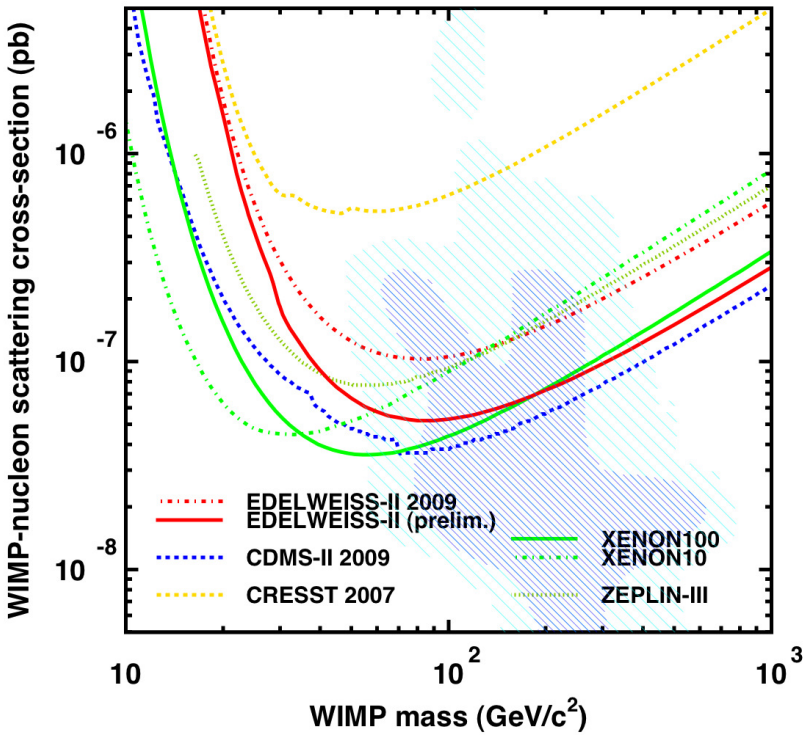

FIGURE 2.13: Summary of current spin-independent WIMP-nucleon cross section limits as a function of WIMP mass [6].

by different background sources, nevertheless they can be roughly classified into the following categories:

1. *primordial radioactive contaminations*, mainly ^{238}U, ^{235}U and ^{232}Th (see Appendix A) with their natural radioactive chains and the β/EC decay of ^{40}K;

2. *anthropogenic radioactive contaminations*, generally residual of nuclear explosions in the atmosphere, radioactive leakages by nuclear power plants and radioactive isotopes used in industrial processes, like: ^{60}Co, ^{90}Sr, ^{134}Cs, ^{137}Cs and ^{207}Bi;

3. *cosmogenic radioactive contaminations*, like isotopes produced by cosmic-ray interactions (e.g. in copper the following isotopes are produced: ^{57}Co, ^{58}Co, ^{60}Co and ^{54}Mn).

4. *environmental background at the experimental location*: cosmic rays, environmental gammas and neutrons.

The first two sources are controlled by accurate material selection and handling. Uranium and Thorium chains are serious backgrounds for experiments which look for signals below 5 MeV. Among those backgrounds there is the special case of ^{222}Rn (and ^{220}Rn)which is a gas. As a consequence the air in the environment in which the material will be handled or stored must respect specific constraints; these will be seen more in details in the next chapters.

Cosmogenic activation is controlled by reducing the exposure of materials to cosmic rays and by avoiding the use of nuclei with large activation cross-section. While for thermal neutron interactions the cross section are well known, in the case of high-energy neutrons or protons uncertainties on the activation reactions are larger. Simulation codes, based on theoretical evaluations of the cross sections, are generally used to predict the rate of activation under cosmic-ray exposure [56, 57]. In some special cases dedicated measurements are realized to attest the presence of any products of dangerous nuclear activation [58, 59].
In the case of the fourth background source the mandatory requirement for a *rare event* experiment is to be located underground. Indeed, only a sufficiently large rock overburden can ensure a relevant reduction of the most penetrating component of cosmic rays: muons. In typical underground laboratories the muon flux is reduced by several orders of magnitude, while all the other components of cosmic-ray radiation are negligible and only secondaries (e.g. particles produced by muon interaction in the rock) are present. These are neutrons and gamma rays. Also the rock radioactivity is a source of neutrons through the natural fission and (α,n) reactions. The flux of such neutrons is much more intense than the one of muon-induced neutrons. Their spectrum is however softer with an end point at few MeV. Environmental gammas are dominated by rock radioactive emission. Gammas are rather easily shielded with high-Z material like lead and copper, while neutrons are shielded with hydrogen-rich materials (for the neutron thermalization) mixed with high neutron capture cross section nuclei. Finally, veto systems are used for the rejection of the background induced by muons interaction in the set-up.

2.3.1 Environmental radioactivity

Radionuclides which go under the name of *environmental contaminations* are the ones that have been described in the previous section. These can be classified in three general categories: primordial, cosmogenic and anthropogenic.

The gamma radiation against which we must shield our detector is composed almost exclusively of photons from the U and Th decay series, ^{40}K and ^{60}Co decay, where the last one is produced through cosmogenic activation (e.g. activation of copper).

Secular equilibrium[3] in the decay series is not always achieved in matrix which are subjected to migration, since nuclides of the chain can leave the source as a result of physical or chemical processes. In particular Rn an intermediate member of all three decay series, may escape from the solid matrix either by recoil on ejection of the alpha particle or by diffusion (it is a gas). It is the way for Rn to be released from the Earth's land surface, known to be rich in Uranium and Thorium, into the atmosphere. The longer-living progeny ^{210}Pb is readily attached to aerosols and finally deposited on the surface by washout and dry deposition.

2.3.2 Radon and its progenies

^{222}Rn, by far the most intense source of airborne radioactivity, is present in indoor sites at an average concentration of 20 Bq·m^{-3} (depending on ventilation and many other atmospheric parameters). This concentration corresponds to about 10 nuclides of ^{222}Rn per cm^3, which is already a significant source of contaminant in low-background experiment. The radiopurity requirements for such experiments is 10^6 times smaller [60]. Another isotope of Radon, ^{220}Rn (also known as Thoron), is produced in the Th decay chain. This isotope has a short half-life ($T_{1/2}^{^{220}Rn} = 55.6$ s) compared to $T_{1/2}^{^{222}Rn} = 3.82$ d, consequently its concentration is more sensitive to pressure changes and other factors influencing the emanation. Therefore, due to the short half-life, its concentration strongly decrease with the distance from the emanating source, hence its activity is normally below the percent level of ^{222}Rn.

Great importance needs to be addressed in analysing the progenies of these radioactive isotopes. The Thoron family dies rather quickly, with an half-life of 10.64 h (the longest daughter half-life of ^{220}Rn is ^{212}Pb), but on the other side Radon feeds into ^{210}Pb with an half-life of 22.4 y. The last gamma-active nuclei for the Radon chain is ^{214}Bi, neglecting the 803.3 keV gamma line of ^{210}Po which has a branching ratio of 0.1%. Thus, at least the gamma activity dies out with the half-life of ^{214}Pb ($T_{1/2}^{^{214}Pb} = 26.8$ min).
If we focus on the β emission in the Radon chain, significant contribution comes

[3]The activity of all daughter nuclides are equal to the activity of their respective parents.

from ^{210}Pb which produces two low energy β of 17.1 keV and 63.5 keV. These β might mimic other low energy events in low-background experiments such the DM ones. Other β-active nuclei are ^{214}Bi and ^{210}Bi which produce high energy electrons with a maximal energy of respectively 3.27 MeV and 1.17 MeV. Finally we cover the subject concerning the α emitted by the Radon chain. Different elements decay through the α channel, short half-lives nuclides like ^{218}Po, ^{214}Po but also ^{222}Rn itself. The ^{210}Po is also an α-emitter but its activity is reduced by the half-life ratio of 3.82 d to 22.4 y (^{210}Pb, its parent), so it might give a negligble contribution. But if it is accumulated over long periods it may disturb, in particular experiments that are sensitive to the α particles.
On the other side Thoron contaminations lead to ^{208}Tl, which is known to be one of the most significant background source for DBD experiments.

The best way to protect a detection system against Rn and its strong concentration variation in air is to protect the system with metal foil or a metal sheet (Uranium and Thorium free) as tightly as possible. A small overpressure of Nitrogen evaporated from liquid Nitrogen reservoir can help expel enclosed Radon and suppress influx through cracks or small openings. However overpressure inside the detection system, hypothetically Rn-free, cannot prevent diffusion because the latter depends only on partial differential pressure.

2.4 Background suppression methods

2.4.1 Material selection

The degree of radiopurity in the detector assembly is relevant if we wish to reach the goals foreseen for the experiments. The selection of materials must be carried out in a meticulous way since interrelations also exist. For instance, the choice and thickness of material for the shield against external gamma radiation does influence the cosmic ray-induced background.

The omnipresence of primordial radionuclides in ores and other raw materials results in a wide range of contaminations in the final product. With some exceptions, the principal radiocontaminants are usually Potassium and Thorium-Uranium. Complex production processes involving many stages and frequent contacts with different reagents make difficult to guarantee acceptable contamination

TABLE 2.4: Sensitivities in $mBq \cdot kg^{-1}$ achieved in copper analysis with different techniques. ^{238}U and ^{232}Th are assumed in secular equilibrium. The quoted sensitivities refer to measures done: (**I**) at sea level with a 100% HPGe detector in Milano-Bicocca laboratories [19], (**II**) underground at Laboratori Nazionali del Gran Sasso (LNGS) with a 110% HPGe detector [19], (**III**) with an ICPMS [20], (**IV**) in Milano with a 100% HPGe detector using an irradiated sample from the LENA Triga Mark II reactor in Pavia [19].

Method	^{238}U	^{210}Pb	^{232}Th	^{60}Co	^{40}K
I (HPGe - Milano)	< 10	< 4	< 1	< 10	< 1
II (HPGe - LNGS)	< 0.01	$< 10^4$	< 0.01	< 0.01	< 0.1
III (ICPMS)	< 0.04	-	< 0.01	-	-
IV (NAA)	< 0.1	-	< 0.003	-	-

levels. The different chemical and physical behaviors of elements of decay series (e.g. Ac, Pb, Ra, Rn) sometimes result in deficiencies or isolated impurities, like the following isotopes: ^{226}Ra, ^{222}Rn and ^{210}Pb. Other parent-daughter separations or equilibrium breakings are also possible. Thus the material selection and handle must be carried out thoroughly. Traditionally [61], this selection is based on gamma-ray spectroscopy employing high-purity Germanium (**HPGe**-diode) detectors, but recently the use of different and more specialized techniques has grown in importance [62, 63]. These are mass spectroscopy (e.g. Inductive Coupled Plasma Mass Spectroscopy, **ICPMS**), α spectroscopy (employing Silicon surface barrier detector, **SBD**) and analysis through neutron activation (Neutron Activation Analysis, **NAA**) (see Table 2.4).

HPGe gamma spectroscopy is by far the most widely used technique, since most radioactive impurities have intense and characteristic gamma emissions. The sensitivity depends on the germanium diode detector efficiency and on its intrinsic background level. The achievement of very high sensitivities ($\mu Bq \cdot kg^{-1}$) requires high-purity detectors, an underground facility and a dedicated heavily shielded set-up as well as a strict control of any possible external contamination.

ICPMS is a technique for elemental analysis that can be used for the measurement of trace elements. Sensitivities comparable with those achievable with gamma spectroscopy are feasible for long living isotopes. The main limiting factor is the radiopurity of the reagents used for the treatment of the source that has to be analysed.

NAA is a multi-element analytical technique employed for identifying trace elements in solid matrix. The technique consists in irradiating the sample with

thermal neutrons and later measure the gamma emission of the sample, identifying the radioactive isotopes created by neutron capture on the matrix impurities. Among the radioactive contaminations that can be investigated with NAA there are the ^{238}U and ^{232}Th chains. In this case primordial parents of these chains are activated and characteristic gammas emitted respectively by ^{239}Np (at 106.1 keV and 277.6 keV) and ^{233}Pa (at 311.9 keV) are observable.

Finally, silicon SBD are used to scrutinize the presence of α or β emitters isotopes in matrixes. Due to the short range of α/β particles this technique is sensitive only to the radioactive content in the first layers (order of few μm) of the sample, a layer which is often characterised by a contamination excess compare to the bulk one. This type of contamination is particularly dangerous if the detector (e.g. a bolometer) does not have a dead layer on the surface. We shall see this more in details in the next sections.

2.4.2 Shielding and veto

Primary cosmic ray particles (about 90% protons, 9% alphas and 1% heavier particles) hit the Earth atmosphere at a rate of about 0.1 cm^{-2}·sec^{-1} [64]. Their interaction with atmospheric atoms generates the following variety of elementary particles: neutrons, electrons, neutrinos, protons, muons and pions. The total intensity of these secondaries reaches a maximum at an atmosperic depth of about 14 km of altitude and then falls off gradually. At the sea level, the relative intensity of charged pions:protons:electrons:neutrons:muons is about 1:13:340:480:1420, with a flux for charged pions of about $1.3{\cdot}10^{-5}$ cm^{-2}·sec^{-1}.

Environmental gammas and cosmic rays are reduced by means of proper shieldings. The underground sites certainly provide clean radioactive environments. In low-radioactivity background techniques only muons and neutrons are relevant particles. Electrons and photons, named *weak component*, are directly absorbed by the lead and copper shields.

In order to run low-background experiments an underground facility is mandatory. The thickness of the rock overburdern decrease the muon flux, roughly, but not exactly, exponentially (see Fig. 2.14). Under a flat surface the flux is 10^{-3} m^{-2}·sec^{-1} at a depth of 2300 meters water equivalent (*m.w.e.*) and 10^{-5} m^{-2}·sec^{-1} at 5300 m.w.e. [65]. Under a mountain, like at Kamioka or Gran Sasso, the angular dependence of the muon flux is complicated, due to the shape of the surface.

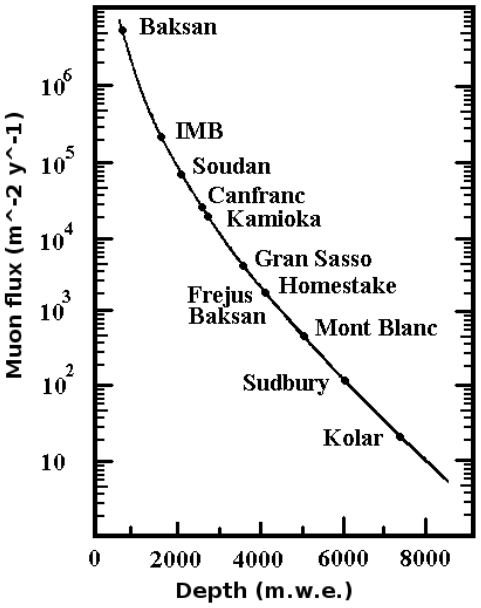

FIGURE 2.14: Muon flux as a function of depth inside some underground laboratories.

Furthermore the flux is time dependent with seasonal variations of several percent. Unfortunatly the underground depth is not enough to reduce the muon flux down to the background requirements for the experiment, besides the muons being deep penetrating particles, cannot be removed by a shield. Generally the most severe problem is due to the gamma and neutron background arising from their interaction in the set-up , and not from the muon direct interaction in the detector, which can be removed through coincidence cuts. The presence of heavy, high-Z shields makes the situation even worse, because it may increase the muon interaction probability, generating showers. The only way to get rid of this background is by the installation of muon veto able to reject any muon-induced interaction.

Neutrons originate mainly from (α,n) reactions and fissions processes (U and Th) in the rocks. The energies range from thermal to several MeV, and consequently the thermalization becomes slow. The neutron flux is substantially independent of the depth, it depends only on the local geology.

Muons interactions in the rocks produce dangerous neutrons at a depth-dependent rate. The fluxes are typically few orders of magnitude smaller than the ones produced by the fission processes. The energies are large, up to several GeV. Even more dangerous are the neutrons produced in the shields, in the detector and in the passive materials. In the case of fast reactions, mainly if a neutron immediately follows the muon, the background can be reduced by anticoincidences.

As shown in this section backgrounds need to be completely undestrand for DM and DBD search experiment. This thesis work is mainly focused on the study of surface contaminations, as a background for rare event searches, as described in the next chapter.

Chapter 3

Surface contaminations

In this chapter we will have a closer look at the detectors employed for rare event search, for DBD0ν and dark matter experiments. We will analyse the working principle and the characteristics that make thermal detectors the suitable tool to be used for these types of searches. Unfortunately, of course, bolometers present not only good aspects but also limitations, as the lack of a dead layer. In fact bolometers are completely active over the entire volume this means also that they are sensitive to surface events. These require great attention since, as we will see, surface contaminations can deposit just a fraction of the whole particle energy mimicking the rare events which we are interested in. This lack of a direct detector shielding is the main source of contaminations, which leads to unavoidable backgrounds, depending on the type of detector.

3.1 Bolometers

Cryogenic particle detectors, named *bolometers*, were used for the first time for rare event search the '80s [66]. Today micro-bolometers (with masses smaller than few grams) are mainly used in X-ray astronomy and β decay measurements. Macro-bolometers (with masses ranging from few grams up to few kilograms) are employed in *rare event physics*: double beta decay, dark matter and rare nuclear decay searches.

The operation of a detector aiming at a search for rare events implies the removal of any spurious source that can mimic the rare event (e.g. radioactive source or cosmic rays). The residual background counting rate measures the sensitivity

of the experiment. As a consequence, one of the main issues of present and future DBD0ν and DM experiments is the identification, control and reduction of the radioactive background. This field is rather new and unexplored for bolometers since most of the experimental activity was concentrated so far on their technical development, aiming at the improvement of their resolution and stability as well as the increase of their mass.

In the last 30 years a huge progress has been made in the development of cryogenic particle detectors [67]. The performances are greatly improved and very massive detectors have been assembled [68]. For specific experiments, detectors with simultaneous measurements of heat and ionization [69, 70] (or scintillation [71]) were also developed. Cryogenic particle detectors have been applied in many fields, not only in particle physics experiments, thanks to some peculiar characteristics that they exhibit. Experiments on double beta decay take advantage from the good energy resolution and the flexibility in selecting materials; low energy thresholds and high efficiency to nuclear recoils of these detectors are very interesting in dark matter searches; the impressive high energy resolution of microcalorimeters is suitable for X-ray spectroscopy and direct neutrino mass measurements. Other useful characteristics concern the detection principle: in fact bolometers are sensitivite to almost any kind of interactions that produce no ionization, and do no exhibit a death layer on the surface. This last two features can be considered as the significant ones, since they imply many pros and cons.

3.1.1 Working principle

The basic idea is very simple [72] and consist in cooling down a material (namely the detector) and measure the signal produced by phonons due to the energy deposit in the detector. The technique requires specific thermometers sensitive to variation of temperature of the order of 10^{-6} K.
Bolometers consists of two main components: an energy absorber, where particles deposit their energy and a sensor, which converts the excitations produced by the particle into a signal (see Fig. 3.1).
Starting with the general properties that all the energy will be finally transformed into heat, cryogenic particle detectors are employed for measuring the energy released by a particle that interacts with a solid medium (the *absorber*). For a crystal with a heat capacity equal to C, a particle that releases an energy E will

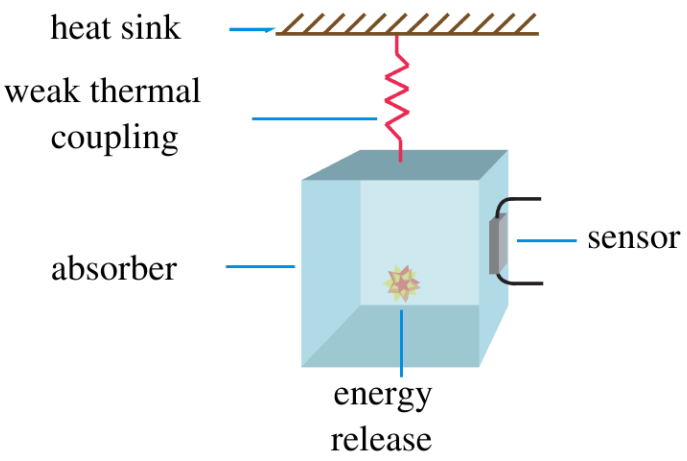

FIGURE 3.1: Schematic representation of a bolometric detector: an absorber is connected to a heat sink through a weak thermal coupling and a sensor for signal read-out is attached to the absorber.

produce a temperature variation equal to:

$$\Delta T = \frac{E}{C} \tag{3.1}$$

Obviously the heat capacity of the crystal must be as low as possible to increase the temperature variation. So it is necessary to operate cryogenic detectors at temperatures well below 1 K and to select specific materials in order to avoid contributions that increase the heat capacity. In order to keep the temperature stable and low, the absorber is connected to a *heat bath* through a conductance G. The absorbed heat then flows trough the conductance until an equilibrium condition with the heat sink is reached. The dynamics follow the exponential law:

$$\Delta T(t) = \frac{E}{C}\, e^{-\frac{t}{\tau}} \tag{3.2}$$

where $\tau = C/G$ is the time constant of the bolometer. With these basic considerations, it is clear that in order to obtain a fast (and large) signal the capacitance of the absorber must be small. This constraint can be fulfilled only if the detector is operated at cryogenic temperatures, between 10 and 100 mK.
Many materials have characteristics that contribute to the specific heat, in particular significant contributions come from the lattice that is proportional to $(T/\Theta_D)^3$, where Θ_D indicates the Debye temperatures of the material, and from the electrons that depends on (T/Θ_F), where Θ_F indicates the Fermi temperature:

$$c(T) = c_l(T) + c_e(T) \tag{3.3}$$

The lattice specific heat is described by the Debye law:

$$c_l(T) = \beta \left(\frac{T}{\Theta_D}\right)^3 \qquad T < \Theta_D \tag{3.4}$$

where $\beta = 1944$ J·K^{-1}·mol^{-}1. For metals the electronic contribution to the specific heat is proportional to T and is described by the following equation:

$$c_e(T) = k \cdot T \tag{3.5}$$

where k is a constant that varies for different materials (number of electrons in the conduction band and Fermi temperature).

In a basic model, in which all the phonons can be detected, a rough evaluation of the energy resolution can be estimated. The only limitations to the resolution of the detector are the thermodynamic fluctuations of the phonons that are exchanged between the heat sink and the detector itself, through the conductance G. The fluctuation of the number of phonons in the absorber produces a temperature variation that consequently affects the energy resolution. The energy E in the absorber is:

$$E = c(T) \cdot T = N \cdot \epsilon \tag{3.6}$$

where ϵ is the energy of each phonons: $\epsilon = k_B T$.
Assuming that the phonon number follows a Poissonian distribution and that the thermometer is ideal, the energy fluctuation is:

$$\Delta E = \Delta N \cdot \epsilon = \sqrt{k_B \, c(T) \, T^2} \tag{3.7}$$

It should be stressed that for dark matter bolometers and double beta decay bolometers the thermodynamic fluctuations give a negligible contribution to the energy resolution. From the above expression, using typical values for a bolometer (e.g. C=10^{-9} J·K^{-1} and T=10 mK) a resolution of few eV (∼10 eV) is predicted, that is well below the measured resolution (few keV). This means that there is still a lot of work to do for improving the detector energy resolutions.

3.1.2 Thermal sensor

The phonon sensor is basically a device able to convert thermal excitation energy into an electrical signal. Two kinds of sensors are used in rare event experiments:

semiconductor thermistors (ST) and transition edge sensors (TES). In both cases the working principle is based on the dependence of their resistivity on the temperature, even if the physical origin for this behavior is rather different for the two devices.

Thermal sensors are characterized by their logarithmic sensitivity, given by the expression:

$$A = \left| \frac{d \log R(T)}{d \log T} \right|. \tag{3.8}$$

The above expression implies that:

$$\frac{dR}{R} = A \frac{dT}{T} \tag{3.9}$$

where obviously the larger is A the higher is the response of the device. Typical values of A are 10 for ST and 100 for TES. Despite the lower sensitivity, ST have a wider range of operating temperature, while TES are strictly limited to a rather narrow temperature range. We will focus on semiconductor thermistors (because of their versatility).

Semiconductors are covalent solids that behave as insulators because the valence band is full and the conduction band is empty, nevertheless the energy gap between valence and conduction band is less than 2 eV. The conduction can then occur only if the activation energy is higher than the energy gap. Since at room temperature $kT \simeq 0.025$ eV, the conduction can happen at higher temperatures. If instead the semiconductor lattice has impurities (e.g. doped semiconductors), then new energy levels are introduced slightly above the valence band or below the conduction band, depending on the type of impurity introduced. With this technique the conduction can also occur at lower temperatures. The dopant concentration determines the behavior of the solid and there is a critical concentration that characterizes the transition from metal to insulator. The region near this concentration is named metal-insulator transition region (MIT) [73], where the material resistivity exhibits a dependence on the temperature.

At low temperature ($\sim$10 K) the conduction is dominated by the migration of the charge carriers between impurity sites. In this situation electrons are not localized and the conduction happens when an electron jumps from a donor site to another, without using the conduction band (*hopping mechanism*). This migration is due to the tunnelling through the potential barrier separating the two dopant sites and it is activated by phonons (see Fig. 3.2). Even at lower temperature, the

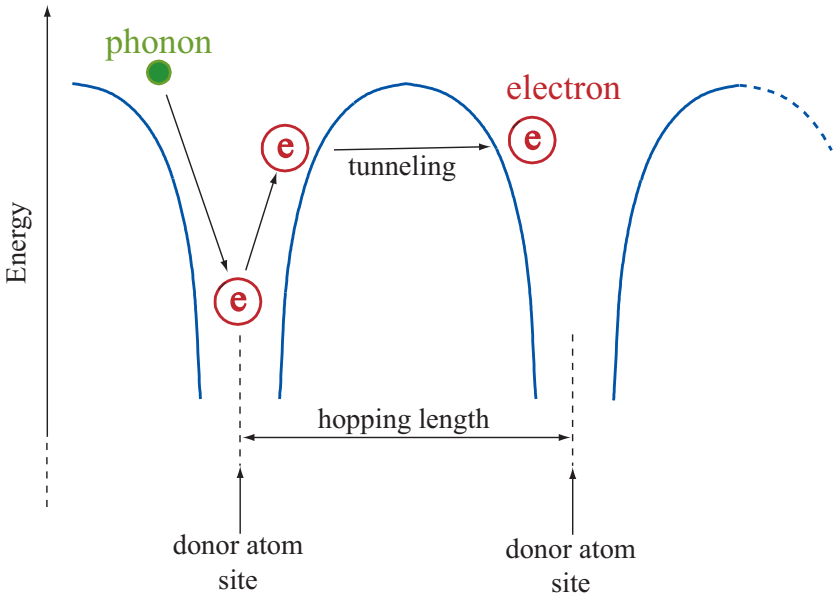

FIGURE 3.2: Schematic representation of the hopping conduction mechanism.

energy of the phonons that are responsible for the conduction mechanism is low, and charge carriers migrate also to far impurity sites with free energy levels that are close to the Fermi energy. In this conduction regime, called variable range hopping (VRH) [74], the concentration of minority charge carriers determines the density of states close to the Fermi level. The MIT is set not only varying the concentration of the impurities, but also varying the ratio of acceptor and donor concentrations.
In the VRH conduction regime the resistivity dependence on temperature is described by the law:

$$\rho(T) = \rho_0 \, e^{(T_0/T)^{\gamma}}, \tag{3.10}$$

where ρ_0 and T_0 depend on the doping concentration and $\gamma = 0.5$. The expression of the logarithmic sensitivity can be easily derived from the above equation:

$$A = \gamma \left(\frac{T_0}{T}\right)^{\gamma}. \tag{3.11}$$

3.1.3 Detector operation

In order to be able to measure the resistance variation the thermistor is biased with the circuit shown in Fig. 3.3a. A bias voltage V_{BIAS} is produced by a voltage generator closed on a load resistor that is put in series with the thermistor. The

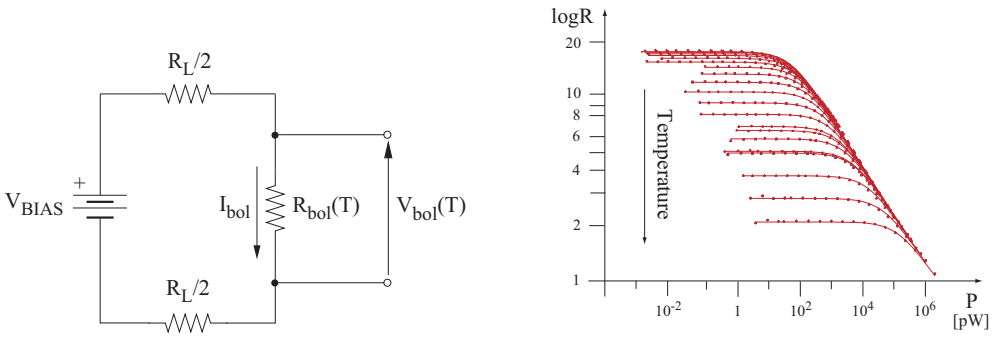

(a) (b)

FIGURE 3.3: Picture (a) shows the electric scheme of the bias circuit used for thermistor readout. The right picture (b) shows the dependence of the resistance on the power dissipation for various values of the base temperature. Curves with lower resistance at P=0 correspond to higher base temperatures.

load resistance R_L is chosen much higher than the thermistor resistance R_{bol} so that the current in the circuit I_{bol} is constant and the voltage across the thermistor V_{bol} is proportional to R_{bol}:

$$V_{bol}(T) = I_{bol} \cdot R_{bol}(T). \tag{3.12}$$

This current produces a power dissipation $P = V_{bol} \cdot I_{bol}$ that heats the thermistor decreasing its resistance: this phenomenon is known as *electrothermal feedback*. In static conditions the thermistor temperature T_S is:

$$T_S = T_{hs} + \frac{P}{K} \tag{3.13}$$

where T_{hs} is the temperature of the heat sink and K is the conductance to it. The $R - P$ dependence is shown in Fig. 3.3b. The electrothermal feedback makes the $I_{bol} - V_{bol}$ relation deviate from the linearity and leads to a non-ohmic behavior (see Fig. 3.4a). Increasing the bias current the slope of the curve increase until it crosses the so called inversion point (IP) and then decreases. In static conditions the thermistor electric and thermal parameters are described by a point on the load curve.

When particles release an amount of energy E in the absorber the voltage across the thermistor varies leading to a signal. A rough estimate of the voltage increase is:

$$\Delta V_{bol} = A\, V_{bol} \frac{\Delta T_S}{T_S} = A \sqrt{P \cdot R_S}\, \frac{E}{C \cdot T_S} \tag{3.14}$$

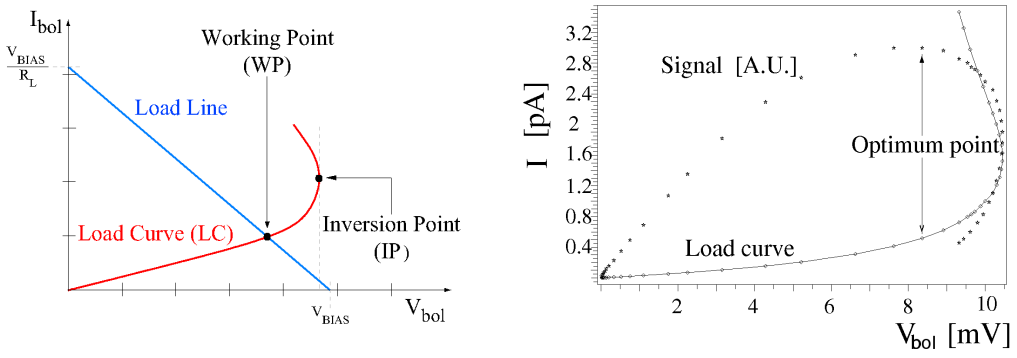

(a) (b)

FIGURE 3.4: Load curve of a semiconductor thermistor. On the left (a) the working point is determined by intersection of the sensor characteristic curve with the bias circuit load line. On the right (b) the load curve is shown together with the corresponding signal amplitude.

where R_S is the static resistance and we used $R_L \gg R_S$. This expression vanishes both for $P \to 0$ and $P \to \infty$ because the resistance vanishes at high temperatures, then a maximum signal amplitude must exists somewhere. If all the detector parameters were known, the optimal working point could be determined analytically. Nevertheless, it often happens that not all of them are known with accuracy and the working point has to be determined experimentally. The procedure consists in scanning the amplitude of a pulse of fixed energy varying the bias current, and selecting the point where the signal to noise ratio is maximum (see Fig. 3.4b).

3.2 Surface contaminations: problems and approaches

As mentioned previously surface contaminations are a serious limitation to low background experiments. First it should be defined what we mean with surface and surface contaminations. Generally a surface is defined as the discontinuity between two media, but this definition does not state how thick is a surface, and when the bulk ends and the surface begins. Radioactive contaminants may help in setting a range of length for which it is possible to differentiate these two regions. We can state that if the products of a radioactive decay realise the whole energy of the reaction (Q-value) inside the matrix in which the source is located, thus we can talk about bulk contamination. Otherwise if the energy is not entirely deposited inside the matrix we are dealing with surface contamination. This statement is true just for α and β radiations, in fact γ rays have a point-like interaction either

in the bulk or on the surface, or in the two regions at the same time through a Compton scattering. Neutrons requires a different type of physics definition.

According to what has been stated the surface depth depends on: the energy of the particles, the type of particle and also the material of which the matrix is made of. An alpha particle of 5 MeV in Germanium can travel at maximum about 23 μm while an electron of 100 keV about 72 μm. Generally speaking the depth that we are dealing with has a maximum range of tens of μm from alphas and betas of primordial contaminations.
The energy lost obviously is different for the alphas and betas along the trajectory. In fact alphas lose the most of their energy at the end of their track, while electrons tends to lose it uniformily along the track (see Fig. 3.5). Thus the electrons coming out from a surface are always difficult to identify since they lost, right after the emission, any information concerning the source that has produced them (the parent nucleus and the location of the contamination). On the other side alphas, depending at which depth they are emitted, can carry that type of information. But if an alpha particle is emitted at the depth corresponding to the Bragg peak, then we are not able to identify the energy that the particle had at the emission site.
So we define surface as the first few micrometers of the outter part of a sample.

For DBD0ν and DM experiments one possible background source is an alpha decay that occurs on the surface of materials facing the detector, or on the detector itself. In fact if we imagine the case in which an alpha (or the recoil nucleus) is coming out from a material that faces the detector (e.g. copper), then the alpha

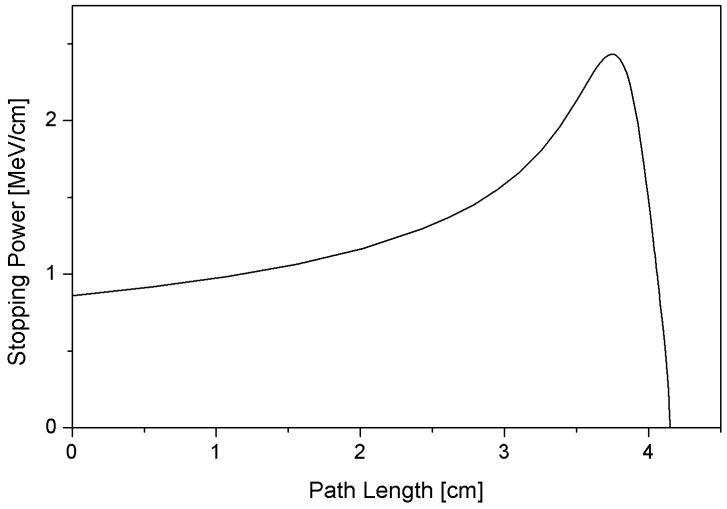

FIGURE 3.5: Bragg curve for an α particle of 5.5 MeV in air.

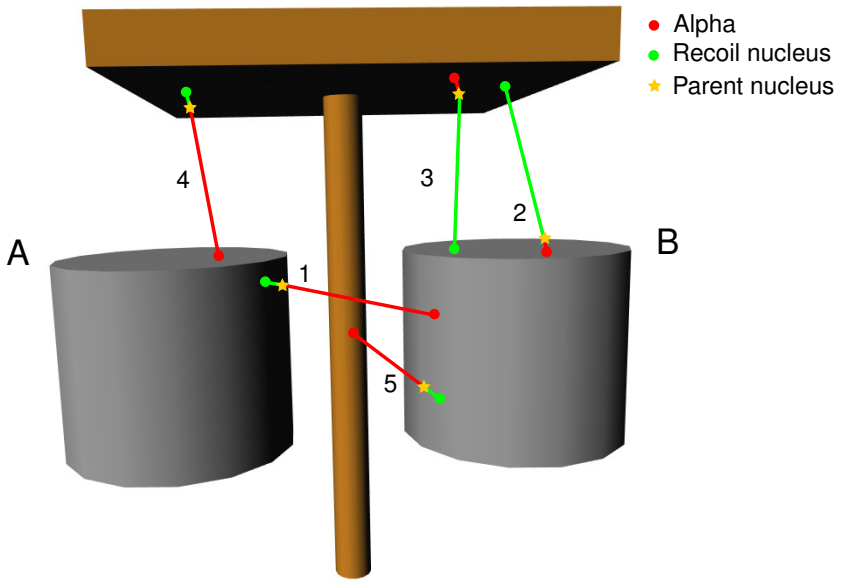

FIGURE 3.6: Examples of alpha decays on active materials (grey) and passive materials (brown).

will leave part of its energy in the copper and the rest in the detector. The first amount of energy will not be detected, and as a consequence in the detector will arrive an alpha having an energy that does not correspond to the initial energy of the particle (degradaded alpha). This energy difference is a function of the depth at which the decay occured: the deeper is the site of the parent nucleus decay, the bigger will be the energy loss of the alpha.
We can see more in details the detector behaviors for different configurations of the parent nucleus locations with respect to the detector. If we look at Fig. 3.6, it is possible to identify five different cases in which a signal is produced in the detector either by an alpha or by a recoil nucleus:

1. The decay occurs on the surface of detector A, the recoil nucleus produces a signal in this detector, while the alpha deposits its energy in the other detector. This type of surface event is discarded with a coincidence cut.

2. The parent nucleus decay on the surface of the detector: the alpha leaves its energy in the detector while the recoil nucleus deposits its energy both on the detector and on the passive material (e.g. copper). This configuration produces in the energy spectrum of the bolometer a peak at E_α (energy of the alpha particle) and a tail that goes up to $E_\alpha + E_{recoil}$.

3. The disintegration occurs on a passive material facing the detector. The entire alpha energy is released on the copper and the recoil nucleus losts its

energy both on the copper and on the detector. This event creates a broad distribution up to E_{recoil}.

4. As the previous case except that the particles take opposite directions. In this case the signal produced in the detector is a broad distribution up to E_{α}.

5. The parent nucleus transmutes on the detector surface. The alpha particle escapes from the surface and deposits most of its energy on the frame of the detector, while the nucleus does not leave the detector. The signal produced is a broad distribution around the value E_{recoil}.

If we simply refers to the ^{210}Po α-decay, the energy of the alpha particle is 5.304 MeV and the nucleus recoils with an energy of 103 keV. Then the third and fifth case might give a background contribution to the region of interest of DM experiments, while the second and the fourth to a DBD0ν experiment. As already stated DBD0ν experiments look for a peak at an energy equal to the Q-value of the reaction. Mostly neutrinoless double beta decay candidates have a Q-value which is of the order of few MeV (see Table 2.2). Comparing these values with the energy of some natural alpha decays, if a degraded alpha reaches the detector then an overlapping of the two signals may occur as well as for DM experiments which look for a signal in low energy regions.

Beta decays occuring on the detector surfaces will always give a background contribution in DM and DBD0ν experiments, except for the case where coincidence cuts are applied. Being a three-body disintegration implying a neutrino (antineutrino) emission, it is a tough task to be able to detect all the decay products and thus the emission site (parent nucleus location). Fortunately there are just few high energy β emitters that can produce background in the DBD0ν region (^{214}Bi and ^{208}Tl), while almost all the β emitters are a source of background in DM experiments.

The third most important source of surface contaminations are the gamma emission of some nuclei, in the specific low energy range for DM experiments and for specific gamma lines depending on the nucleus employed for the DBD0ν search (e.g. the ^{208}Tl γ at 2615 keV for the ^{130}Te). The real issue is connected to the possible single Compton-scattering of a gamma on the detector surface, which can mimic both a DBD0ν decay and a WIMP recoil. Moreover if the detector is not able to discriminate neutrons, alpha and beta (gamma) particles the background reduction is still a tough task.

As already shown, surface contaminations can affect both active materials such as the detector and passive materials like detector's assembly materials (e.g. copper and teflon), depending on the handling (e.g. machining, cleaning procedure and storage site), the chemical features of them and the initial radioactive contamination. It is important to distinguish between these two classes of materials because, in an experiment looking for rare events, they appear in different quantities, following the design of the experiment. At the same time there are different precautions that can be adopted in order to mitigate the surface contamination problem. In fact in the case of radioimpurities on the surface of both active and passive materials there are two main categories of strategies that can be identified: the first one consists on employing a detector with high granularity[1]. A real advantage consists of high geometric efficiency for the detector surfaces and small for the passive materials. An example of this type of detector is illustrated in Fig. 3.7, where the high number of detectors supported by a shrunk copper structure of Cuoricino allows applying in the analysis coincidence cuts due to high geometric efficiency of the detector, where the crystals face each other. Unfortunately the use of high granularity detectors implies big detector surfaces and thus requires a more thorough control of the surface contaminations, obviously at the same time passive materials should be reduced as much as possible. The second strategy consists of an active rejection of surface events using vetos. In this case the idea is to tag all surface events cutting out of the detector a fiducial volume and considering the rest as a veto. An example of this type of detector is given in Fig. 3.8 where the voltage applied to the detector, allows discriminating between surface and bulk events by means of the shape of the electric field in the region underneath the electrodes. This type of surface contamination control has an higher power rejection of surface events, but the limitation is the significant reduction of the active volume of the detector as it is illustrated in the schematic view of the Edelweiss detector (Fig. 3.8b).

There is also a commonly used precaution which consists on some cleaning procedure, which may prevent the diffusion and the bounding of radioactive contaminants on the surface [75].

[1]Composed by an elevated number of detectors of small size

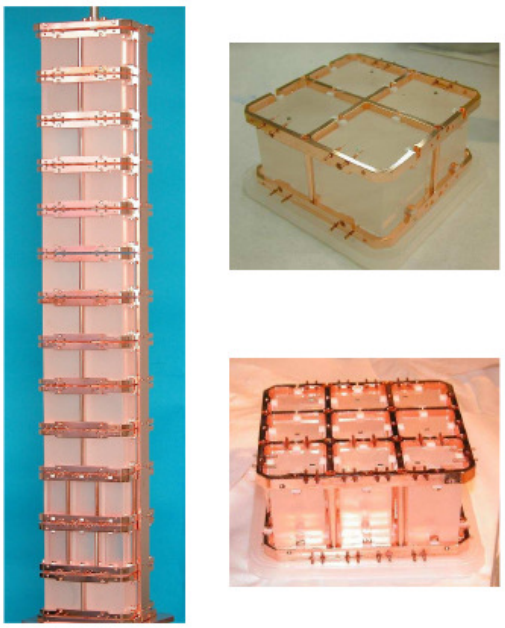

FIGURE 3.7: Photographs of a modular detector for DBD0ν search: CUORICINO tower and two different modules. On the top right is a 4 crystal array of 5 x 5 x 5 cm^3, and on the bottom right a 9 crystal array of 3 x 3 x 6 cm^3.

3.2.1 The copper issue

High-purity copper is an attractive material for constructing ultra-low background radiation detectors. Copper has favorable mechanical, electrical and thermal properties, and is easily purified. Intrinsically low in primordial radioisotopes and having no long-lived radioisotopes itself (see Table 3.1), copper also benefits from the *electroforming process* [76]. In this processing, a current is passed from an inert anode through a liquid solution containing the metal so that the metal is extracted

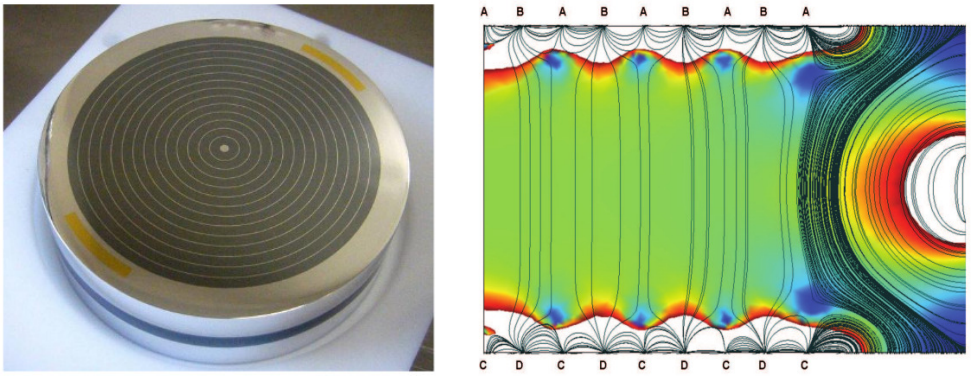

(a) (b)

FIGURE 3.8: Edelweiss (a) detector and (b) simulation of the electric field inside the detector.

TABLE 3.1: Present best values on the radioactive content in Electroformed copper.

Contaminant	Content [g/g]	Technique	Reference
^{232}Th	$< 4.9{\cdot}10^{-13}$	NAA	[77]
^{238}U	$< 2.4{\cdot}10^{-12}$	NAA	[78]
^{40}K	$< 4.0{\cdot}10^{-12}$	NAA on ^{41}K	[79]

as it is deposited on the cathode. Many contaminations of radiopurity significance do not follow copper in this step by virtue of their negative electrochemical values. When higher purity is required, additional fabrication steps are added up (like electroforming and chemical purification), providing a potential way to eliminate cosmogenic activation products seen in copper (e.g. ^{60}Co).

Most of the components that directly face the detector are made of copper, so a strict control of the radiopurity of it is required. Even if the copper is free of any kind of contaminants a recontamination is still possible due to the handling of it in non-controlled environment or the contact with materials which are not radioactively pure.
The problem we have just illustrated concerns not only the copper but also all the materials, either active or passive, which are close to the detector.

3.3 Sources of surface contaminations

The use of radiopure materials for the detector assembly is a fundamental and crucial point, as already discussed. It is possible to keep under control the different steps that bring to the final production of the detector components, in such a way that the residual contamination of these components is well known. Problems may arise, not only during the production but also in all the final stages in which the detector is stored, ready for the assembly, and during the assembly phase. In fact these procedures are the most crucial ones because the detector will be handled in an environment different from the one in which it was stored, and the crossing between the two environments might lead to some uncontrolled contaminations, especially at the interface between the two environments. Furthermore the detector assembly in the new environment might take a long time, this might also lead to an uncontrolled contamination even if all the major precautions are taken. Moreover if the recontamination occurs, in unstable conditions (there is

not secular equilibrium between the various elements), then the real effects will be visible only after a period of time comparable with the half-life of a radionuclide contaminant (e.g. 22.3 y for the ^{210}Pb). These effects might be more visible and more significant, in particular with a low background detector.
This thesis aims at studying the dynamics and the mechanisms which lead to the recontamination of the radiopure components of low background experiments, in the specific DM and DBD experiments. In this frame a thorough analysis about Radon-induced surface contaminations is carried out for the understanding of how these recontaminations can affect the performances and the sensitivity of the experiments.

As already discussed, one of the most dominant radioactive background comes from radon gas which is naturally present in air. Radon is particularly difficult to control due to its high mobility. In practical terms this means low background detectors must be designed to be leak tight to air. As an additional constraint, surface contact of detector materials with radon progeny must also be minimized. In general it is possible to identify three main processes that lead to radon (and its progeny) contaminations:

- gravimetric deposition of particulate matter (PM) and radon combinations. Especially ^{210}Pb which is highly reactive with small dust particles (aerosols)[80];
- radon diffusion into solids. It is already well known that a gas can diffuse inside solids due to the different Rn concentration between the solid and the environment [81];
- nuclear recoils implantation of Rn nuclei. The decays that occur close to the surface materials can implant Rn-progeny nuclei, which can further diffuse inside the material through the same process of nuclear implantation.
- chemical boundings between radon progenies and the sample exposed to radon.

It is important to stress the fact that radon induces surface contaminations, but since it has a short half-life (T_{Rn}=3.8 d) it is sufficient to wait about 15 days (about 5·T_{Rn}) to get rid of all the radon contamination. The real issue is the contamination induced by radon progeny, in particular the daughters that have a longer half-life like Lead-210 and Polonium-210. For these isotopes it is not possible to wait until all the nuclides have decayed. So it is necessary to reduce

their amount since the first step of material production and to employ trustworth cleaning procedures which will reduce their contamination.

3.4 Dynamics of surface contaminations

Because of the long half-lives of the elements in the lower part of the Uranium chain (Rn chain) a certain time is needed in order to reach the secular equilibrium between the various elements of the chain. And it is exactly during this period that the activity of the radionuclide is not constant and thus difficult to compute. Another reason that makes the computation difficult is because the processes, previously illustrated, have low efficiency so we have to deal with really small surface contaminations.

In the following section we will have a closer look at the dynamics which allow a general radioactive decay chain to achieve the equilibrium after a transient state, and then this model will be applied to the radon case. We assume that we begin with N_0 atoms of the parent a $t = 0$ and that no atoms of the decay products are originally present:

$$N_1(t = 0) = N_0 \tag{3.15}$$

$$N_2(t = 0) = N_3(t = 0) = ... = 0. \tag{3.16}$$

The various decay constants are represented by τ_1,τ_2,τ_3,.. . For the present calculation, we will assume that the granddaughter is the stable end-point of the decay. The number of parent nuclei decreases with time according to the well known formula:

$$dN_1 = -\frac{N_1}{\tau_1}\, dt. \tag{3.17}$$

The number of daughter nuclei increase as a result of decays of the parent and decreases as a result of its own decay:

$$dN_2 = \frac{N_1}{\tau_1}\, dt \; - \; \frac{N_2}{\tau_2}\, dt. \tag{3.18}$$

The number of parent nuclei can be found directly from integrating equation 3.17:

$$N_1(t) = N_0\, e^{-t/\tau_1}. \tag{3.19}$$

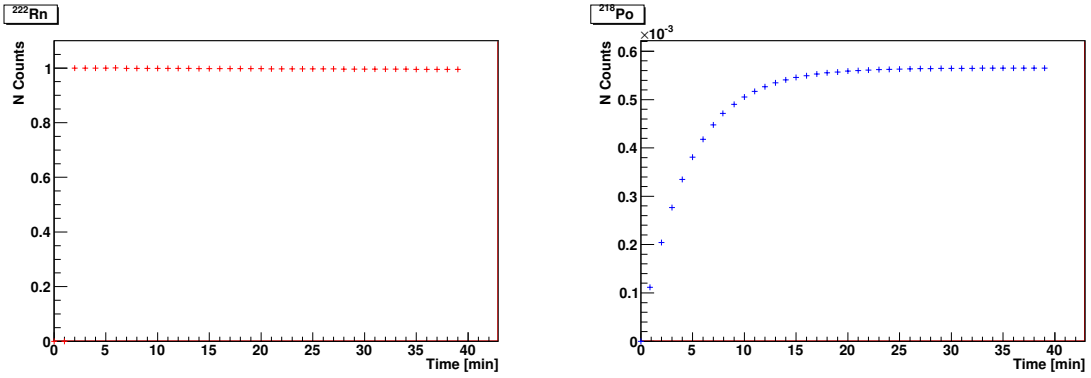

(a) (b)

FIGURE 3.9: Time evolution of normalized number of (a) Radon-222 and (b) Polonium-218 nuclei. The normalization is per radon nucleus.

To solve equation 3.18, we try a solution of the form $N_2(t) = Ae^{-t/\tau_1} + Be^{-t/\tau_2}$ by substituting it into the mentioned equation and with the initial condition $N_2(0) = 0$ we find:

$$N_2(t) = N_0 \frac{\tau_2}{\tau_1 - \tau_2} \left(e^{-t/\tau_1} - e^{-t/\tau_2}\right) \tag{3.20}$$

$$A_2(t) \equiv \frac{1}{\tau_2} N_2(t) = N_0 \frac{1}{\tau_1 - \tau_2} \left(e^{-t/\tau_1} - e^{-t/\tau_2}\right). \tag{3.21}$$

$\tau_1 \gg \tau_2$ case:

In this case the parent nucleus is so long-lived that it decays with a constant rate; for all practical times $e^{-t/\tau_1} \simeq 1$ (see Fig. 3.9) and

$$N_2(t) \simeq N_0 \frac{\tau_2}{\tau_1} \left(1 - e^{-t/\tau_2}\right) \tag{3.22}$$

that corresponds to an activity A_2 that approaches the limiting value of $A_1 \simeq N_0/\tau_1$. The ^{222}Rn α-decay to the ^{218}Po is a good example for this case: in fact $T_{^{222}Rn} = 3.8$ d $\gg T_{^{218}Po} = 3.1$ min (see Fig. 3.9). The maximum of the right plot represents the equilibrium point, where the activity of Radon-222 and Polonium-218 are equal, and thus corresponds to the ratio between the half-lives of the two nuclides. Clearly this number scales as the half-life of the elements.

$\tau_1 > \tau_2$ case:

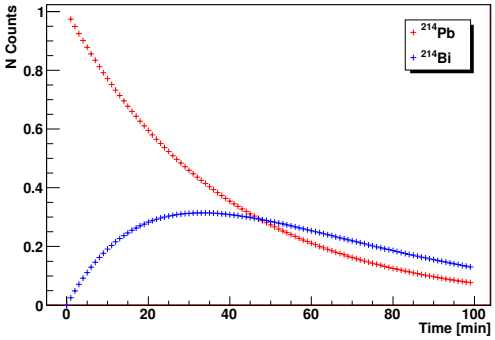

FIGURE 3.10: Time evolution of normalized number of Lead-214 and Bismuth-214 nuclei. The normalization is per lead nucleus.

From equation 3.19 and 3.20 we can calculate the ratio of the two activities:

$$\frac{\tau_1 N_2}{\tau_2 N_1} = \frac{\tau_1}{\tau_1 - \tau_2}\left(1 - e^{-\left(\frac{1}{\tau_2}-\frac{1}{\tau_1}\right)t}\right). \tag{3.23}$$

As t increases, the exponential term becomes smaller and the ratio approaches the limiting constant value $\tau_1/(\tau_1 - \tau_2)$. The activities themselves are not constant, but the nuclei of type 2 decay with the decay constant of type 1. This situation is known as transient equilibrium and is illustrated in Fig. 3.10 for two radionuclides of the lower part of the Rn chain (^{214}Pb and ^{214}Bi).

$\tau_1 < \tau_2$ case:

In this case the parent decays faster. The daughter activity rises to a maximum and then decays with its characteristic decay constant. When this occurs the number of nuclei of type 1 is small and nearly negligible. If t is so long that e^{-t/τ_1} effectively vanishes, then equation 3.20 becomes

$$N_2(t) \simeq N_0 \frac{\tau_2}{\tau_2 - \tau_1} e^{-t/\tau_2} \tag{3.24}$$

which reveals that the type 2 nuclei decay approximately according to the exponential law, as shown in Fig. 3.11 for the ^{210}Bi and ^{210}Po case.

3.5 Principle of surface contamination study

In this thesis work the best tools for carrying out the study of surface contaminations are the alpha and beta emissions of the radon chain nuclides. As a matter of

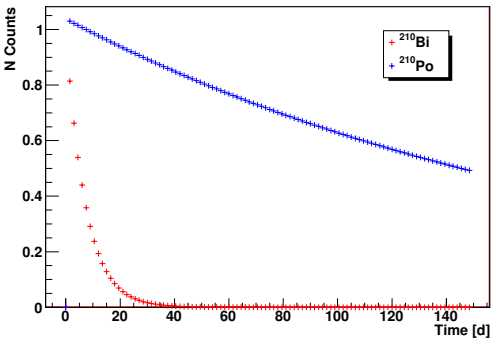

FIGURE 3.11: Time evolution of normalized number of Bismuth-210 and Polonium-210 nuclei. The normalization is per bismuth nucleus.

fact the alphas and betas ionize as a continuum along their track, which allows the analysis of the diffusion profile of surface contaminants on sensitive materials. This study would not be feasable just looking at the few gamma emissions of the chain: 46.5 keV of ^{210}Pb and 803.1 keV of ^{210}Po, which have respectively low energy for the first and a branching ratio as low as respectively 4% and 1.2×10^{-3}%. In fact one has to study the diffusion profile of the radon-induced contaminations, which is really important for the understanding of the possible sources of background in rare event searches (see §3.2).

We have seen that contaminations induced by radon are small, but still enough big to produce background of rare event experiments. A low background detector with the smallest possible dead layer is needed to analyze these contaminations, since the tracks produce by the particle that we are interested in are really small, and the energy deposit in the dead layer must be minimized. Moreover it might be necessary to wait until the secular equilibrium is reached between all the elements of the decay chain on the sample, and this step depending on the elements could take a long period of time. Anyway, the signal to noise ratio is still small because of the low efficiency of the contamination processes. In order to be able to study these types of contaminations it would be better to have a higher signal to noise ratio, so either we reduce the noise or we can intensify the signal source. If we try to further reduce the small background, which is supposed to be already optimized we may also reduce the signal that we are looking for, since we do not know *a priori* which would be the form and the energy of the signal. Thus the best choice would be to use a source which would intensify the signal.

In this work two sources were employed. Both sources were created using radon (uranium) as a primary source for producing polonium and lead contaminants. As

shown in the next chapters these sources were used to see how the induced contaminations behave in terms of: time evolution, contamination profiles and how they affect the sensitivity of DBD0ν and DM experiments.

Chapter 4

CUORICINO and CUORE surface contaminations

The use of bolometric detectors for the search of neutrinoless double beta decay was proposed by Fiorini in 1984 [82]. Since almost thirty years his research group has been developing cryogenic detectors of increasing mass. The successful operation of a 340 g tellurium dioxide crystal [83] was followed by the construction of a detector array composed by 20 crystals, for a total mass of 6.8 kg of TeO_2, that was the MiDBD [84].

The choice of a pure calorimetric approach, and thus no particle identification through the tracking technique, was supported by the very good energy resolution achievable and application of pulse shape analysis for the particle discrimination with bolometers.

In the detector a great mass increase was obtained with the recent CUORICINO experiment [68, 85]. Operated in the Laboratori Nazionali del Gran Sasso in the years 2003-2008, **CUORICINO** was composed by a single tower of 62 tellurium oxide bolometers, for a total mass of more than 40 kg. The experiment sets a lower limit of 2.8×10^{24} years [86] for the DBD0ν half-life of ^{130}Te. At present the CUORICINO results represent one of the most competitive limits for the effective Majorana mass, comparable with the ones obtained with Germanium detectors [17]. Furthermore, it has been a unique test bench for the next generation experiment **CUORE** (Cryogenic Underground Observatory for Rare Events) which is currently getting ready for the construction phase. The excellent performance obtained with CUORICINO is a very good basis to demonstrate the feasibility of

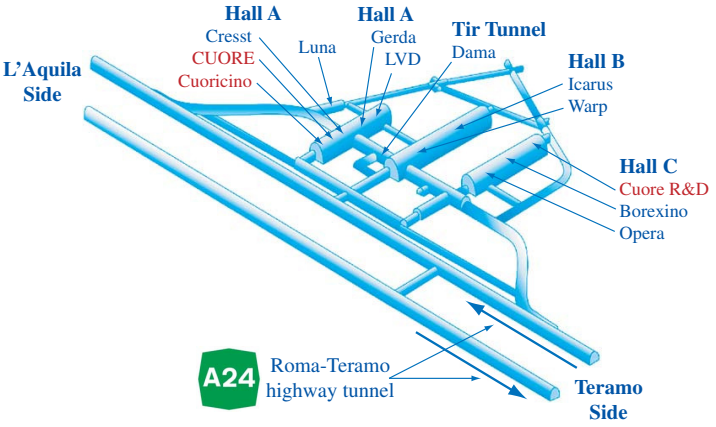

FIGURE 4.1: Map of the LNGS laboratories.

a ton scale bolometric experiment aiming at the investigation of $m_{\beta\beta}$ in the inverted mass hierarchy range. But there are still some important issue concerning the background sources in the region of interest.

4.1 CUORICINO experimental set-up

CUORICINO is an array of 62 TeO_2 bolometers arranged in a tower of 13 floors (see Fig 3.7); 11 of them are made of four 5×5×5 cm^3 crystals, while the two remaining floors are composed by nine 3×3×6 cm^3 crystals: two of them are enriched in ^{130}Te (82%) and the two others are enriched in ^{128}Te (75%). The mass of the big crystals is about 790 g, while the one of the small crystals is 330 g. The total detector mass is 40.8 kg (11.9 kg of ^{130}Te).

The experiment is located in the Hall A of the Laboratori Nazionali del Gran Sasso, under a mountain that provides a 3400 m.w.e. shield against cosmic rays. In this undergound laboratory the muon flux is reduced to about $3{\cdot}10^{-8}$ $\mu{\cdot}cm^{-2}{\cdot}sec^{-1}$ [87] and the neutron flux to about 10^{-6} $n{\cdot}m^{-2}{\cdot}sec^{-1}$ [88]. The mechanical structrure of the tower is made of OFHC (Oxygene Free High Conductivity) copper, and the crystals are fixed to it by mean of Teflon supports. The thermal pulses are read by neutron transmutation doped (NTD) thermistors, thermally coupled to each energy absorber. Since thermal drifts would induce variations in the response of the detectors, the tower is maintained at a constant temperature by a feedback stabilization circuit, fed by the signal of a thermometer that is attached on the mechanical structure of the detector [89]. Fine gain corrections are applied offline by exploiting the fixed energy thermal pulses that are injected every few minutes in the crystals [90]. These stabilization signals are generated by dissipating an

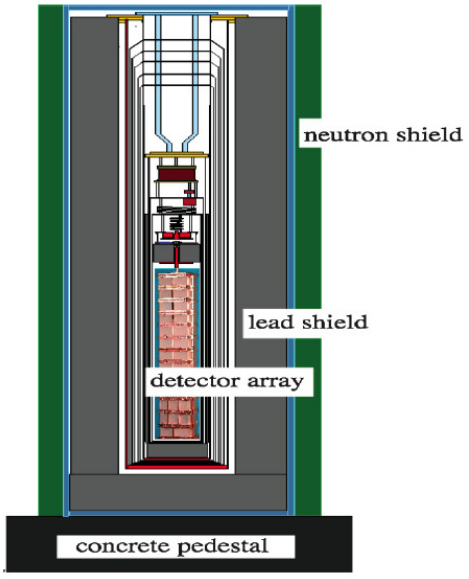

FIGURE 4.2: Sketch of the CUORICINO apparatus showing the tower hanging from the mixing chamber of the diluition refrigerator and the detector shieldings.

electrical pulse of fixed energy on a Si resistor attached to each energy absorber. They have a time duration much shorter than the typical thermal response of the detector. These signals, usually called heater pulses, are flagged by the data acquisition system and are used offline to correct the gain fluctuations induced by temperature drifts.

About once per month a few days energy calibration is performed by inserting ^{232}Th sources between the cryostat and the external lead shields.

All the materials used to construct the CUORICINO tower were selected after thorough check on the radiopurity level and dedicated procedures were developed to clean them. The crystals were grown using previously tested low radioactivity powders by the Shanghai Institut of Ceramics (SICCAS) and were shipped to Italy by boat and stored underground in order to minimize the activation by cosmic ray interactions. The cleaning procedures, as well as the detector assembly, were performed in a N_2 atmosphere, when possible, using glove boxes to minimize surface recontaminations [91].

The CUORICINO tower is hosted in a dilution refrigerator that allows to operate the detectors at a temperature of about 8 mK. To avoid heating due to vibrations the tower is mechanically decoupled from the cryogenic apparatus using a stainless steel spring.

Several shields are used to minimize the background. The tower is surrounded by a 1.2 cm low activity Roman lead layer ($A_{^{210}\mathrm{Pb}} < 4$ mBq·kg^{-1} [92]) mantained at

600 mK to avoid the radioactive background coming from the cryostat radiation shields. The thickness of the Roman lead layer is increased to 10 cm on the top (and on the bottom) of the detector in order to protect it from contaminations in the dilution unit. The cryostat is surrounded externally by two 10 cm thick lead shields. The internal one has an activity of 16±4 Bq·kg^{-1} in ^{210}Pb while the external one is made of standard commercial lead 50 Bq·kg^{-1} (Boliden [93]). The background due to environmental neutrons is reduced by a 10 cm thick borated polyethylene shield. The cryostat is also surrounded by a box continuously flushed with clean N_2 to reduce radon contaminations in the outter part of the cryostat, and it is enclosed in a Faraday cage to avoid electromagnetic interferences.

4.2 The tellurium dioxide choice

The employment of tellurium dioxide crystals as absorbers for the search of DBD0ν with bolometric detectors has undergone exhaustive and convincing validations in CUORICINO (and previous experiments). The choice is motivated by different reasons, some of them are related to the choice of the candidate, others to the cryogenic properties of this material. Double beta disintegration of ^{130}Te occurs through the following channel:

$$^{130}\mathrm{Te} \rightarrow {}^{130}\mathrm{Xe} + 2e^- (+ 2\overline{\nu}) \tag{4.1}$$

The main characteristic of this DBD candidate is that it has the highest natural abundance (η = 33%)compare to other isotopes (see Fig. 4.3). In contrast to other materials, which usually need to be enriched to obtain a sufficient sensitivity in a reasonable detector mass (see equation 2.6), the abundance of ^{130}Te allows to build an experiment with natural Tellurium. This is a great advantage for economic reasons and for radiopurity controls, since the processes that follow the enrichment often introduce radioactive contaminants and make the crystal growth critical.

In addition ^{130}Te has a reasonably high transition energy ($Q_{\beta\beta}$ = 2527±1.0 keV [94]). This corresponds to a high phase space factor ($G_{\mathrm{DBD0}\nu} \sim Q^5$) and a low contribution to the background from DBD2ν (the fraction of DBD2ν counts in the region of the DBD0ν peak scales as $1/Q^5$). Unfortunately, as mentioned in the first chapter, experiments using isotopes with a Q-value above 2615 keV are affected by a much lower radioactive background, but this is not the case of CUORICINO

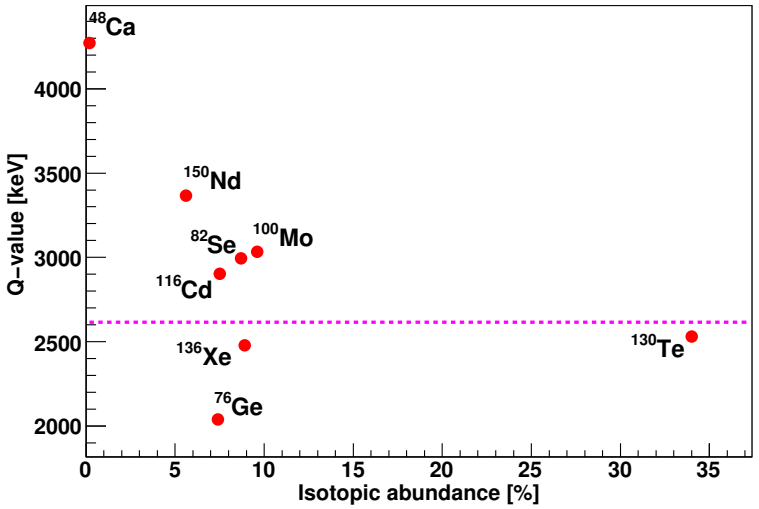

FIGURE 4.3: Natural abundances and Q-value for several DBD0ν isotopes. The dashed lines represents the 2615 keV gamma line.

or CUORE.

The possibility to employ pure Te crystals as bolometers absorbers was taken into account (in order to increase the mass of DBD candidate, leaving the total detector mass unchanged), but it was ruled out mainly because of the poor mechanical properties of this material at low temperatures. Stress caused by the differential thermal contractions occuring between different detector materials revealed to produce excessive damage on pure Te crystals.

4.3 The single module

The CUORICINO detector has a modular structure, where the basic element is represented by a single floor (see Fig. 3.7). The design of the single module must satisfy stringent requirements concerning mechanical properties, thermal performances and radioactivity constraints. Thermal coupling between the crystals and the heat sink, as well as the ones with the NTD sensors, must guarantee good detector performances. At the same time the geometry of the various parts of the single module must be properly designed, preventing the differential thermal contractions from breaking the crystal. All these requirements must meet the most stringent one concerning the low radioactive contaminations of the parts.

A detail image of the CUORICINO single module detector is shown in Fig 4.4. It is composed by four 5×5×5 cm^3 (or nine 3×3×6 cm^3) crystals enclosed

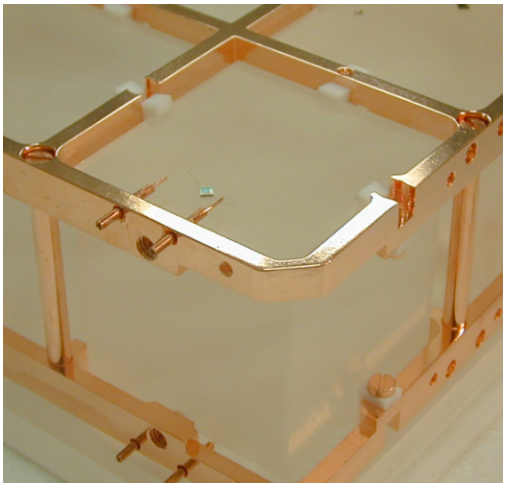

FIGURE 4.4: Detail picture of the CUORICINO single module detector. The crystal is hold by a OFHC copper frame, which is at the same time the thermal bath for the detector. In the picture Teflon holders and NTD sensor are also visible.

in a pair of copper frame which both work as mechanical supports and thermal bath for the absorbers. The two frames are connected to each other by four small copper columns.

The crystals are connected to the copper frames by small Teflon supports that represent the weak thermal conductance between the detectors and the heat sink. They also work as compensator for the different thermal contractions of TeO_2 and copper.

The NTD sensors are glued to the crystals using an epoxy glue (Araldit Rapid). Since a single flat glue deposition would cause the sensor to detach from the crystal surface because of different thermal contractions, the glue is deposited in nine separate spots, with a diameter of 0.7 mm each. The thermal conductance of the glue spots was measured experimentally and the phenomenological relation revealed to be $G \sim 2.6\times10^{-4}$ T^3 [$W\cdot K^{-1}\cdot spot^{-1}$] [95], where T is the temperature in Kelvin. The same gluing technique is employed to apply on each detector the Silicon resistor used for producing heater pulses on the absorber. Electrical connections for both the NTD sensor and the Si resistor are made with two 50 μm diameter gold wires, bonded to metalized surface of the two chips. The wires are crimped on the opposite side into copper pins that pass through the mechanical structure of the single module (see Fig. 4.4).

4.4 CUORICINO: background and results

CUORICINO data taking started in March 2003. Several wiring connection broke down during the cool down of the detector, so that only 49 channels out of 62 were able to acquire. Since the active mass was still quite large (about 30 kg of tellurium dioxide) and the detector performances were satisfactory, data taking continued for few months. In November 2003 the tower was warmed up at room temperature in order to recover the lost channels and to perform maintenance operations of the cryostat. Data taking restarted in May 2004 with the full operation of all 62 channels. This interruption set a marking point dividing the data taking in Run 1 and Run 2.

The performances of the detectors were excellent, the average energy resolution was 7 keV for the big crystals and 9 keV for the small ones. The best detectors had a resolution of 5 keV. Energy resolution was evaluated as the FWHM of the ^{208}Tl 2615 keV gamma line observed in the calibration measurements. Similar energy resolution was obtained from the same peak in the background measurements summed over long time periods. Excluding the interruptions for the maintenance of the cryogenic apparatus, the live time of the experiment was about 40%.

4.4.1 Background study

The background measured by CUORICINO can be seen as the results of two different sources, depending on whether it comes from outside the detector (external background) or from the detector itself and the passive materials that surround it (internal background).

External background is produced by neutrons, muons and natural radioactivity in the underground laboratory. It can be reduced down to a negligible level by proper shieldings (see §4.1).

Internal background comes from the radioactive contaminations in the cryostat radiation shields, the mechanical structure of the tower and the crystals themselves. Apart for the most external cryostat radiation shields, from which the crystals are protected by a low radioactivity Roman lead layer, there is no way to protect the detector from the internal background sources, due to the lack of a veto or a dead layer. The only available solution is to eliminate them by proper material selection and cleaning.

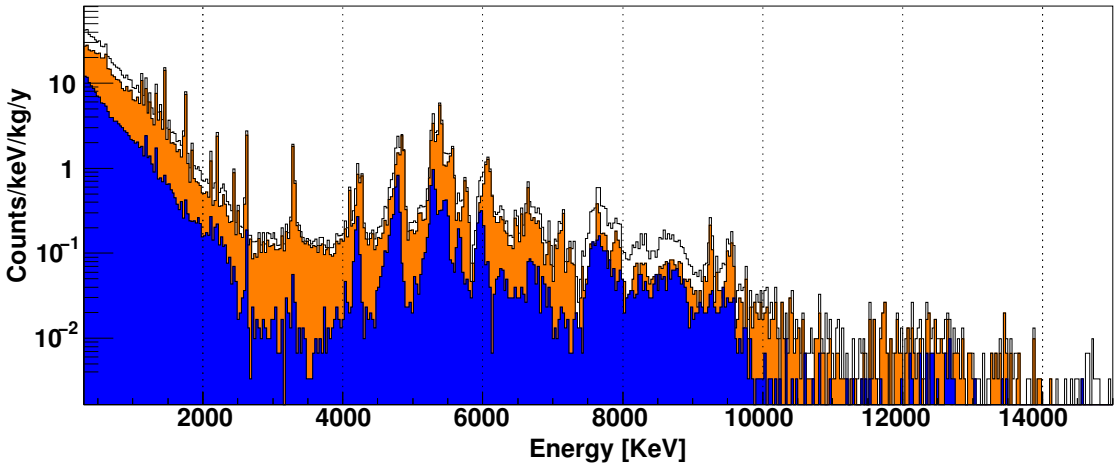

FIGURE 4.5: Full background energy spectra acquired by CUORICINO big crystals. The blue histogram represents the double hit spectrum (two events in the same time window of 100 ms), the orange histogram is the anti-coincidence spectrum (single hit in a coincidence window of 100 ms) and the black one is the total energy spectrum.

The background measured by the big CUORICINO crystals is plotted in Fig. 4.5. It was obtained by summing up the single crystal energy spectra over the whole data taking of the experiment. The three histograms represents the single hit, double hit and total energy spectra. Single hit spectrum is obtained using the detector array as a veto, thus selecting events in which only one crystal was hit within a coincidence time window of 100 ms. Double hit spectrum is obtained selecting events that hit two crystals in the same coincidence time window.

The DBD0ν detection efficiency has been evaluated using Monte Carlo simulations: in 88% of the cases the two emitted electrons are fully contained in the crystal where the decay occurs. Therefore the DBD0ν signal should appear as a peak at Q-value of the disintegration in the single hit spectrum. Thus, the capability of operating the detectors in anti-coincidence allows to reduce the background. Due to the way in which the crystals are arranged, this cut is not much effective for CUORICINO, but it will play a fundamental role in the tight-packed structure of CUORE. Even in CUORICINO, by studying the differences between coincidence and anti-coincidence spectra it is possible to extract important informations concerning the nature and the location of background sources.

CUORICINO background was as low as 0.18 counts$\cdot$keV$^{-1}\cdot$kg$^{-1}\cdot$y^{-1} in the DBD0ν region, the main contributions are listed in Table 4.1.

As shown in Fig. 4.6 the background is different at lower energy and higher energy than the 2615 keV peak. This line, from the Thorium chain, is the only γ

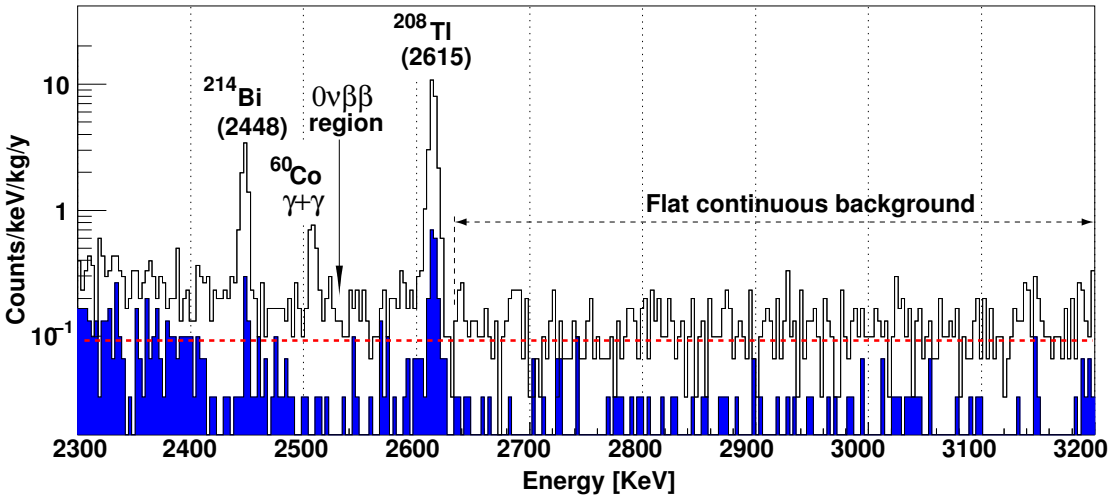

FIGURE 4.6: CUORICINO background in the ROI. The blue histogram represents the double hit spectrum, while the black one is the single hit.

contribution to DBD0ν background, through scattering Compton. The other two lines appearing in the spectrum are the 2448 keV line from ^{214}Bi and the 2505 keV sum line of two ^{60}Co gammas produced in the copper structure. If the energy resolution is good enough (as it is the case for CUORICINO), these two sources give a negligible contribution to the DBD0ν region.

By comparing the intensities of the ^{208}Tl gamma line with other lower energy gammas from the same isotope (e.g. 277 keV, 583 keV and 860 keV) it is possible to obtain informations concerning the location of the Tallium source. The Th gamma contamination is located relatively far from the detector, probably in some external cryostat thermal shield. Based on the guess of the source position, the contribution from the ^{208}Tl line to DBD0ν background reported in Table 4.1 was obtained using Monte Carlo simulations.

The background measured by CUORICINO in the high energy region (higher than 2615 keV) is produced mainly by degraded α from the Uranium and Thorium contaminations that are located on the crystals and on the passive materials surrounding the detectors. They produce a continuum in the energy spectrum

TABLE 4.1: CUORICINO background sources

Source	^{208}Tl	DBD0ν	3-4 MeV
Surf. Cont. TeO_2 ^{238}U and ^{232}Th	-	10±5%	20±10%
Surf. Cont. Cu ^{238}U and ^{232}Th	15%	50±20%	80±10%
Bulk Cu shields in cryostat ^{232}Th	85%	30±10%	-

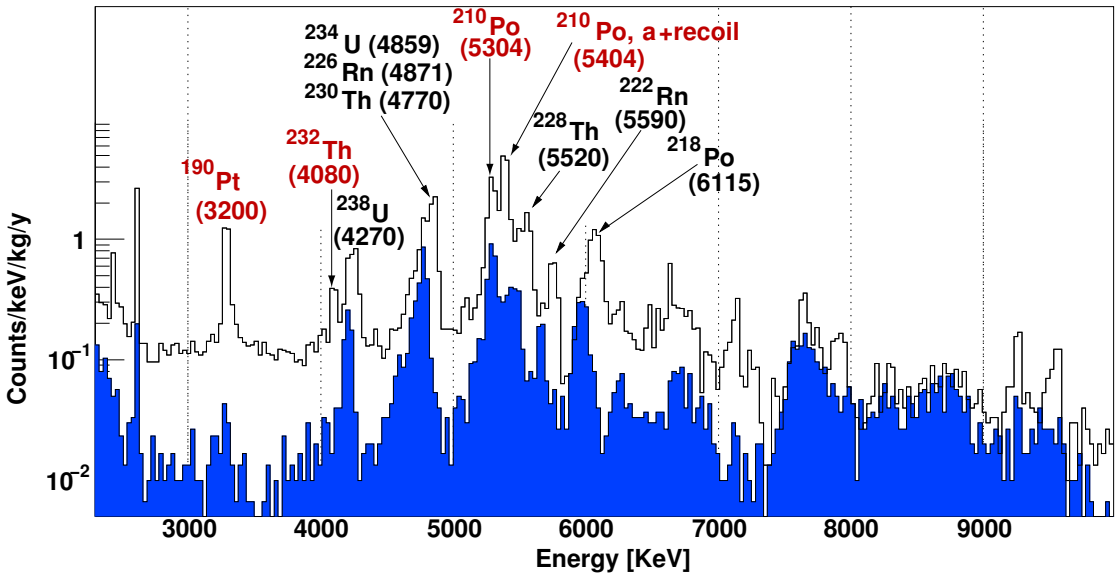

FIGURE 4.7: CUORICINO background in the α region. In blue is plotted the double hit spectrum, while in black the single hit spectrum.

that extends to low energy (lower than 2615 keV) giving a contribution to the background in the DBD0ν region. As shown in Fig 4.7 the α peaks can be easily identified in the CUORICINO energy spectrum. From the study of their position and shape it is possible to extract informations on the location of the radioactive contaminants (see Fig. 4.8).

If the source is located within the crystals, both the α particle and the associated nuclear recoil release their energy inside the crystal and a sharp Gaussian

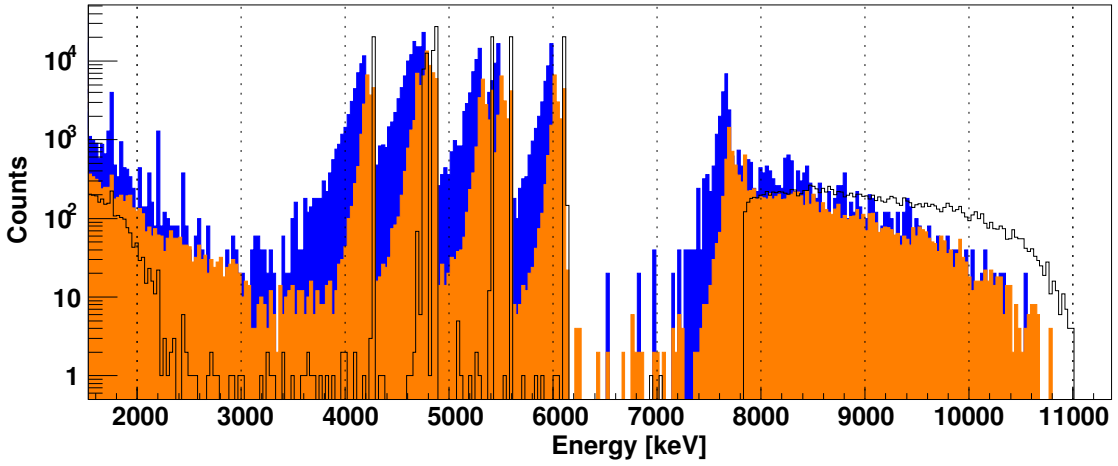

FIGURE 4.8: Simulation of CUORICINO Uranium alpha background. The orange histogram represents crystal surface contaminations, the blue one copper surface contaminations and the black one crystal bulk contaminations. Surface contaminations have been simulated with an exponentially decaying density profile and 1 μm of thickness.

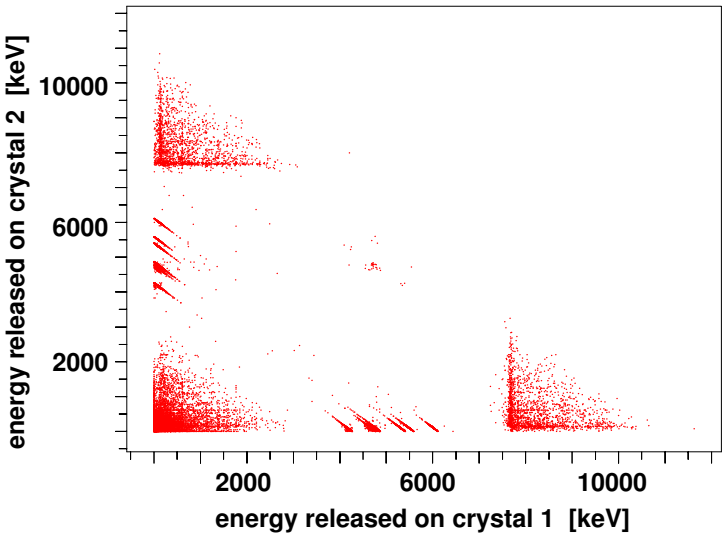

FIGURE 4.9: Scatter plot of coincidence events (double hit) for CUORICINO.

peak is produced in the spectrum. In case the contamination is located on a very thin layer in the vicinity of the crystals or the passive materials, the α particle can escape retaining almost all its energy and can hit another crystal. Even in this case a Gaussian peak is produced, whose position is given by the energy of the α particle only (no recoil energy). If instead the surface contaminations are deep enough, even a part of the α energy is released in the material where the radioactive decay occurs. In case this material is a crystal, a peak with an asymmetrical long energy tail is produced. If instead the decay occurs on a passive material, only a flat continuum will appear in the energy specrum. Besides the analysis of spectral shapes, further informations on the location of the contaminants can be extracted from the study of coincident events (see Fig 4.9). In the case they are located on crystal surfaces, there is a non negligible probability that the escaped α was detected by a neighbour crystal. This would result in two detectors recording a signal at the same time and whose sum energy is equal to the total transition energy of the decay (α + recoil). Obviously this feature is not present if the contaminant is located in the passive materials, as the fraction of energy that has been released can not be detected.

In CUORICINO most of the α peaks in the region above 4 MeV are produced by Uranium and Thorium surface contaminations of the crystals: these peaks are visible both in single and double hit spectra, and they have a long low energy tail that rules out the possibility of internal contaminations. These are however few exceptions (see Fig. 4.7, orange spectrum):

- 3200 keV is the internal ^{190}Pt contamination of the crystals: the peak is

Gaussian and no peak appears in the coincidence spectrum. The crucible of the crystals is made of Platinum, this might be the primary source of contamination;

- 4080 keV is due to ^{232}Th internal contamination. This peak grows on the tail of the ^{238}U contamination (at 4270 keV);

- 5304 keV is produced by a contamination of ^{210}Po. The interesting feature observed is that the polonium activity does not seem to decrease along with the time ($T_{1/2}^{^{210}Po} = 138$ d), for long time periods. This is a clear proof that there must be also an important contamination of ^{210}Pb, which continuously feed the polonium level, in a way that the activity of ^{210}Po is unchanged. The position of the peak (centered at the α energy, and not at the Q-value of the transition) indicates that the contamination has to be on a very thin layer either on the crystal surface or on the passive materials surface facing the detectors. From the scatter plots it is then possible to conclude that at least part of the peak is produced by a contamination of the crystal surfaces;

- 5404 keV is due to the bulk contamination of ^{210}Po. Usually observed in recently grown TeO_2 crystals, this peak produces no events in the double hit spectrum. However part of the peak is a consequence of the Uranium and ^{210}Pb surface contamination discussed above.

While the sources of the α contaminations are rather understood, it is quite a complex task to characterize the continuous background that extends down to the DBD0ν region. It is difficult to associate it to a particular α peak (or tail) and to identify the corresponding contaminant. Based on measurements made before the construction of CUORICINO, and on several dedicated tests performed on the R&D apparatus, major contributions from neutrons and from the small parts of the detector can be excluded.
Therefore most of the flat background measured by CUORICINO between 3-4 MeV should come from crystal and copper surfaces contaminations. Given the amount of events in the double hit spectrum in this 3-4 MeV range it is possible to conclude that a negligible fraction of the flat continuum has its source not in the crystals.

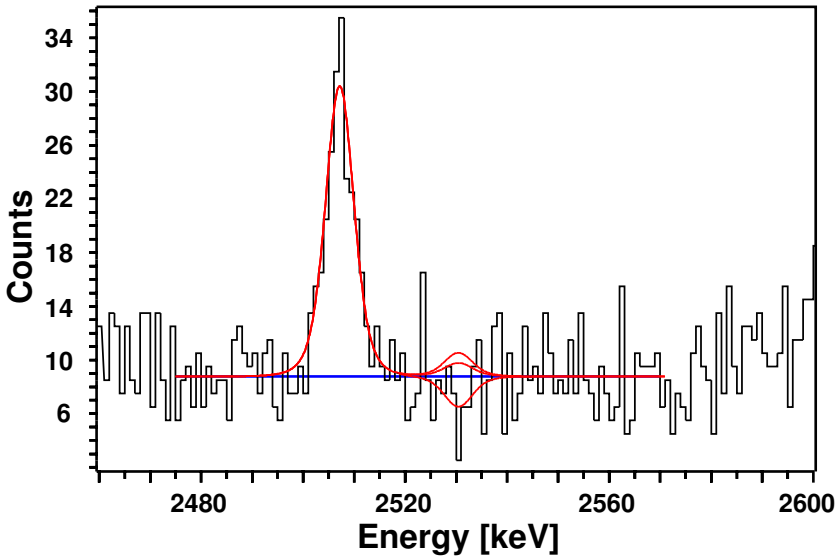

FIGURE 4.10: CUORICINO single hit background spectrum summed over all detectors. The red lines represent the best fits at 68% and 90% C.L. on the number of events under the DBD0ν peak, while the blue line represents the continuum background in the region of the DBD0ν.

4.4.2 CUORICINO results

For computing the half-life of the DBD0ν it is necessary to analyse the single hit energy spectrum collected by CUORICINO in the DBD0ν region (see Fig. 4.10). It was obtained by summing the spectra from all detectors during the whole data taking period and corresponds to a total statistics of 19.75 kg·y in ^{130}Te.

In order to evaluate the half-life limit, the peaks and the continuum in the DBD0ν region were analyzed using a maximum likelihood method [5]. The six energy spectra acquired (2 Runs times 3 crystal types) were combined allowing a different background level, and a different intensity of the 2505 keV ^{60}Co peak. Other free parameters are the position of the ^{60}Co peak and the number of counts under the DBD0ν peak. The response function for each spectrum was assumed to be a sum of symmetrical Gaussian functions, each having the typical energy resolution of one of the detectors summed in that spectrum. Assuming a flat background, the fit in the region between 2470 keV and 2580 keV yields a negative number of counts under the DBD0ν peak (-13.9$\pm$8.7). The resulting upper bound for the number of candidate events under the peak is $n = 10.7$ at 90%. This limit is then assumed to come from the sum spectrum of the entire statistical data set in which each of the six spectra is weighted on the corresponding live time t, geometric efficiency ϵ and number of ^{130}Te nuclei N. In terms of these parameters

the number of expected counts can be written as:

$$n = \ln 2 \frac{1}{T^{0\nu}_{1/2}} \sum_{i=1}^{6} N_i \, \epsilon_i \, t_i. \tag{4.2}$$

The resulting lower limit on the half-life of ^{130}Te is:

$$T^{0\nu}_{1/2}(^{130}Te) \geq 2.8 \times 10^{24} \; y \qquad (90\% \text{ C.L.}). \tag{4.3}$$

Systematic uncertainties in the evaluation of the half-life limit come from the live time and from new measurement of Q-value.

Extracting the effective Majorana mass of the electron neutrino from the half-life requires the calculation of the nuclear matrix elements. Since these calculations depend on the model and on the selection of a number of parameters, the results from different authors give a significant spread, even for the same nucleus. Using the best and the worst case, the CUORICINO lower limit on the DBD0ν half-life of ^{130}Te corresponds to:

$$m_{\beta\beta} < 0.3 \; - \; 0.7 \text{ eV [96–99]}. \tag{4.4}$$

4.5 The CUORE experiment

Next generation double beta decay experiments aim at exploring the neutrino mass range corresponding to the inverted mass-hierarchy pattern (see Fig. 2.4). This will require a sensitivity on $m_{\beta\beta}$ of few tens of meV, which is about one order of magnitude lower than the present results. This goal can be reached by an important increase of the DBD0ν mass candidate and by a strong background reduction in the region of interest.

The CUORE experiment [19] will search for neutrinoless double beta decay in ^{130}Te using an array of 988 TeO_2 bolometers, with an entire mass of tellurium dioxide of about 740 kg. Compared to CUORICINO, the detector mass will be increased by a factor of 20 and the background will be reduced (in the optimistic case) by the same amount. The data taking of CUORE is foreseen to start in 2013: after 5 years of continuous data taking a sensitivity of about 10^{26} years is expected on the DBD0ν half-life of ^{130}Te. Even if the mass increase will require

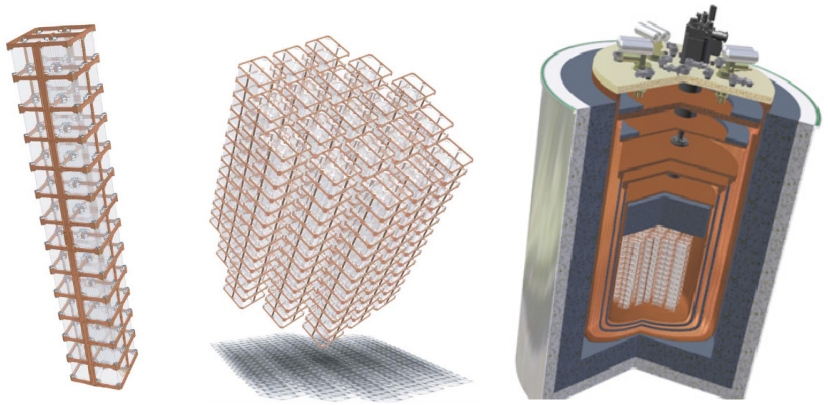

FIGURE 4.11: 3-dimensional sketch of a single CUORE tower and the whole detector.

much effort, mainly due to technological issues concerning the cryogenic apparatus, the biggest challenge will be the achievement of a sufficient low background level. The baseline of the CUORE collaboration is to reach a background of $\sim 10^{-2}$ events·keV^{-1}·kg^{-1}·y^{-1} in the DBD0ν region. This background level corresponds to observing less than 1 count per crystal over 10 years in an energy window of 10 keV centered at the Q-value of the decay.

4.5.1 CUORE: detector

The CUORE experiment will be composed by an array of 988 not-enriched TeO_2 bolometers. As for CUORICINO, the crystals will have a dimension of 5×5×5 cm^3, and a mass of about 750 g each. The total number of ^{130}Te nuclei will be about 9.4×10^{26} ($\sim$205 kg). The geometry of the CUORE detector is shown in Fig. 4.11. The 988 crystals will be arranged in a cylindrical structure organized into 19 towers. Each tower will have a structure really close to the CUORICINO one, and will be made of 13 floors, each floor being composed by four crystals.

The thightly packed structure of the CUORE array will take great advantage from the high background rejection capability that can be obtained by operating the detectors in anti-coincidence mode. Since there is a small probability for the two electrons of DBD0ν to escape from the crystal where they are emitted, a simultaneous hit in more than one detector is an indication of a background event. In contrast to CUORICINO, most of the crystals will be completely surrounded

by other detectors, thus allowing an easier identification of crystal surface contaminations.

CUORE will be operated underground, in the Hall A of the Laboratori Nazionali del Gran Sasso where the 3400 m.w.e. rock shielding reduces the muon and neutron fluxes.
The entire array, surrounded by a 6 cm thick lead shield, will be operated at about 10 mK in a ^{3}He/^{4}He dilution refrigerator. An other shielding of 25 cm of low activity lead will be positioned on the top of the detector array in order to shield it from the materials in the dilution unit of the refrigerator and from the environmental radioactivity. A borated polyethylene shield will protect the detector from neutrons and an anti-radon air-thight cage will surround externally the cryostat.

Despite the biggest challenges of the CUORE experiment that are the mass increase and background reduction, several other aspects of the detector have been revised in order to cope with the increased number of detectors. For example the mechanical structure of the towers has been redesigned to allow a simpler assembling procedure and to guarantee better energy resolution and more uniformity in the response of different detectors.

Given the packed structure of CUORE, the energy calibration procedure had to be redesigned. While in CUORICINO the calibration sources could be positioned at room temperature, outside of the cryogenic apparatus, a uniform and fast enough calibration of the CUORE array will require to periodically insert the sources inside the cryostat, and therefore to cool them at 10 mK and warm them up again. The calibration system will have to introduce thermal loads that can be afforded by the cryogenic apparatus, and will have to guarantee a reliable operation during the whole live time of the experiment. Moreover the position of the sources, as well as their intensity, will have to be optimized to reduce the loss in detector live time due to calibration.

The analog part of the readout chain will be almost identical to the CUORICINO one.

4.5.2 CUORE: shieldings and cryogenics

Including the detector copper support structure and the radioactivity lead shieldings, the total mass to be cooled in CUORE will be of about 10 tons. Refrigerators with the required power are technically feasible, as was demonstrated by the

gravitational wave antenna experiments [100]. However, because of the stringent radioactivity requirements, the CUORE refrigerator will have to satisfy several requirements that are rather uncommon in standard cryogenic devices.
The design must satisfy the following set of requirements:

- base temperature lower than 10 mK, in order to have optimal detector operation;
- volume to be cooled down almost 1 m^3;
- cooling power of the refrigerator will have to account for the thermal load produced by the ∼2600 wires running from 10 mK to room temperature;
- vibrations transmitted to the detectors must be minimized;
- the experience acquired with CUORICINO shows that the experiment must be properly shielded to reduce at a sufficient level the background coming from the ^{232}Th contaminations in the cryostat thermal shields;
- employment of radiopure materials for the shielding structure;
- employment of a stable, service-free and high duty-cycle apparatus.

The cryostat (see Fig. 4.12) will be made of six nested vessels. The outer vacuum chamber (OVC), maintained at room temperature, and the inner vacuum chamber (IVC) maintained at about 4 K, will be separated by an intermediate radiation shield that will operate at a temperature of ∼40 K. Additional thermal radiation shields will be provided by 30 layers of Multilayer Insulation (MLI) covering the 40 K shield and by 10 layers on the IVC shield, the amount of MLI being limited by radioactivity constraints.

The cooling of the IVC and of the 40 K radiation shield will be provided by five Pulse Tubes mounted on the OVC top flange.
The detector will be cooled by a ^{3}He/^{4}He dilution refrigerator especially designed for CUORE by Leiden Cryogenics. It is a DRS-2000 unit modified to run without cryogenic liquids: a Joule-Thompson heat exchanger will replace the functionalities usually provided by the 1 K pot. The expected cooling powers are: >1.5 mW at 120 mK, 30 μW at 20 mK and 5 μW at 12 mK.
Inside the IVC there will be three thermal shields connected respectively to the Still plate (∼500 mK), to the cold plate (∼50 mK) and to the mixing chamber (∼10 mK).

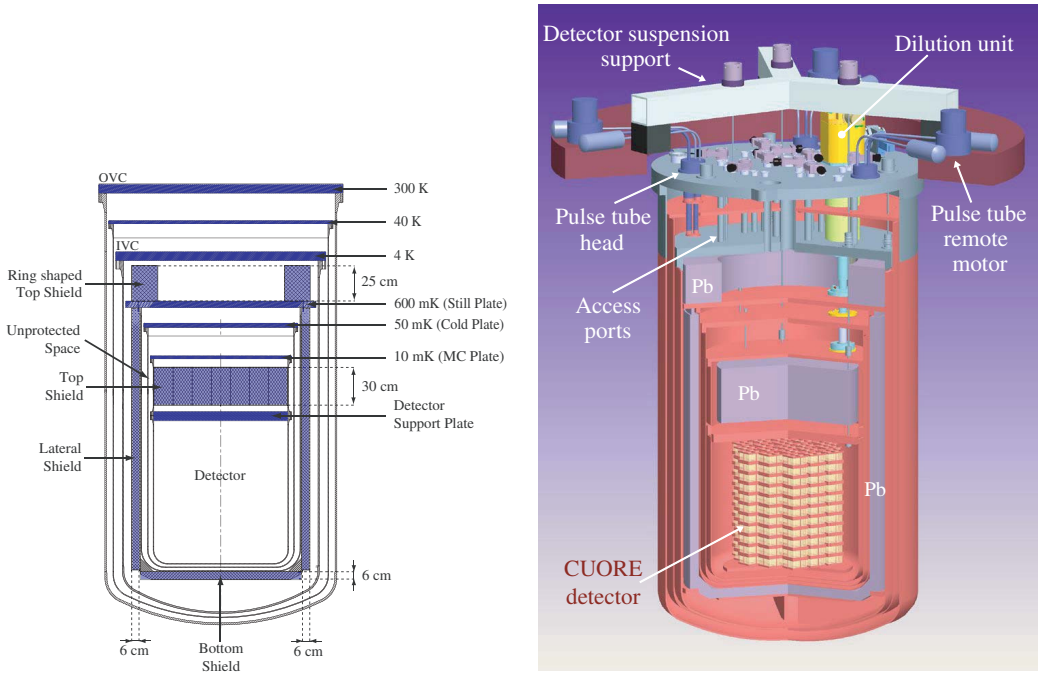

FIGURE 4.12: CUORE (a) internal shields and (b) cryostat.

Inside the cryostat there will be three lead shields to protect the experiment from environmental radioactivity and from contaminations in the construction materials.
A 25 cm thick lead shield is positioned outside the OVC, it will protect the detector from the bottom and from the sides. An equivalent shield from the top will be hosted inside the cryostat, just above the detector. It will be placed between the mixing chamber plate and the detector, but it will be thermally linked to the 50 mK radiation shield. With a 30 cm thickness and a 90 cm diameter it will weight about 3300 kg. A lead ring-shaped shield placed on the Still flange (see Fig. 4.12a) will close the gap between the lead disk above the detector and the outer room temperature shields. An additional 6 cm lead shielding (5400 kg) will be installed just outside the Still shield.

To accomplish the radiopurity constraints, the cryostat radiation shields are made of selected high purity copper that has been already delivered and stored in the LNGS to prevent cosmic activation and will be brought to surface only for machining and cleaning to build the cryostat.
The detector suspension has been designed to minimize the transmission of mechanical vibrations produced by seismic noise and by the operation of cryocoolers and pumps.

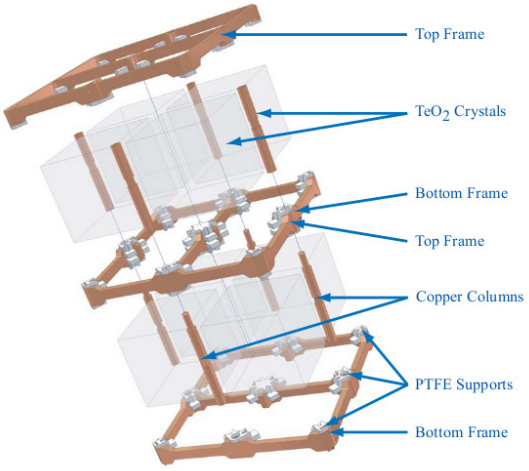

FIGURE 4.13: Pictorial view of a CUORE detector module.

4.5.3 CUORE: assembly

In CUORICINO each group of four crystals was hold together by a pair of copper frames, and this single module was replicated as many times as the number of floors in the whole tower. In the new design the same copper frame will be used both as a top frame and as a bottom frame for two adjacent floors (see Fig. 4.13). This simple modification makes the assembly procedure easier (thus faster) and at the same time reduce the amount of copper needed of 50%. This feature is really important since the copper was the most important background source in CUORICINO (as shown in Table 4.1).

In order to avoid material recontaminations, all the assembling procedures will be perfomed in a nitrogen fluxed environment using custom design glove boxes that will prevent any direct contact with the detector materials. For this purpose a dedicated clean room is being built within the CUORE hut, as well as a clean area to store the materials between their arrival at the LNGS and the assembly of the towers. In any case because of radon mobility, the Rn concentration will be reduced as much as possible in the clean room ($\sim$100 mBq$\cdot$m^{-3}).

4.5.4 CUORE: background reduction

As already mentioned the main contributions to the CUORICINO background in the DBD0ν region are produced by ^{232}Th contaminations in the cryostat radiation shields and by surface contaminations in the crystals and in the copper used for the structure of the tower. While the background coming from the ^{232}Th is rather

understood and will be easily reduced by the 6 cm thick lead layer that will be placed outside the 600 mK radiation shield, the contaminations in crystal and copper surfaces have a less clear signature and represent the main obstacle towards the background goal of 10^{-2} events·keV^{-1}·kg^{-1}·y^{-1} foreseen for CUORE.

In the next section we will analyze the possible mechanisms that lead to those surface contaminations.

4.6 ^{210}Po and ^{210}Pb surface contaminations

In section §4.4.1 it was demonstrated that ^{210}Po (and ^{210}Pb) are the main sources of surface contaminations in CUORICINO. In section §3.3 we have illustrated the main possible mechanisms that lead to surface contaminations. We can merge these two information analyzing the surface contamination of CUORICINO components voluntarily polluted with Polonium-210 and Lead-210, through a radon exposure of various material samples. The aim is to understand the mechanism of surface contaminations and to evaluate if the CUORICINO ^{210}Po contamination could be attributed to radon exposure of the detector during the assembly procedures, even if for the assembly many precautions were taken in order to minimize the radon exposure: the assembly was carried out in a clean room, inside glove boxes continuously flushed with N_2 gas. The effective radon concentration in the environment probably did not have still an enough low value to prevent the contamination of the detector. Thus a study concerning the link between radon exposure of construction materials and ^{210}Po (and ^{210}Pb) contaminations is needed. A parameter that can quantify the radioactive contaminations of samples after a radon exposure is the *Sticking Factor*.

4.6.1 The Sticking Factor

We define the Sticking Factor (Σ) for radon as the ratio between the number of radon nuclei that stick on a sample and the total number of nuclei which have a probability (dP) different from 0 to stick on it:

$$\Sigma_{Rn} = \frac{N(dP = 1)}{N(dP \neq 0)}. \tag{4.5}$$

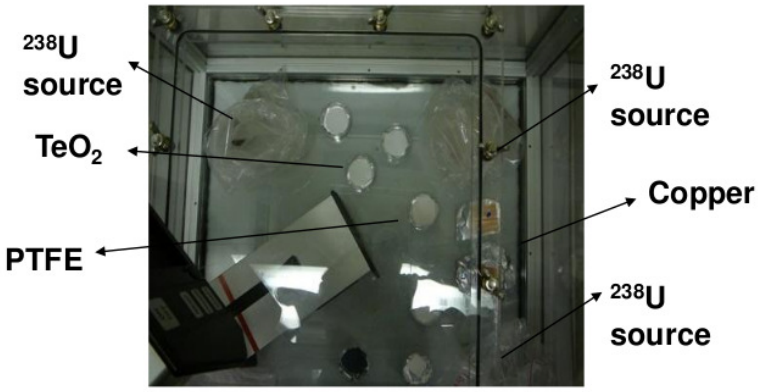

FIGURE 4.14: Experimental set-up for the Rn exposure: an insight into the Rn-box.

Certainly Σ_{Rn} is a function of the radon concentration, of the time exposure and of the material features. During the development of this work all these dependences have been taken into account.
When a material sample is exposed to an atmosphere rich in some radioactive element (e.g. Rn), there will be different mechanisms that will bring to the contamination of the sample. Mainly there are three processes: the first is the deposition of the particulate that have bound to the radioactive elements of the atmosphere (e.g. aerosols); the second mechanism is the diffusion of radon through the material and finally the third is the nucleus recoil implantation as the consequence of the nuclear decay.

4.6.2 Experimental set-up

In order to perform the Σ_{Rn} evaluation, it is necessary to place samples in a monitored atmosphere rich in radon. So, a plexiglass box with hermetic closing was built, and three radioactive sources of ^{238}U were installed inside. The atmosphere was monitored with radon detectors placed inside and outside the box: this configuration allowed us to evaluate any possible radon flux to and from the radon-box (see Fig. 4.14).

The background measurement was just run placing the radon detector inside the Rn-box and thightly closing it. The results shown in Fig. 4.15 demonstrate that the enclosure is not perfectly hermetic to Rn, but it still has a good insulation. Indeed the decay constant of the exponential fit of the measured activity is slightly higher ($T_{1/2}$=5.8 d) compared to the theoretical one ($T_{1/2}$=3.8 d). The decrease

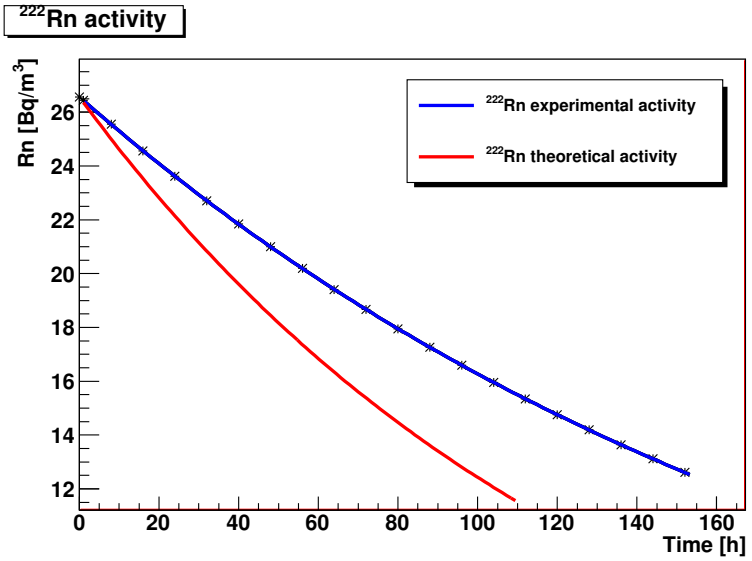

FIGURE 4.15: Radon concentration inside the Rn-box (blue line) and theoretical value (red line).

in activity is simply due to the radon decay, and the absence of any parent nuclei that can feed the radon level.

This difference will be completely washed out by introducing ^{222}Rn sources in the box. Another measurement was run (in the same background configuration) placing three ^{238}U sources (rocks) inside. The radon concentration inside the box was evaluated and is presented in Fig. 4.16. In this case the Rn concentration is still smaller compare to the theoretical value, but the reason is different. In fact now we are dealing with much bigger activity, hundreds of kBq, while in the previous case it was just a few Bq. The difference between the two curves is due to the presence of more than one mechanism of radon emanation from the rocks: surface emanation and bulk emanation. The first mechanism produces prompt radon which is injected in the environment right after its production, while the second one instead is delayed because of the time needed for the gas to diffuse inside the source (Uranium rocks) and to reach the surface. The weighted mean of the time constant of the two processes reduces the effective Rn half-life. The experimental curve was obtained fitting the data with equation 3.22.

In the Rn-box slabs of various materials were placed. The samples selected were obviously: OFHC copper, TeO_2; all the main components of the CUORE detector. All the copper and tellurium dioxide slabs were treated in the same way (machining and cleaning procedures) before the exposure.

Sample	Material	Exposure time [days]
Rame_OFHC	Copper	56
Rame_BaseMen	Copper	63
TeO2_1Mis	Tellurium Oxide	49
TeO2_2Mis	Tellurium Oxide	73
Rame_OFHC_brv	Copper	16
TeO2_brv	Tellurium Oxide	14

TABLE 4.2: Samples exposed to radon (in chronological order of exposure)

4.6.3 Analysis of the samples

The radon concentration was monitored during the whole exposure time. The saturation regime of Rn concentration was reached after about two weeks, with a value of 315 kBq·m^{-3}. The samples were exposed to the high radon concentration atmosphere for almost 2 months.

The analysis of the contamination of the slabs was performed with alpha spectroscopy employing a surface barrier Silicon detector in a vacuum chamber (about 7 μm Hg); the active surface of the detector is 1200 mm^2 and the dead layer is 50 nm thick. The analyzed samples have a surface of 2500 mm^2 and during the measurement they were placed right in front of the detector in order to maximize the geometric efficiency of the measurements, which is evaluated with Monte Carlo simulation to be 10%.

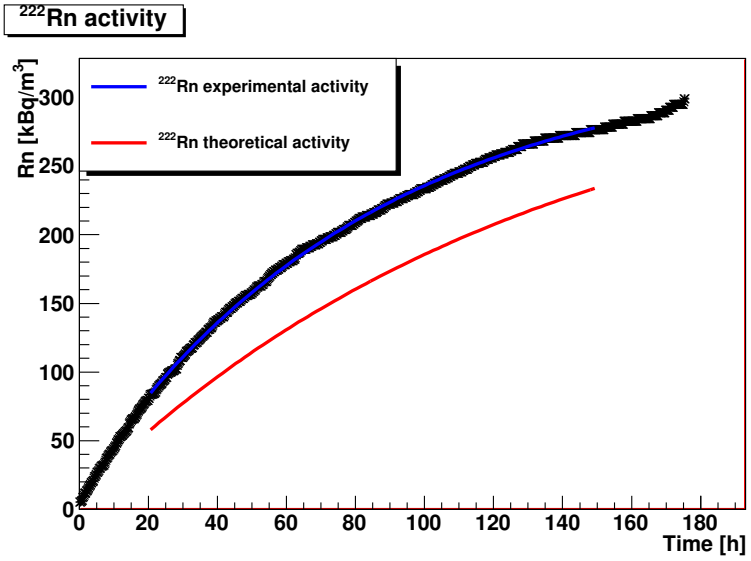

FIGURE 4.16: Radon concentration inside the Rn-box (blue line) and theoretical value (red line).

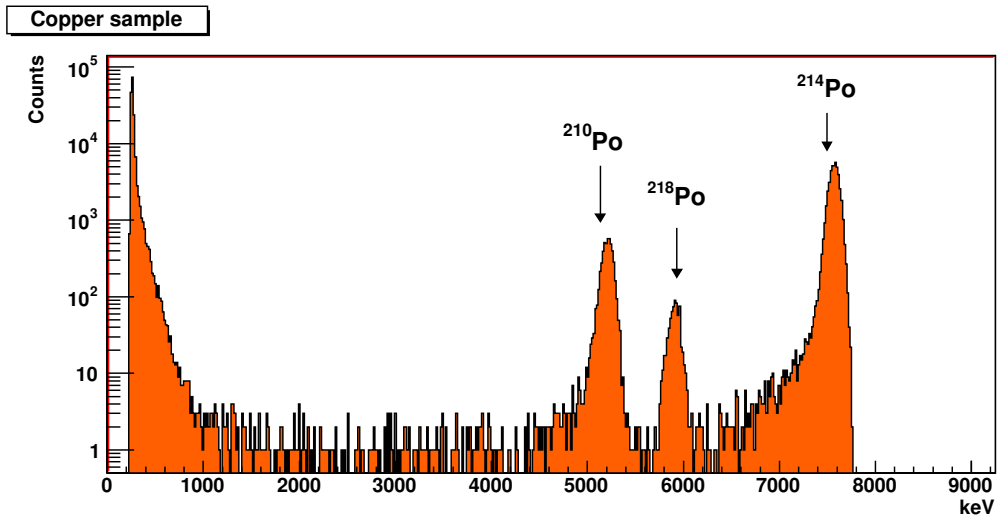

FIGURE 4.17: Acquired spectrum of an exposed copper sample.

The samples were measured one at the time (in Fig 4.17 is shown a standard acquired spectrum). The only contaminations visible on an acquired spectrum are the alpha emission of ^{218}Po (6.0 MeV), ^{214}Po (7.6 MeV) and ^{210}Po (5.3 MeV) decays. This means that we are able to see almost all the nuclei of the Rn chain that decay through the alpha channel, except for the ^{222}Rn (5.5 MeV) which seems to be not present or hidden by the other signals.
Before and after every measurement of the sample a background measurement was run. No ^{210}Po excess was found in the background (see Fig. 4.18).
The analyzed samples and the exposure time are listed in Table 4.2.

Looking at Fig. 4.17 it is clear that the peaks are not symmetrical. In fact there is a convolution of a *Gaussian peak* and a *tail* that starts a few FHWM away from the Gaussian centroid and extends to lower energy. But there is still an issue concerning the length of the tail: in fact it is hard to understand where it ends up. Actually it fades out in the continuum background down to 3 MeV, and at the same time it is the superposition of different tails depending on the number of peaks in the spectrum. In the next section we will present in more detail all the tail analysis and we will describe the reason of the exponential choice for the lower energy fit.

In order to understand the dynamics and mechanisms of the contamination, we must understand what is going on inside the Rn-box. So for the sake of the argument we will analyze the differential activity of the samples for the different polonium isotopes. This will give us information about the contamination levels inside the box. The activity that we are going to consider are computed just considering the symmetrical part of the alpha peak, for reasons previously mentioned.

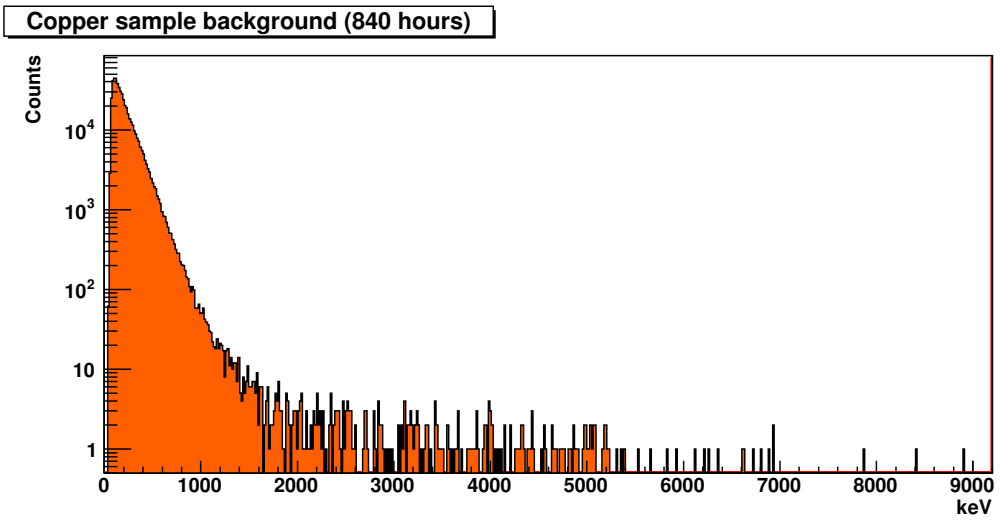

FIGURE 4.18: Background measurement of a copper sample. The measurement lasts 840 hours.

However the events that are in the tail are a small fraction of the overall activity (about 15%), assuming the continuum contribution negligible.

We compare the plots in Fig. 4.19, which show the differential activity measurements (that are just the difference of two acquired spectra of the same sample), for each polonium nuclide for a copper and a tellurium dioxide sample: we see that the trends for the activities (dots) of ^{218}Po (plots **e** and **f**) and ^{214}Po (plots **c** and **d**) have all the same shape, and are in good agreement with the simulations (continuum lines). The simulations concern the time evolution of the contaminant activities once they are taken away from the main sources (^{222}Rn). In fact the ^{218}Po activity decreases with a proper decay constant ($T^{^{218}Po}$= 3.1 min) while the ^{214}Po activity after an initial increase falls off with a decay constant given by equation 3.23, which is in complete agreement with the result presented in Fig. 3.10.

If we look at plots **a** and **b**, which describe ^{210}Po activity, we see that the experimental data are not in agreement with the simulations, the reason for this behavior is due to the fact that the time needed for the lower part of the Rn chain to reach the secular equilibrium is quite long because of the long ^{210}Po half-life. The Polonium-210 is trying to reach the equilibrium but it needs about $4{\cdot}\tau_{^{210}Po}$ to get to it, in the mean while the activity is increasing linearly. These plots corresponds exactly to a zoom in on the origin of the Cartesian axes of Fig. 3.9b, it is a zoom in of an exponential function.

All the analyzed slabs have the same trend for the activity, but different values. The reason is probably linked to the chemical features of materials like copper and

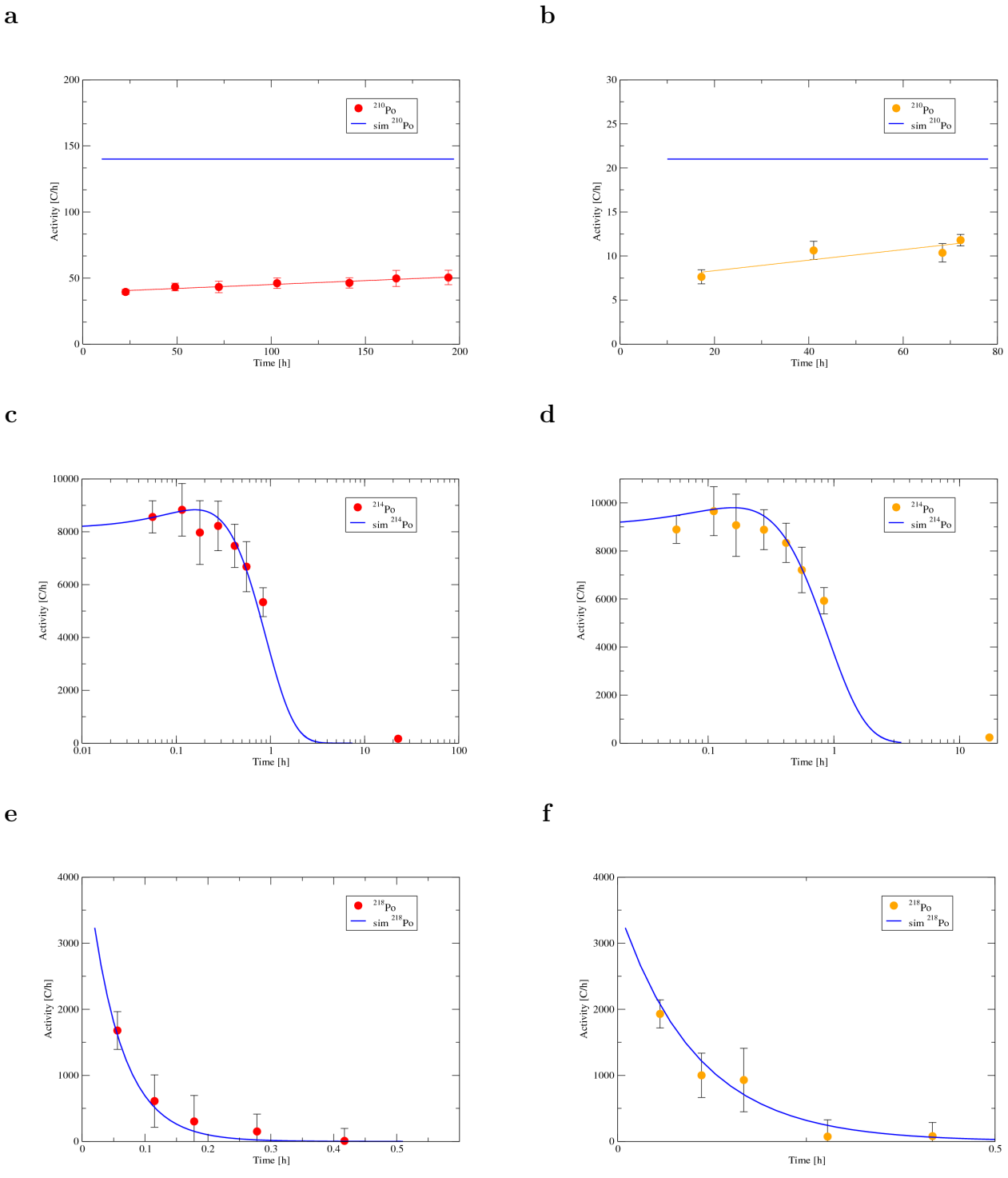

FIGURE 4.19: Activity for a copper and a tellurium sample. The dots represent the experimental data, while the continuum lines are the simulations of the time evolution of the activity of the contaminants.

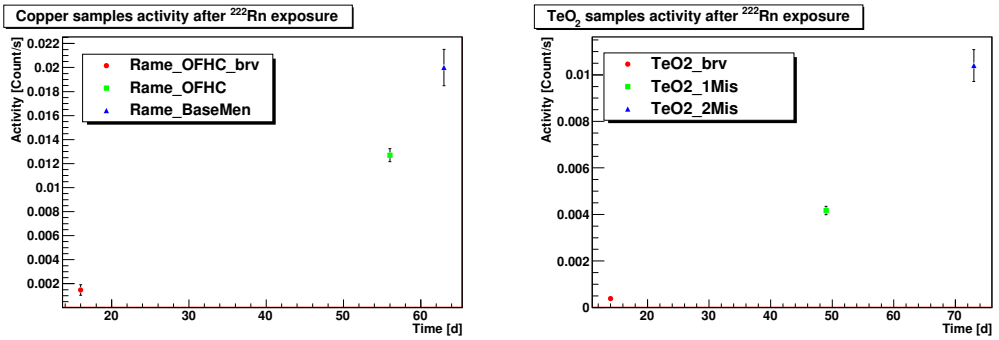

(a) (b)

FIGURE 4.20: Activity of (a) copper and (b) tellurium samples.

tellurium oxide: copper is more chemically active than tellurium oxide, in fact it has got more contaminants even if it was exposed for a shorter time, compare to the tellurium samples. There are also considerations regarding the grade of the surface. In principle a better grinded surface may present a *reduced* area, and in this way it can collect less contaminants. Moreover the peak shape is expected to be much sharper for well polished surfaces. Fig. 4.20 shows this behavior for the various samples. We just focused on the ^{210}Po activity. The choice of this isotope is due to the fact that the other two have a much shorter half-life, and during the set-up of the measurements it was needed some time to get the detector ready. During this period of time we were not able to analyze the contaminants on the samples which were decaying, so we were not able to calculate the instant in the time evolution of the activity (see Fig. 4.19) in which we were at the starting of the measurement. The Polonium-210 has a much longer half-life ($T_{1/2}$ = 138 days), and the "loss" in the activity evaluation is smaller compare to ^{218}Po ($T_{1/2}$ = 3.1 min) and ^{214}Po ($T_{1/2}$ = 0.164 msec).

If we take a look at the ^{210}Po activities of the different samples, we may observe that there is still a difference and this can not be caused by the material features, but it is due to the different time exposure. The more the sample is exposed to the high radon concentration atmosphere, the more it will be contaminated in ^{210}Po. The relation between exposure time and ^{210}Po activity seems to be slightly different from the linear regime, this bias is due to the fact that inside the Rn-box the secular equilibrium is still not reached, during the exposure time, and the ^{210}Po activity is increasing. So the samples that were exposed for longer time, evenly show a higher activity compare to the two other samples (Rame_OFHC_brv and TeO2_brv).

4.6.4 Radon and polonium diffusion

Radon is a gas thus it can diffuse in the air producing a Polonium contamination on material sufaces. This is a slow process and strictly linked to the Rn concentration in the atmosphere. Thus the more the slab is kept in the Rn-box the more the radon will diffuse into the material, obviously this is true if the sample surfaces are treated all in the same way. In fact the diffusion depends also on the effective surface of the sample. All the copper (and tellurium) samples were treated respectively in the same way (see [19]).
In order to understand how much the gas has diffused inside the samples, we have to observe an asymmetric part at lower energy for the polonii isotopes. We focus our attention on the element which has the longest half-life and allows us carrying out an analysis about the evolution in time of the activity: ^{210}Po. We try to reconstruct the Polonium-210 activity signal in the energy spectrum using Monte Carlo simulations. We suppose that the alpha peak at 5.3 MeV and its tail are caused by two different processes: a deposition and a diffusion of the contaminants. So, for each sample we simulated a superficial contamination layer of 0.5 nm (whose depth is much smaller than the Monte Carlo accuracy) and a contamination layer with an exponential profile inside the sample due to the diffusion of the gas at different depths. The solution of the diffusion equation of a radioactive isotope in a solid medium [81] is the reason for the choice of the exponential profile.
As already mentioned in the previous section in an acquired spectrum the tails of the various polonium isotopes may overlap. So, in order to get rid of this type of interferences in evaluating the diffusion profile we have taken into account just differential spectra. The spectra are chosen in a way that all the ^{218}Po and ^{214}Po have already completely decayed and the only left isotope is ^{210}Po. After about 15 hours the only signal was produced by Polonium-210, this long period of time is due to the presence of intermediate elements of the ^{222}Rn chain (^{214}Pb and ^{214}Bi) which have an half-life of about 30 min.

The diffusion profile are reconstructed with relative accuracy (see Fig. 4.21). In Table 4.3 are reported the diffusion depth for the various samples. We were not able to estimate this value for the two samples that were exposed for the shortest time (*Rame_OFHC_brv* and *TeO2_brv*) due to the lack of statistics. Looking at the contamination depths we can make two statements: the ^{210}Po diffusion is strictly related to the exposure time of the samples to Rn, and the tellurium samples have a deeper implantation depth of ^{210}Po. The first remark is clearly understandable, in fact the more the samples are kept in the Rn-box the longer is the time at

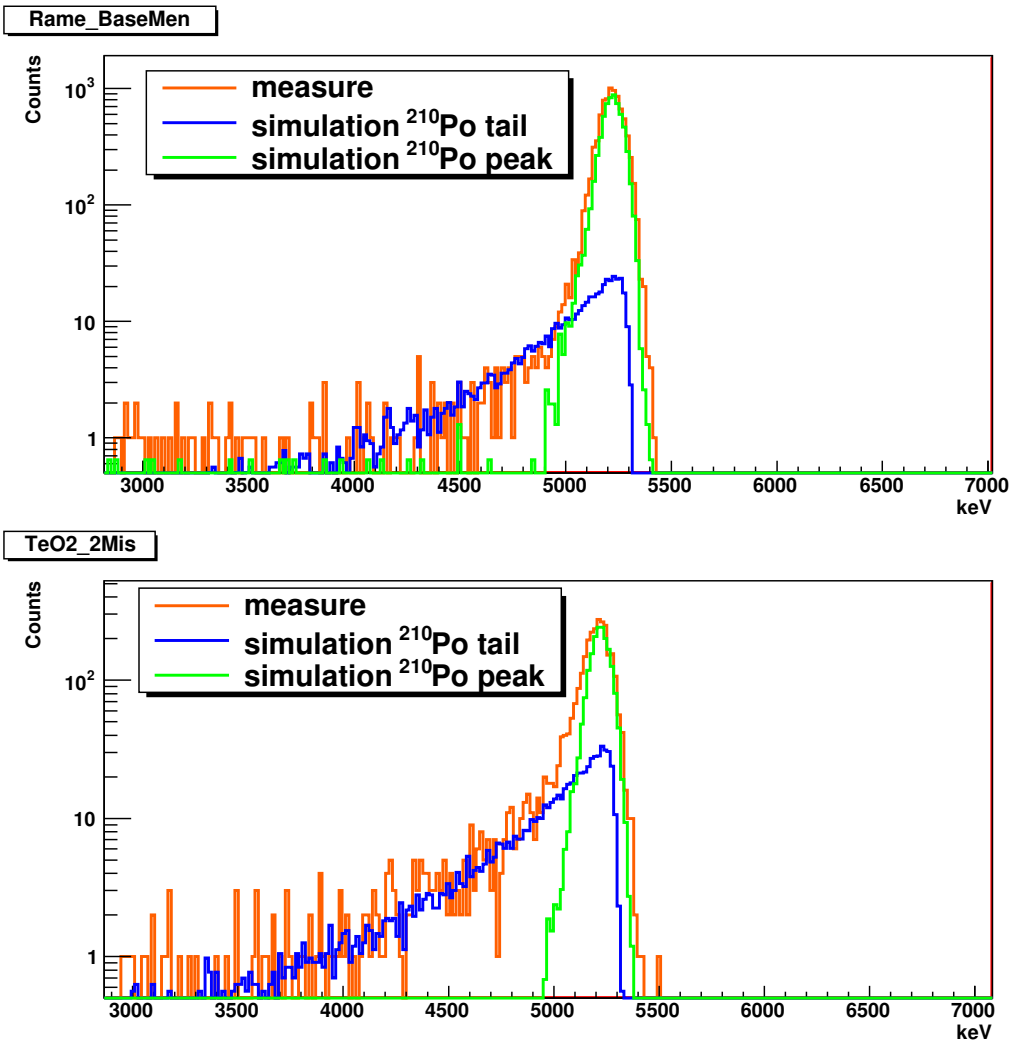

FIGURE 4.21: Reconstruction of the two components (peak and tail) ^{210}Po signal (top) for the copper sample (diffusion profile 430 nm) and (bottom) for the tellurium one (diffusion profile 940 nm).

^{210}Po's disposal for diffusing in the inside. Obviously the higher is the concentration of radon in the atmosphere the faster and deeper will be the diffusion, since it just depends on the concentration gradient between the environment and the free cavity (or canyons) on the sample surface, especially on the copper (see Fig. 4.22). At the same time we can state that the diffusion of Polonium-210 in the samples is not caused by the nuclear recoil implantation, in fact a recoil nucleus of 150 keV will travel in a copper matrix just 16 nm (Monte Carlo simulation). A cross-check that validates the previous statement is done by looking at the diffusion depth of ^{214}Po, which in the acquired spectra show a high statistics. The diffusion depth of this nuclide in the samples (respectively copper and tellurium) does not change with the time exposure to Rn but it has a fixed value (380±20 nm for copper and 520±20 nm for tellurium dioxide). The reason for this behaviour is the short

Sample	Material	Exposure time	Diffusion depth
Rame_BaseMen	Copper	63 days	430±20 nm
Rame_OFHC	Copper	56 days	410±20 nm
Rame_OFHC_brv	Copper	16 days	***
TeO2_2Mis	Tellurium Oxide	73 days	940±20 nm
TeO2_1Mis	Tellurium Oxide	49 days	500±20 nm
TeO2_brv	Tellurium Oxide	14 days	***
Teflon	PTFE	117 days	100±20 nm

TABLE 4.3: Diffusion length of ^{210}Po

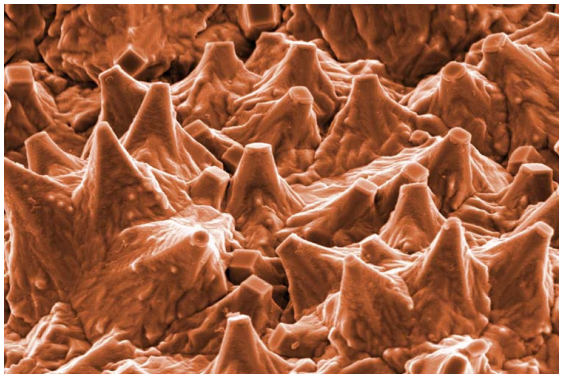

FIGURE 4.22: SEM image of a burnt electroplated copper deposit.

half-life of this isotope ($T_{1/2}$ = 0.164 msec) which is several orders of magnitude smaller compare to the exposure time of the samples.
Since ^{214}Po and ^{210}Po have compatible diffusion profiles they are driven by the same mechanism of diffusion. Moreover we can say that the nuclide that is causing the deep contamination (and that is diffusing in the samples) is the Polonium and not the Bismuth. In fact if Bismuth-210 diffuses in the sample then we would have a deeper diffusion profile for ^{210}Po compare to ^{214}Po, because while ^{214}Po is diffusing as a consequence we would have ^{210}Bi diffusion that would lead to a deeper contamination of ^{210}Po. This is not our case since the Polonium isotopes have same diffusion profiles. Bismuth does not diffuse in copper.
The tellurium samples have a deeper contamination compare to the copper one, even if they have smaller surface contamination (activity under the peak). The reason is in the crystal structure which is highly regular in the tellurium, allowing a diffusion with less impedances.

Some interesting remarks that can be made concern the region between 3 and 4 MeV where is clearly evident the presence of a continuum of counts. Considering that what we are looking at is a differential spectrum where the only signal visible is the ^{210}Po one, we can attribute this to the polonium diffusion inside the sample

(see Fig. 4.21). This continuum is not explained completely by the diffusion profile shown before, but through a different diffusion mechanism which goes deeper into the material. Moreover there are no counts in the upper part of the spectrum (higher than 5.5 MeV, α emission of ^{222}Rn); we see no alpha peak at any radon "fast" daughters (^{218}Po and ^{214}Po) region. This is a clear evidence that the radon is not diffusing in the samples, otherwise during the measurement time ($>T_{1/2}$ of Rn) we would still be able to see some events coming from the radon "fast" daughters. Therefore there must be some other element which is diffusing leading to a deep ^{210}Po implantation. The only nuclides which have a half-life long enough for allowing deep diffusion are ^{210}Pb and ^{210}Po.
It should be stressed that the Polonium contaminations on the samples, while it is in the Rn-box, are at the equilibrium this implies that the Polonii isotopes are the only elements that stick to the samples. In fact if Bismuth-218 or Lead-218 nuclei (elements of the Rn decay chain) would stick, then the equilibrium would be distorted because of their concentration which is higher than the Polonium-218/214 one (see next sections for better understanding). The consequence would be to have a Polonium-214 activity much higher than the Polonium-218 one, but we did not have evidence for this behaviour, the system was at the equilibrium.

4.6.5 Durative ^{210}Po diffusion

The question that concerns which nuclide is diffusing inside the samples is really important, because it allows understanding the precautions we have to take for preventing the recontamination of radiopure components of the detector.
We can test the hypothesis of the polonium diffusion reanalyzing the samples exposed to Rn to see if there were some kind of change in the contamination profile of ^{210}Po.
The copper and tellurium samples after the first measurement were kept inside polyethylene bags in a controlled environment, for preventing any additional uncontrolled recontamination. About 350 days after the first measurement the *Rame_OFHC*, *Rame_OFHC_brv*, *TeO2_1Mis* and *TeO2_2Mis* samples were reanalyzed in the same way, employing a surface barrier Silicon detector in a vacuum chamber.
We have remarked that the samples have a different contamination profile, compare to the one observed after the first measurement. The analysis is carried out in the same way as before, employing Monte Carlo simulations for evaluating the

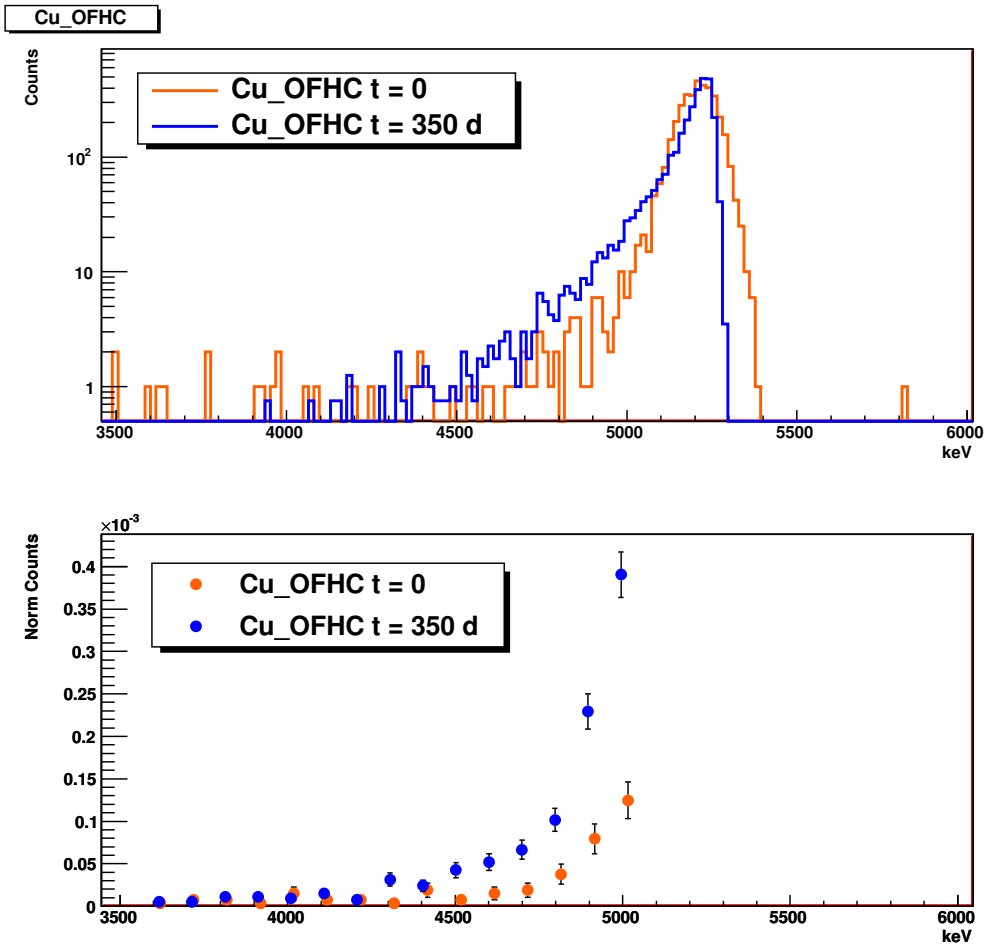

FIGURE 4.23: Comparison between the two measurement (the first one in orange and the second in blue) of the Cu_OFHC sample renormalized. The bottom plot is a renormalized comparison of the two tails. The renormalization factor takes into account: the detector resolution (since the two measurements were carried out with two different detectors, with different resolution) and the total integral of the signal (since the polonium activity has changed).

new diffusion depth. In Table 4.4 are presented the new depths: it is clear that the polonium has moved deeper inside the copper samples. In fact the renormalized tail of the (*old* and *new*) polonium signals are incompatible (see Fig. 4.23) in the region that lies 3 FWHM values away from the peak. We see no compelling evidence of diffusion inside the tellurium samples. The reason for the different behaviour of the two materials lie in the fact that the diffusion inside TeO_2 is rather a fast process due to the crystal structure, and the polonium gets into deeper during the Rn exposure. The amorphous copper, on the other side, has some impedances that slow down this process and it just takes more time for having a deeper contamination. This work shows for the first time that polonium diffuses duratively inside copper. This result can have important consequences in the physics of rare

Sample	Diffusion depth @ t=0	Diffusion depth @ t= 350 d
Rame_BaseMen	430±20 nm	***
Rame_OFHC	410±20 nm	550±20 nm
Rame_OFHC_brv	***	390±20 nm
TeO2_2Mis	940±20 nm	940±20 nm
TeO2_1Mis	500±20 nm	500±20 nm
TeO2_brv	***	***

TABLE 4.4: Diffusion length of ^{210}Po at different time.

Sample	First Measure [C/h]	Last Measure [C/h]
Rame_OFHC	33.30 ± 1.94	148.99 ± 1.97
Rame_OFHC_brv	4.63 ± 1.58	34.84 ± 0.93
TeO2_2Mis	26.23 ± 2.46	82.45 ± 1.55
TeO2_1Mis	11.80 ± 0.65	66.31 ± 1.84

TABLE 4.5: Polonium-210 peak activity right after the radon exposure and after 350 days.

events since it rises up an important problem concerning the control of implanted radioactive nuclides. In fact if we have an implanted polonium contamination on a detector component which is not a background source, it may turn into a source after a time period during which it changes its implantation depth.

In this analysis we have considered also the peak activity, and as already mentioned we expect that the ^{210}Po has increased as it is shown in Table 4.5. In fact the chain is trying to reach the equilibrium and the polonium activity tends to the Lead-210 one. Unfortunatly we are not able to test any dynamical model about the evolution of the ^{210}Po peak activity, since it is growing at the same time it is diffusing leading to an overlap of this two processes which are impossible to untangle due to the too big time difference between the two measurements. This does not allow a differential study.

4.6.6 ^{210}Pb study

Detector components following an exposure to an environment rich in Rn will be contaminated in Polonium-210. However, this nuclide is produced by the ^{210}Pb nuclei that are implanted or deposited on the sample. If we analyze more in detail the mechanism and dynamics that bring to a lead contamination we will be able to

reduce the polonium one. Moreover a precise evaluation of the Lead-210 content in the samples will allow a complete knowledge of the nuclides that have stuck on the surface, thus a meaningful value for the *Radon sticking factor*. This will be evaluated taking into account also the Radon progeny.
In a radioactive chain at the equilibrium the activity of all the elements of the chain is the same, this means that the concentration of a specific nuclide scales as its half-life:

$$A = \frac{N_1}{\tau_1} = \frac{N_2}{\tau_2} = \frac{N_3}{\tau_3} = ... \tag{4.6}$$

Since the ^{210}Pb is the longest living element of the chain ($T_{1/2}$ = 22.3 y), it will have the highest concentration inside the Rn-box, once the equilibrium is reached. We can define two main mechanisms that lead to this type of contamination: implantation and gravimetric deposition. The first one is simply the formation of a chemical bound between a Lead-210 nuclide and an element of the matrix (in our case copper or tellurium); the second one is gravimetric deposition of particulate and radon combinations [80].
In order to determine which of the two processes is the leading one, a specific measurement was carried out. A contaminated copper sample (*Rame_BaseMen*) was measured after an exposure to Rn. We have chosen a copper sample, because of its high reactivity (higher than tellurium, see Fig. 4.20) to Rn and Rn daughters. The Polonium-210 contamination of the mentioned sample was analyzed right after the exposure and after that a cleaning procedure was applied. The cleaning consisted in a series of baths of ultrapure water, absolute ethanol and again ultrapure water:

1. sample exposure;
2. sample measurement: $A_{^{210}Po}$ = 118.8±3.2 counts·h^{-1};
3. sample cleaning: ultrapure water ⇒ absolute ethanol ⇒ ultrapure water;
4. sample measurement: $A_{^{210}Po}$ = 100.5±2.9 counts·h^{-1}.

The time passed between the two measurements was about 24 hours, this means that we can easily neglect any possible contribution coming from the dynamic evolution of the polonium activity, due to the equilibrium transient state. We see that the sample activity has changed of about 15%, which we can estimate to be the contribution of the gravimetric deposition of ^{210}Pb to the overall lead activity, the remaining one can be attributed to the other mechanism.

Now that we have understand how ^{210}Pb sticks to the copper, we might focus

on the mechanism leading to the production of this nuclide in the Rn-box where the equilibrium among the various elements of the radioactive chain is still not reached. As already stated ^{210}Pb is the element with the highest concentration inside our box, thus the associated nuclides can stick to the sample letting the ^{210}Po contamination be visible during the first measurement. So, the initial ^{210}Po contamination is produced directly by the ^{210}Pb already available inside the box, and because of that we might define this action as a *fast* one. We can evaluate this ^{210}Pb quantity on the sample looking at the initial ^{210}Po activity that we suppose caused just by the *fast* ^{210}Pb implantation.
In parallel to this we can describe an other way of undirectly producing ^{210}Pb but this time directly on our sample (and not in the Rn environment). As shown in Fig. 4.17 ^{214}Po diffuses inside the copper, this means that at a certain time, after the complete decay of ^{218}Po and ^{214}Po, there will be a ^{210}Pb deep contamination. We may define this way of producing ^{210}Pb as a *delayed* one, compare to the *fast* one. We can compute the *delayed* lead quantity looking at the dynamics of the polonium activity while it is trying to reach the secular equilibrium in the chain. At that point calculating the ^{210}Po activity, we will look at just the ^{210}Pb produced by the decay of the fast radon daughters that are implanted on the sample, neglecting the ^{210}Pb fast produced quantity that we assume completely decayed.
The ^{210}Po activity defined as a function of the ^{210}Pb activity at equilibrium. If we analyse the *Rame_OFHC* sample after 350 days, assuming the equilibrium between Polonium-210 and Lead-210, we get the following equation:

$$A_{Po} = A_{Pb}^{0\,delayed}\frac{\lambda_{Pb}}{\lambda_{Po}-\lambda_{Pb}}(e^{-\lambda_{Pb}t} - e^{-\lambda_{Po}t}) \;=\; 148.99\,\text{counts}\cdot\text{h}^{-1}. \tag{4.7}$$

where we can obtain the value of the $A_{Pb}^{0\,delayed}$.
Since $T_{Pb} = 22.3$ years $\gg T_{Po} = 138.4$ days, the previous equation becomes:

$$A_{Po} \approx A_{Pb}^{0}(1 - e^{-\lambda_{Po}t}). \tag{4.8}$$

Now we will evaluate the fast composition, that will be derived from the first measurement after the exposure. This measurement lasted 3.7 days, which is a small value compare to the polonium half-life. Under these conditions we can make the following approximation:

$$A_{Po} \approx A_{Pb}^{0\,fast} \cdot \lambda_{Po} \cdot t \;=\; 33.30\,\text{counts}\cdot\text{h}^{-1}. \tag{4.9}$$

and thus we derive A_{Pb}^{0fast}.
The ratio between the activity of Lead-210: rapidly produced and the one produced later is:

$$\frac{\text{delayed A}_{^{210}Pb}}{\text{fast A}_{^{210}Pb}} = \sim 6. \tag{4.10}$$

This result tells us that the ^{210}Pb contamination comes mainly (85%) from the fast radon daughter contamination, and not from the ^{210}Pb direct exposure of the sample. This also gives the clean room requirements needed for a rare events experiment: strict control on the radon (and radon daughters) emanation, while the ^{210}Pb deposition can be considered as a secondary issue.

4.6.7 Radon sticking factor

Let's assume to have a surface (S) exposed to a high radon concentration atmosphere (n, radon nuclei concentration). To compute the number of radon nuclei which hit our surface per time unit and surface unit (e.g. the flux), Γ, we have to consider the number of nuclei in the volume $v \cdot t$, where v is the particle velocity and t the time unit. If we integrate the solid angle in which all the particles in the volume $v \cdot t$ see the surface S, we obtain:

$$\Gamma \left[\frac{hits}{cm^2 \cdot sec}\right] = \int_0^{2\pi} d\phi \int_0^{\frac{\pi}{2}} d\theta sin\theta \int_0^{v} drr^2 \left(\frac{Scos\theta}{4\pi r^2}\right) \frac{n}{S} = \frac{n \cdot v}{4}. \tag{4.11}$$

The thermodynamics let us write the velocity of the nuclei as:

$$v = \sqrt{\frac{k_b T}{m}} \tag{4.12}$$

where k_b is the Boltzmann's constant, m the mass of the nucleus and T the temperature (300 K). In our case, where the radon concentration is 315 kBq$\cdot$ m^{-3} we have:

$$\Gamma = 5.85 \cdot 10^9 \frac{hits}{cm^2 sec} \tag{4.13}$$

Once we have the total number of nuclei which have a probability different from zero to hit on (hence to stick) the slab, the computation is almost done. In order to estimate the number of nuclei which does stick on slab we use the activity definition:

$$A = \lambda \cdot N \tag{4.14}$$

Sample	Material	Exposure time	Σ_{Rn}
Rame_BaseMen	Copper	63 days	$1.86 \cdot 10^{-9} \pm 1.01 \cdot 10^{-10}$
Rame_OFHC	Copper	56 days	$6.99 \cdot 10^{-10} \pm 1.82 \cdot 10^{-11}$
Rame_OFHC_brv	Copper	16 days	$5.16 \cdot 10^{-10} \pm 2.78 \cdot 10^{-11}$
TeO2_2Mis	Tellurium Oxide	73 days	$3.75 \cdot 10^{-10} \pm 1.19 \cdot 10^{-11}$
TeO2_1Mis	Tellurium Oxide	49 days	$3.13 \cdot 10^{-9} \pm 2.10 \cdot 10^{-11}$
TeO2_brv	Tellurium Oxide	14 days	– –

TABLE 4.6: Radon sticking factor value for different materials

where A is the *delayed* ^{210}Pb activity derived from the equation 4.7, λ is the decay constant of the elements with activity A (hence ^{210}Pb) and N is the number of nuclei. The Radon sticking factor is computed on the *delayed* Lead-210 activity, because this element will integrate all the other elements that have stuck on the sample by means of its long half-life. All the nuclides that are implanted will decay and reached the Lead-210 level.
Finally the sticking factor is computed employing the following formula:

$$\Sigma_{Rn} = \frac{A^0_{^{210}Pb} \cdot \tau_{^{210}Pb}}{\Gamma \cdot S \cdot t_{exp}} \tag{4.15}$$

where S is the slab surface and t_{exp} the time exposure. These values are conservative because we are assuming that the Lead-210 concentration is constant with time.

After a thorough analysis we can state that the radon sticking factor of the studied materials has a tiny value for a very high radon concentration (much higher than the environmental one). The sticking factor of the samples which had a smaller time exposure will tend to the value of the ones which were exposed for longer time, because the radioactive system is trying to reach the equilibrium configuration between Lead-210 and Polonium-210.
The copper samples being more chemically reactive show a higher radon sticking factor compare to the tellurium dioxide ones.
The sticking factor for the *Rame_BaseMen* sample has a larger error value compare to the other copper samples because its delayed ^{210}Pb activity was measured after 52 days, and not after 350 as the other samples. This has affected the measurement, giving a poorer statistics.

4.6.8 Radon-induced surface contaminations in CUORE

From the previous studies we have understood that the main source of contamination for the CUORE sensitive materials (copper and tellurium) is the Radon exposure. To be more specific the Polonium is the only element that diffuses directly in copper and in tellurium, we have demonstrated that Radon and Bismuth do not diffuse. The Polonium diffusion leads to a ^{210}Pb contamination, so the mechanism that produces the Lead-210 contimanation is strictly linked to the Polonium contamination.

In the environment in which the detector will be assembled the Radon concentration in air must be reduced as much as possible in order to prevent the Polonium nuclei sticking on the detector components.

Given the knowledge about the radon sticking factor, we can now evaluate the background contribution in the region of interest that an exposure to Rn of the copper for the CUORE detector will have on the background of the experiment.

We suppose that during the storage time and the assembly line of the detector, we expose the copper to an atmosphere with a Rn concentration of 100 mBq·m^{-3} (expected concentration inside the clean room see section § 4.5.3) for a period of time of one year. Considering the Rn sticking factor for the copper being in the best case (closer to the saturation level): $1.86{\cdot}10^{-9}$ (see Table 4.6) for a radon concentration of 315 kBq·m^{-3}, and assuming the linearity dependence of Σ_{Rn} with the Rn concentration, we can scale this value for the one inside the storage area (or clean room). We will have after the exposure an initial ^{210}Pb activity of $1.07{\cdot}10^{-7}$ Bq·cm^{-2}. After 5 years of data taking there will be a ^{210}Po surface contamination of $1.07{\cdot}10^{-7}$ Bq·cm^{-2} on the copper (we assume that the ^{210}Pb and the ^{210}Po are at the equilibrium). The entire CUORE copper surface is 41061 cm^2 and the detector efficiency of a Polonium-210 layer at the depth of 0.5 μm will give a contribution to the background in the region of interest of CUORE of $3.36{\cdot}10^{-3}$ counts·keV^{-1}·kg^{-1}·y^{-1}. Thus the value obtained from the computation tells us that an exposure of CUORE copper to radon (with the assumption of one year at 100 mBq·m^{-3}) would not give a significant contribution to the background of CUORE knowing that the estimated background of CUORE has to be less than 0.01 counts·keV^{-1}·kg^{-1}·y^{-1}. But still, the radon concentration in the area in which the detector will be assembled must be under control because an exposure to 1 Bq·m^{-3} of radon might create some problems.

Chapter 5

EDELWEISS surface contaminations

The EDELWEISS (Expérience pour DEtecter Les Wimps en SIte Souterrain) collaboration consists of about 50 scientists from universities and research centers in France, Germany, Russia and England. The experiment is installed since 1994 at the Laboratoire Souterrain de Modane (LSM), an underground laboratory settled in the highway tunnel of Fréjus between France and Italy. The EDELWEISS experiment looks for direct interaction of dark matter particles in Germanium crystals. The first 320 g Germanium detector has been installed in the EDELWEISS cryostat in 2000 [69]. In 2001, the EDELWEISS-I phase started with 3 detectors [101]. The experiment has been upgraded step by step in terms of shieldings and detection mass. With a complete new set-up since the end of 2005, the so-called EDELWEISS-II experiment [102] intends to have a mass of about 30 kg.

5.1 EDELWEISS detectors

The goal of the EDELWEISS-II experiment is to detect the nuclear recoil events of the well-motivated dark matter candidate, the Weakly Interacting Massive Particle. The event rate of the WIMP can be as low as 10^{-3} counts$\cdot$kg$^{-1}\cdot$d^{-1}, which is a low rate expecially because these are low energy events. The recoil energy of a WIMP in a detector is also very low. A WIMP with a mass M = 100 GeV$\cdot$c^{-2} has a kinetic energy of $E_k \approx 50$ keV. An elastic collision between a 100 GeV$\cdot$c^{-2}

galactic WIMP and a nucleus, for example, then gives the nucleus to recoil with typical energy of ≈ 25 keV. A very low event rate plus a low recoil energy require special precautions in terms of background, which has then to be maintained as low as possible.

The EDELWEISS experiment is located underground in the LSM laboratory which provides an approximately 4800 m.w.e. rock shielding against cosmic ray muons.

A requirement for the experiment is to have passive and active shieldings around the detectors. Then when the background is hardwarely maintained as low as possible, the next step is to find various methods to clearly distinguish the WIMP from other signals in the bolometers.

The possible signatures used in the EDELWEISS-II experiment to discriminate the recoil spectrum of the WIMPs from those of background particles are:

- Type of interaction: WIMPs scatter off the nuclei of the detector material (nuclear recoil), while background particles, mainly β and γ through Compton scattering, scatter off the electrons of the target (electronic recoil).
- Location in the detector: the WIMPs have a long free mean path, which means that the events due to the WIMPs are uniformily spread in the detector. On the other hand, events from the environmental radioactivity of the laboratory happen close to the surface: high energy γ have a mean free path less than a cm, and low energy γ, β and α much smaller.
- Multiple interaction: neutrons produce nuclear recoils, like WIMPs. But the WIMPs as it is described by its name interact weakly, which is not likely to make multiple interactions, while the neutrons-nucleus scattering cross section is $\sigma_n \approx 1$ b with a distance in between two interactions in a solid of the order of a centimeter.

Therefore, WIMP events are classified as single non-surface nuclear recoil events. When a WIMP interacts with a nucleus of the target, the kinetic energy of the recoil nucleus is partially converted into three possible ways: ionization, heat/phonons and scintillation light. The measurable quantities are then an electric current, a temperature rise and a light emission. The Ge bolometers of the EDELWEISS experiment, which do not scintillate, measure the signal in the ionization and heat channels.

Choosing two channels of detection allows discriminating between WIMPs and background events. The mean free path of an electron of 50 keV in a solid is a few μm while a nucleus of the same energy recoils only a few tens of nm. A nuclear recoil produces then proportionally less ionization than an electronic recoil of equal energy in the same medium. This effect is quantified in a factor, the so-called quenching factor Q, which is the ratio of the signal of a nuclear recoil over that of an electronic recoil of equal energy, as described empirically in [103]. In the ionization channel for Germanium, the quenching factor is $Q_{Ge} \simeq 0.33$ [104]. It is important, however, to note that there is no quenching in the heat channel: $Q'_{Ge} \simeq 1$ [104], which means that the heat signal does not depend on the origin of the interacting particle. This is the great advantage of the cryogenic Ge bolometer, the energy scale comes from heat and this is indepedent of the particles. The second great advantage is that the quenching in the ionization channel allows an event-by-event discrimination of electronic and nuclear recoils by the simultaneous measurement of the two signals.

Because of the different quenching factors Q_{Ge}, the energy calibration using the ionization channel depends on the origin of the signal, whether electronic or nuclear. The detectors are calibrated with gamma and neutrons sources, in keV-electron-equivalent, keV$_{ee}$. One keV$_{ee}$ corresponds to 1 keV for an energy deposit of a γ or a β.

The EDELWEISS collaboration uses cryogenic Germanium crystals. The high-purity Germanium detectors, as shown in Fig. 5.1 have a mass of 320 g and a cylindrical shape. The diameter is 70 mm and the height is 20 mm. On the sides of some detectors, the thickness reduces to 4 mm due to beveled edges in a 45° angle. The detectors of EDELWEISS detect simultaneously two signals for each interacting particle, the ionization signal and the heat signal.

5.1.1 Ionization channel

The bolometer are semi-conductor crystals made of ultra-pure Germanium. The Germanium has a lot of advantages. First, it is possible to have crystals of an extremely intrinsic purity of $N_{\text{acceptor}} < 10^{-10}$ and of a relatively high mass (kg). Furthermore the small gap between the conduction band and the valence band, 0.75 eV$_{ee}$ at 0 K [105], allows a great conversion efficiency of electronic energy into electron-hole pairs. The intrinsic fluctuation of the Germanium due to free

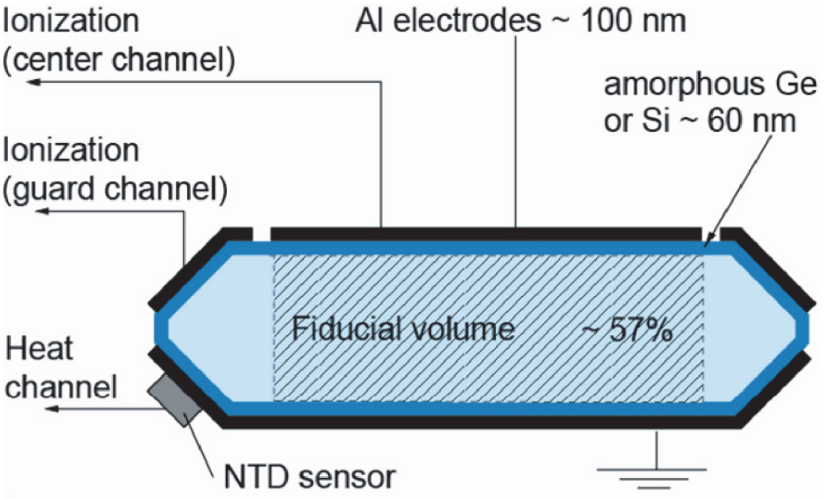

FIGURE 5.1: Schematic overview of an EDELWEISS Germanium detector with double read-out (heat and ionization).

charges, fluctuation which depends on T, is low, $\approx$ 100 eV_{ee} for a deposit of 10 keV_{ee}, and therefore detection thresholds of the order of a few keV_{ee} are possible.

In Fig. 5.1, we represent a Germanium detector as used in EDELWEISS-I and the first phase of EDELWEISS-II. On top and on bottom of the bolometers there are planar electrodes to collect charges. The electrodes are made of 100 nm thick Aluminum layers sputtered on the upper and bottom surface of the detectors. The top electrode is divided into a central part, and a guard ring, electrically decoupled for radial localisation of the charge collection. Between the electrodes a moderate voltage between $\pm$3 V and $\pm$8 V is applied. The charge carriers created in the crystal by the particle interaction drift along the electrical field lines towards the electrodes where they are collected. The time interval between the interaction and the collection of charges depends on the location of the interaction relative to the electrodes [106].

The complete charge collection is essential to determine the type of interaction, whether electronic or nuclear recoil. However, incomplete charge collection can occur because of three main processes:

- Presence of impurities: during their migration towards the electrodes, charge carrier can be trapped by impurities and induce the formation of space charges. To limit this effect, degradation or regeneration phases are conducted with ^{60}Co, which emits two high energy γ. A regeneration lasts at least one hour between two data acquisitions, and occurs at minimum every 24 hours [107].

- Surface events: as already mentioned, electrons and α particles (with kinetic energies of several tens of keV) have a mean free path of only respectively few μm and few nm. Therefore the interaction of these particles takes place in principle very close to the surface of the crystals [108]. It is possible that the created charge carriers are collected by the inadequate electrode due to the proximity of the interaction to the electrodes. For these near-surface events, the measured ionization signal may represent for example only an half of the actual energy of the charge carriers. In [109] it is shown that introducing an additional amorphous layer between the electrodes and the crystal significantly reduces the collection of wrong-sign charges. An amorphous dead layer of either Germanium or Silicon is used for EDELWEISS detectors and has a thickness of about 60 nm.

- Electric field line irregularities: on the lateral sides, the electric field lines can escape from the solid before they reach the electrodes. Therefore the lateral sides of the surface are beveled and a segmented electrode (center and guard ring electrodes) is used to additionally acquire information on the position of the interaction. The beveled surfaces allow having a more homogeneous field under the central electrode. Miscollection due to field inhomogeneties are on the guard ring and can be rejected afterwards. Moreover, the guard ring collects the radioactive background from the holders of the detectors and of the electronics, which are intentionally localized in this region.

To limit these effects, the electric field is maintained at a few V/cm. In the data analysis a fiducial volume is defined where: the electric field is the most uniform, a reliable charge collection is expected and the detector is better shielded from its environment.

When an interaction occurs, depending on the type of recoil induced in the target, the number of electron-holes created per unit of energy is different:

$$N_I = \frac{E_r}{\epsilon} \tag{5.1}$$

where E_r is the initial energy deposit of the particle and the needed energy to create a charge carrier is $\epsilon \simeq 3$ eV for an electronic recoil, and $\epsilon \simeq 9$ eV for a nuclear recoil. For an equal energy deposit, a nuclear recoil will create 3 times less pairs than an electronic recoil. This difference is represented by the quenching

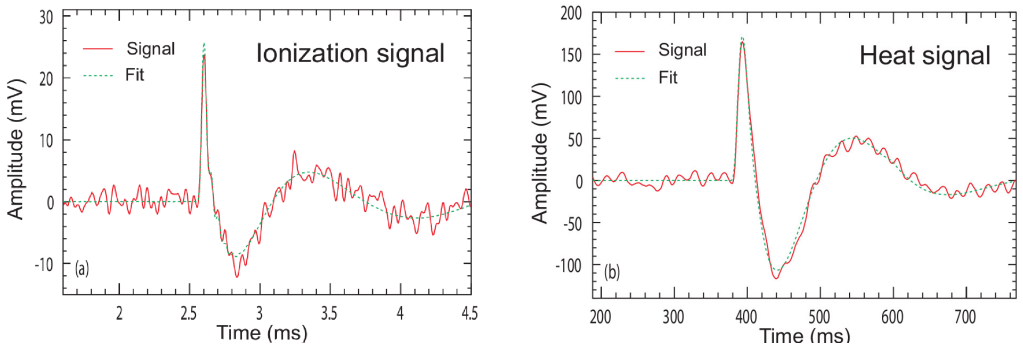

FIGURE 5.2: Example of filtered signals for (a) the ionization and for (b) the heat channel. The green line is the corresponding fit.

factor $Q = \epsilon_\gamma/\epsilon_n$. We define then two numbers for the pair creation N_I^γ and N_I^n:

$$N_I^\gamma = \frac{E_r}{\epsilon_\gamma} \tag{5.2}$$

$$N_I^n = \frac{E_r}{\epsilon_n} = Q\,\frac{E_r}{\epsilon_\gamma} \tag{5.3}$$

The ionization signal is measured in mV after the amplification in a charge amplifier, see Fig. 5.2. It is then normalized thanks to calibration runs to be expressed in keV. Conventionally, for electronic recoils, we consider E_r=E_I, where E_I is the ionization energy in keV$_{ee}$. Practically, the ionization signal is measured and then transformed in ionization energy thanks to an ionization normalization factor. This factor is determined during calibration runs with a well-known gamma source, ^{133}Ba. This calibration procedure allow expressing the ionization energy for any incident particle $E_I \equiv \epsilon_\gamma N_I$. Hence the ionization energy for an electronic recoil E_I^γ and a nuclear recoil E_I^n are:

$$E_I^\gamma = \epsilon_\gamma\,\frac{E_r}{\epsilon_\gamma} \tag{5.4}$$

$$E_I^n = \epsilon_\gamma\,Q\,\frac{E_r}{\epsilon_\gamma} = Q\,E_r \tag{5.5}$$

with E_I=E_r for γ particles for the normalization.

5.1.2 Heat channel

The heat increase δQ is linked to the temperature variation ΔT through the equation $\delta Q = C\Delta$T, where C is the heat capacity of a body. The phonon is a particle

describing the excitation of a vibrational mode in a crystal. These excitations, once thermalized, carry the heat δQ. Immediately after the collision, the phonons are not thermalized, δQ and ΔT are then not defined. The fastest thermic sensors can then be sensitive to athermal phonons, out of equilibrium; we then would talk about *phonon signal*. The slowest sensors are sensitive just to thermalized phonons; we then would talk about *heat signal*.

The principle of the measurement of the heat induced by the interaction of a particle is to measure the energy deposit of the particle in the target, which is entirely converted into phonons. A bolometer is made of two elements: an absorber in which the particles interact and deposit energy (where also the ionization energy is generated) and a thermal resistor (or thermistor) which measures the induced rise of temperature (see Fig. 5.3). The relation between the deposited energy and the rise of temperature is:

$$\Delta T = \frac{\Delta E}{C(T)} \tag{5.6}$$

where C is the total heat capacity of the bolometer. The heat capacity of the absorber at very low temperature follows Debye's law (see equation 3.4). For Germanium, the Debye temperature is approximately 360 K. Consequently, to lower the heat capacity and to achieve a measurable temperature rise for very small energy deposits, the crystals need to be operated at very low temperatures. In the EDELWEISS experiment, the base temperature is 10-20 mK. For example, for a Germanium bolometer of 300 g at a temperature of 20 mK, the interaction of a particle that releases 10 keV gives a temperature rise of about 10 μK.

These detectors allow reaching a very low detection threshold ($\sim$ 1 keV) and an energy resolution of $\sim$ 100 eV. One technical challenge, however, is to reach detector masses of the order of 1 kg and to maintain C as low as possible due to the need of very low temperature. The thermistors of the EDELWEISS standard bolometers are Neutron Transmutation Doped (NTD) Germanium crystals glued on a sputtered gold pad on the main Germanium crystal (see Fig. 5.3). These NTD sensors are sensitive to the global temperature variations of the absorber, having no resolution power on the time evolution of the phonon signal and thus without the possibility to determine the position of the interaction, in contrast to the sensors for athermic phonons (they will be discussed in the next section).

Increasing the applied voltage, and thus the electrical field, would in principle improve charge collection for ionization but, a moderate voltage, typically between $\pm$3 V and $\pm$9 V depending on the detector, is essential to limit additional heating

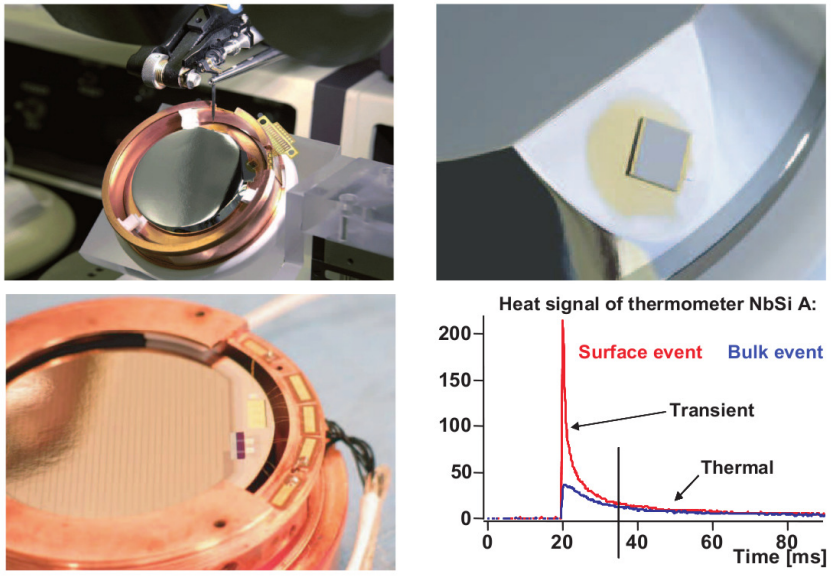

FIGURE 5.3: EDELWEISS Germanium bolometers: (first row) picture of a standard Germanium bolometer within the copper holder structure and the NTD thermistor glued. (second row) Picture of a Germanium detector with NbSi thin film sensor, for detecting athermal phonons.

of the crystal. This effect is generally known as Neganov-Luke effect [110, 111]. It is analog to the Joule effect in metals. The charge carriers increase their kinetic energy during their drift in the crystal and release this energy via phonons. The released energy is proportional to the number of charge and to the applied voltage of polarisation:

$$E_{Luke} = N_I V = V \frac{E_r}{\epsilon}. \tag{5.7}$$

The total measured energy E_{tot} is then equal to the sum of E_{Luke} and the recoil energy E_r, reduced by a potential heat quenching factor Q' in the case of a nuclear recoil:

$$E^{\gamma}_{tot} = E_r + V \frac{E_r}{\epsilon_\gamma} = E_r \left(1 + \frac{V}{\epsilon_\gamma}\right) \tag{5.8}$$

$$E^{n}_{tot} = Q' E_r + V \frac{E_r}{\epsilon_n} = E_r \left(Q' + \frac{QV}{\epsilon_\gamma}\right). \tag{5.9}$$

For any incident particle, the normalized heat energy in keV is:

$$E_H = \frac{E_{tot}}{1 + V/\epsilon_\gamma}. \tag{5.10}$$

Hence the heat energy for an electronic recoil E_H^γ and for a nuclear recoil E_H^n is:

$$E_H^\gamma = E_r \frac{1 + V/\epsilon_\gamma}{1 + V/\epsilon_\gamma} = E_r \tag{5.11}$$

$$E_H^n = E_r \frac{Q' + Q'V/\epsilon_\gamma}{1 + V/\epsilon_\gamma}. \tag{5.12}$$

And note that E_H=E_r still holds for γ particles.

5.1.2.1 Germanium NbSi bolometer

In order to achieve the 10^{-8} pb goal for the spin-independent WIMP-nucleon scattering cross section, the EDELWEISS experiment needs to accumulate an exposure of 1000 kg·d with no events in the nuclear recoil band (obviously except for WIMP ones). Therefore, the contribution of background within the nuclear recoil band has to be less than 0.001 counts·kg^{-1}·d^{-1} in the region of interest. However, if the contribution from neutrons is considerably low, by means of vetos, the low energy β coming from ^{210}Pb may generate low ionization signal, which means most likely surface events with a miscollected charge. A standard Germanium bolometer without any device to reject surface events will get $\approx$ 2000 events during 1000 kg·d of exposure (assuming a reasonable value of 2 counts·kg^{-1}·d^{-1}). Hence, bolometers which can localize precisely the position of events in the detectors for rejecting the undesired ones have been developed.

The first new generation of detectors, called Germanium NbSi bolometers, are operated combining the two sensors for charge collection and temperature rise into one. Two heat channels and two ionization channels are measured simultaneously. This is achieved by an amorphous thin film, typically 10-100 nm thickn, replacing the NTD-thermometer and the Aluminum electrodes on both sides of the Germanium crystal [112, 113]. These films are obtained by evaporating NbSi, on the surface of the crystals, whose electric resistance is strongly dependent on the temperature.

The advantage of these thin film phonon detectors is the possibility to determine the position of the interaction by comparing the signal ratio of each side of the crystal, which was not possible with the NTD sensors. A particle interaction in the Germanium crystal will produce out-of-equilibrium phonons diffusing away from the impact site. In the case of near-surface events, a large amount of these high-energy phonons will be trapped by the nearby NbSi layer and induce

an athermal heat signal. This signal, as illustrated in red in the lower part of Fig. 5.3, will be much larger than the one created by a bulk event of the same energy, illustrated in blue, while the thermal part related to the total energy deposit does not change. Using pulse shape analysis of the two NbSi thermometers allows effective identification of near-surface events, but still bad charge collection events can not be flagged.

However the results of the test phase at the LSM laboratory were not as successful as expected, and this detector development is not pursued any more.

5.1.2.2 Interdigitized bolometer

In addition to the new NbSi athermal phonon detectors, the collaboration developed for the EDELWEISS-phase II a new method of surface event rejection based on the ionization signal. The first prototype of this new InterDigitized bolometer (ID), called ID201, has been realized at CSNSM (Orsay, France) in the context of the R&D program of EDELWEISS. ID201 is a Germanium crystal of a mass of about 200 g, 48 mm-length diameter and 2 cm-height with a new electrode design. The classical disk-shaped central Aluminum electrode is replaced by interleaved concentric rings with typical width of 200 μm, 2 mm spaced, centered around a central disk of 1 mm diameter. The strips are alternately connected by ultrasound bonding to make two alternated subsets. Both faces are identical. As for standard bolometers, guard electrodes and a NTD complete the device. So there is a total of 6 different electrodes (2 strips on the top and 2 on the bottom, 2 guards) which can be independently polarized and read the ionization channel. One additional electrode is used for the heat channel.

Different voltages of polarization are applied on the electrodes to modulate the electric field inside the detector. Symmetrically for each surface, there is one collecting electrode and one veto. One face collects electrons and the veto the holes, the other one collects the holes and the veto the electrons. The two guard electrodes are separated into one collecting electrode on top, and one veto on the bottom. Charge carriers produced by a particle interaction are drifted along the field lines towards the collecting electrodes. Depending on the place of the energy deposition, different event populations are then obtained in the electrodes. In principle it is possible to identify four different classes of events [114]:

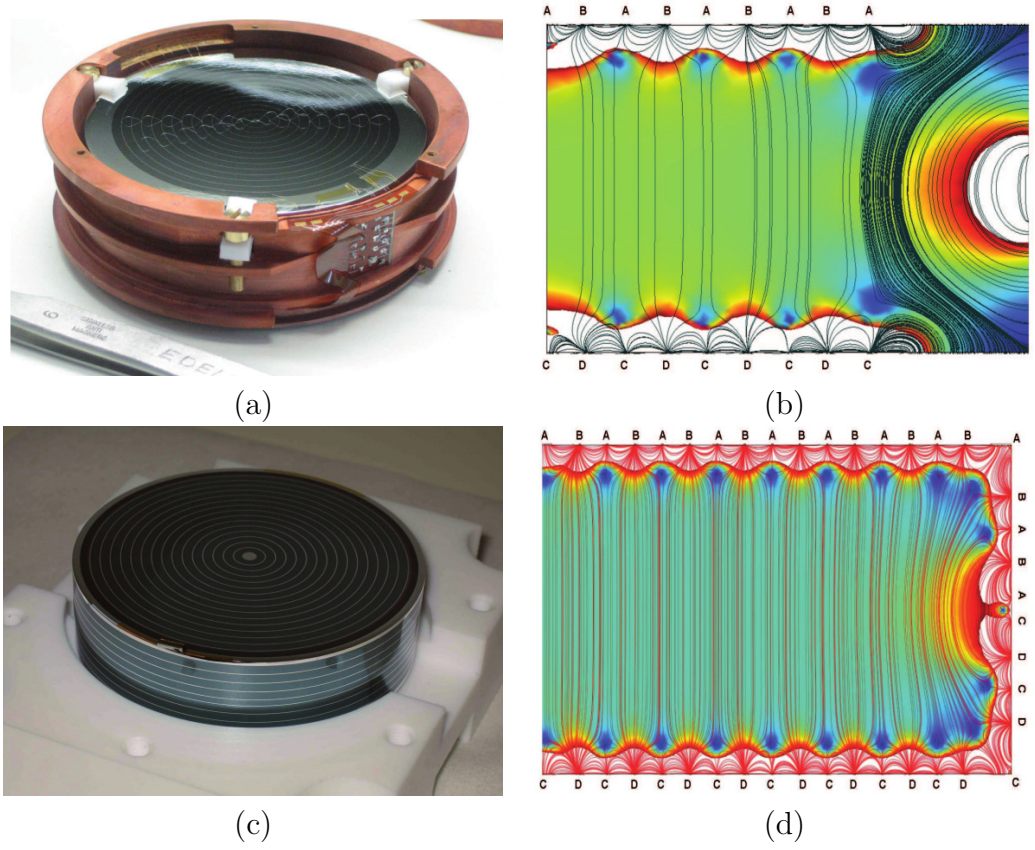

FIGURE 5.4: EDELWEISS-II detectors: (a) Germanium InterDigitised detector ID and (b) relative simulated electric field. (c) Germanium Full InterDigitised detector FID and (d) relative simulated electric field.

- Bulk events create signals on both sides of the crystal: electrons (holes) on the collecting electrode of one (the other) side.
- Near-surface events deliver signals only on one side: electrons on the collecting electrode of a side, holes on the veto electrodes of the same side.
- Low field area events, which occur at the limit of the bulk and surface events, result in charge division between three measurement channels because of Coulomb s law: electrons and holes are collected as for bulk events, but additionally holes or electrons are also collected in the corresponding veto electrodes of a side.
- Lateral events which occur in the guard area are collected in the specific electrodes of the guard.

It is thus possible to select potential signal events, for which there is no collection of charge on the veto electrodes and in the guards. A fiducial volume can then also be defined, in which there is no event with a miscollected charge. Apart from

this technique, this bolometer type, as well as other ID with larger masses have the same read-out principle as other standard Germanium crystals, except that the number of electrodes allow having a good rejection of surface events.

With the Germanium NbSi bolometers, 2% of the β background still produced a signal in the nuclear recoil band due to bad charge collections, which means that we had a power rejection of 98%. With interdigitized bolometer, the obtained passive rejection is 99.998% [13], less than one β over 2000 events makes an event in the nucelar recoil band. And the threshold has been improved from 30 keV for standard bolometer to 10 keV [115].

If, in terms of surface passive rejection, the interdigitised bolometers are the best tuned detectors so far in EDELWEISS-II, the fiducial volume of an ID is less than 60% of the available volume. The interdigitized bolometer have therefore been developed a step further. New bolometers, so called Full InterDigitized bolometer (FID), have their interleaved concentric strips continuing on the side which is not beveled any more, as shown in Fig. 5.4c. The new detector generation, FID, allows to have a more uniform electric field inside the detector, and at the same time to increase the fiducial volume up to 80%.

The interdigitized bolometer type has been installed in 2008 for test purposes in EDELWEISS-II. At that time there were three ID bolometers. But since mid-2009 (Run 12), ten 400 g ID detectors were used, the rest is two FID prototypes and two standard Germanium bolometers.

5.1.3 Event discrimination

From the interaction of a particle in the detector medium to the collection of the created charges into the different channels, the ionization and the heat energies, E_I and E_H, of the incident particle are defined and known. Based on the experimental values E_I and E_H, we deduce how the recoil energy and the quenching factor of events can be extracted and use these information to discriminate between electronic and nuclear recoils.

Recoil energy E_r and quenching factor Q

The ionization and heat energies after the calibration and the normalization can be expressed as:

$$E_I = QE_r \tag{5.13}$$

$$E_H = E_r \frac{Q' + Q'V/\epsilon_\gamma}{1 + V/\epsilon_\gamma}. \tag{5.14}$$

The recoil energy E_r is the value to be determined for the WIMP search. But the previous equations do not allow determining E_r without any hypothesis on the ionization quenching factor Q and on the heat quenching factor Q'.

As we already mentioned, in Germanium, Q' is expected to be 1. However, since the determination of the energy calibration for nuclear recoils, and then the energy threshold of the detector, rely on the value of Q', thorough investigations have been performed [104]. The heat quenching factor is indirectly measured combining direct measurements of Q and measurements of the ratio Q/Q' by neutron calibrations. For recoil energies between 20< E_r <100 keV, the result for the heat quenching factor is:

$$Q' = 0.91 \pm 0.03 \pm 0.04 \simeq 1, \tag{5.15}$$

where the two errors are the contribution from the Q and Q/Q' measurements. Starting from here, we will consider $Q' = 1$. The ionization quenching factor Q depends on the recoil energy. For Germanium, we use the Lindhard model [103]:

$$Q = \frac{k\, g(\epsilon)}{1 + k\, g(\epsilon)}, \tag{5.16}$$

with $\epsilon = 11.5{\cdot}E/Z^{7/3} = 0.00354{\cdot}E$ keV, $k = 0.133{\cdot}Z^{2/3}/A^{1/2} = 0.157$, and g = $3{\cdot}\epsilon^{0.15}+0.7{\cdot}\epsilon^{0.6}+\epsilon$. Merging all these values, we obtain the following quenching factor:

$$Q = 0.16\,(E_r)^{0.18}. \tag{5.17}$$

This relation has been tested with direct measurements and holds at a 10% level [104].

As $Q' \approx 1$, it is possible to determine a pair (E_r,Q) for each event from the

ionization and the heat energy:

$$E_r = \left(1 + \frac{V}{\epsilon_\gamma}\right) E_H - \frac{V}{\epsilon_\gamma} E_I \tag{5.18}$$

$$Q = \frac{E_I}{E_r}. \tag{5.19}$$

In case of miscollection of charges, the collected charges for a surface events correspond to only a fraction of the value of what they should be. The quenching factor becomes $Q = Q_m < 1$, typically $0.3 \leq Q_m \leq 0.8$, while the recoil energy remains the same.

$$E_I^m = Q_m E_r \tag{5.20}$$

$$E_H^m = E_r \frac{Q' + Q_m V/\epsilon_\gamma}{1 + V/\epsilon_\gamma}, \tag{5.21}$$

then plugging these equations in equation 5.18, we have $E_r^m = E_r$. Surface events are thus translated into the (E_r, Q) plane with $Q < 1$, getting closer to the nuclear recoil region, but with correct reconstruction of the recoil energy E_r.

Resolutions

Knowing the recoil energy E_r and the corresponding quenching factor Q, it is possible to make the so-called Q-plot. This plot represents the quenching factor as a function of the recoil energy for all the event detected by the detectors.

For each channel two values of the resolutions are measured, one for the baseline during physics runs and one for the photoelectric peak of ^{133}Ba. This isotope emits a characteristic γ of 356 keV. This is enough penetrating to reach the detectors inside the cryostat. The resolution, squared sum of the baseline resolution and Barium peak resolution, vary together with the energy such as:

$$\sigma_{I,H} = \sqrt{\sigma_{I,H}^2(0) + a_{I,H}^2 E_{I,H}^2}, \tag{5.22}$$

where $a_{I,H}$ is a factor calculated from the resolution at 356 keV and at 0 keV:

$$a_{I,H} = \frac{\sqrt{\sigma_{I,H}^2(356) - \sigma_{I,H}^2(0)}}{356}, \tag{5.23}$$

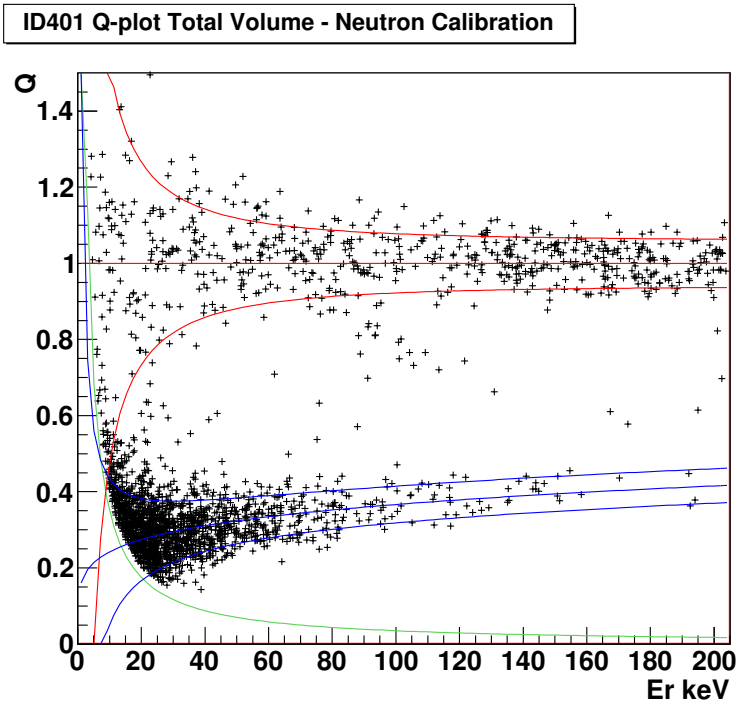

FIGURE 5.5: Q-plot for a partial of a calibration run with a neutron source. The red and blue lines represent the 90% acceptance for respectively electronic and nuclear recoil regions.

$\sigma_I(356)$ is computed from the Gaussian fit in the ionization channel of the Barium peak. $\sigma_H(356)$ is deduced from the distribution of E_H/E_I once $\sigma_I(356)$ is measured.

Now we can determine electron and nuclear recoil zones using the measured resolutions. We can parametrize the region of 90% acceptance for nuclear and electronic recoils (see Fig. 5.5) by the following cut:

$$|Q - \langle Q_{\gamma,n}\rangle| \leq 1.645\,\sigma_{\gamma,n}, \tag{5.24}$$

where $\langle Q_{\gamma,n}\rangle$ and $\sigma_{\gamma,n}$ are the average value and standard deviation of the Q distribution for nuclear (n) and electronic recoils (γ). Both variables are determined for each detector. In addition, for electronic recoil populations we define a region of 99.99% acceptance ($|Q - \langle Q_{\gamma,n}\rangle| \leq 3.29\,\sigma_\gamma$). This region is used for rejecting electronic recoils, even if the Q_γ is not Gaussian distributed.

By construction, the ratio of the ionization energy to the recoil energy, Q, is equal to 1 for energy deposits coming from γ. For neutrons, Q, is a function of E_r:

$$\langle Q_n\rangle = \alpha\,(E_r)^\beta, \tag{5.25}$$

from the dispersion of these data is deduced the nuclear recoil band, defined as the region in the (E_r,Q) plane where 90% of nuclear recoils are expected. The widths of electronic and nuclear recoil bands are given in units of standard deviations of electronic and nuclear distributions. They can be calculated starting from the definition of Q and E_r, obtaining the following set of equations:

$$\sigma_{Q_\gamma} = \frac{1 + V/3}{E_r}\sqrt{\sigma_I^2 + \sigma_H^2} \tag{5.26}$$

$$\sigma_{Q_n} = \frac{1}{E_r}\sqrt{\left[\left(1+\frac{V}{3}\right)\langle Q_n\rangle\sigma_H\right]^2 + \left[\left(1+\frac{V}{3}\langle Q_n\rangle\right)\sigma_I\right]^2}. \tag{5.27}$$

A previous investigation [116] has measured a broader nuclear recoil distribution than the one expected from the previous equation at high energy for neutron calibration data. So the width σ_{Q_n} of Eq. 5.26 has to be smeared by an additional spread, as follows:

$$\sigma'_{Q_n}(E_r) = \sqrt{\sigma^2_{Q_n}(E_r) + +C^2E_r^2}, \tag{5.28}$$

the constant C represents the effect of multiple neutron scattering and energy straggling of the Ge recoils. The experimental value of C is 0.035.

5.1.4 Data acquisition

For each detector, the data acquisition (DAQ) has to generate from 3 up to 7 channels per bolometer: heat, ionization from the center electrodes and ionization from the guard electrode in the case of a standard Germanium bolometer; ionization from the collecting electrode of a side, ionization from the veto electrode of the same side, the same for the other side and the guard and finally the heat, in the case of an interdigitized bolometer.

Basically when one channel of one detector triggers, all the other channels of all detectors are registered and read out as one event. The ionization signal is saved in a time window of 50 ms, the heat signal over 1 s. Besides the physics signal, the baseline before the event is also registered, which is called the pre-trigger. The main action is to choose between an ionization or a heat trigger.

The risetime of the ionization signals is ∼1000 times faster than the one for the heat signals. The advantage is that the time of an event can be known very accurately, and the search for the heat signal is then facilitated. However, the data acquisition has a heat trigger because of the following reasons:

- the baseline resolutions of the heat channel are typically twice as good as those of the ionization channel;
- the ionization signal of a nuclear recoil event in Germanium is 3 times smaller than the one of an electronic recoil for the same energy deposit, while the heat signals have the same amplitude. Therefore the trigger is more efficient for the small amounts of energy deposit and does not inherently depend on the type of interaction.

The main problem of the heat trigger is the search of the corresponding ionization signal which occurs before the heat signal because of its very fast risetime. This problem has been worked out in [117]. The conclusion is that the maximum time interval between an ionization and a heat signal is 20 ms. Thus, as soon as a heat signal passes the threshold, the system looks back up to 40 ms in the ionization signal buffer for the corresponding signals. This is made by comparing the data with a reference event built during the calibration runs. Once the event with the highest amplitude is found, all other events are synchronized to this one and saved on disk.

5.2 EDELWEISS-II cryostat and shielding

In the WIMPs hunting, the principal limitation is the background, especially from neutron-like events. To be shielded against most of the cosmic rays, the EDELWEISS experiment is sheltered under 4800 m.w.e. of shielding rock. Still there is natural radioactivity in the rock and in the material around bolometers, that need further reduction strategies.

5.2.0.1 Reversed cryostat

The EDELWEISS-II cryostat has a total volume of about 100 l and can host up to 120 bolometers with a total mass of approximately 30 kg. It is a nitrogen-free system, using three pulse tubes to cool the 100 K and 20 K copper screens around the detectors and a He reliquefier to reduce the He consumption. Its operating temperature of 10 mK is reached by the principle of a dilution refrigerator.

The characteristic of this cryostat is that it has an inverted geometry, with the

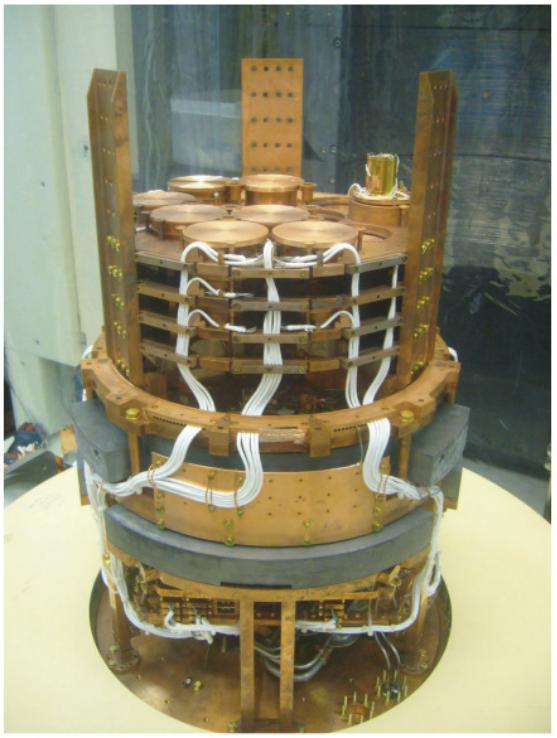

FIGURE 5.6: Picture of the EDELWEISS reversed cryostat.

experimental chamber on the top of the structure (see Fig. 5.6). It simplifies the installation and maintenance of the detectors as well as reduces the susceptibility to vibrations by the pumping system. Furthermore, since the complete cryogenic pumping system with all supply tubes is below the bolometers, the shielding of the detectors is more uniform. The copper walls of the cryostat are the so-called self-shielding. Nevertheless, inside the cryostat, in addition to the radiopurity selection of materials, the bolometers have individual copper casings, plus some archaeological lead underneath to protect against noise and radioactivity from the electronics nearby the crystals.

5.2.0.2 Shieldings

Then from inside to outside, 20 cm of lead and 50 cm of polyethylene are used. Since all materials in the close vicinity of the detectors are subject to radiopurity limitations, the innermost 3 cm of the total 36 tons of lead comes from archaeological sources (see Fig. 5.7). The archaeological lead used for EDELWEISS was retrieved from a sunken old roman ship [118]. The contamination in ^{238}U in this lead is less than 12 mBq·kg^{-1}.

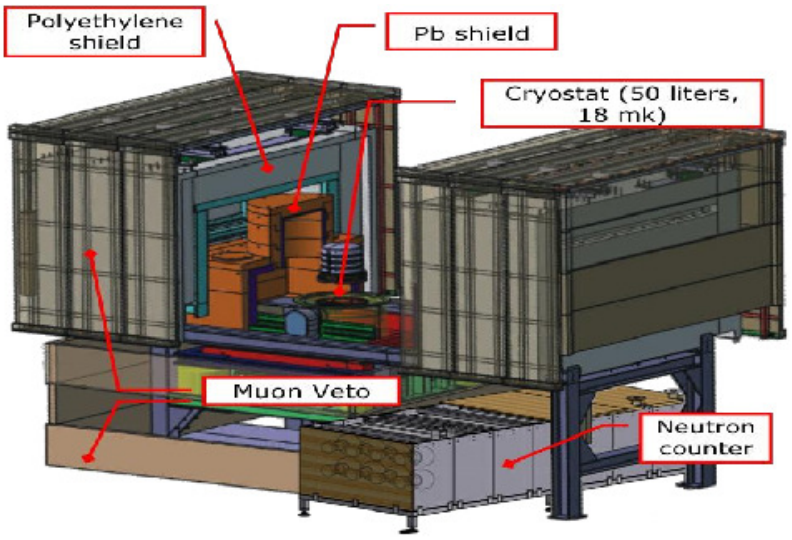

FIGURE 5.7: Schematic view of the EDELWEISS set-up system.

Polyethylene is an hydrogen-rich moderator, which moderates and absorbs neutrons from natural radioactivity in the rock surrounding the underground laboratory. The mean neutron energy of these processes is of a few MeV. Then after the moderator material, most of the neutrons have an energy which is not sufficient to penetrate the lead shielding. The whole polyethylene shield is covered by a 98%-efficient plastic scintillator muon veto system.
For neutrons with a kinetic energy less than 10 MeV, the use of 50 cm of polyethylene allows to reduce the rate of neutrons by a factor of ∼1000 [119]. To allow easy access to the cryostat for installation and maintenance purposes, the experimental setup of EDELWEISS-II is separated into two horizontal levels. The lower part at ground floor houses most of the cryogenic system. The upper part, first floor, is placed in a permanent cleanroom of class 10,000. Furthermore the clean room is "deradonised". The radon concentration in the LSM laboratory is about 10 Bq·m^{-3}, but in the clean room the air contains less than 0.01 Bq·m^{-3}.

5.2.1 Neutron counters

The EDELWEISS-II collaboration performed a wide variety of neutron measurements in the proximity of the experimental set-up together with Monte Carlo studies.

Environmental neutron counter

Monitoring of the ambient neutron flux in proximity of the EDELWEISS experimental set-up is performed with four low background ^{3}He gas detectors. Each proportional counter is filled with 400 kPa of ^{3}He and 500 kPa of ^{36}Ar as a working gas. In proportional counters the main background arises from the α contaminations in the walls of the detector. To reduce this background, a 50-60 μm thick layer of Teflon followed by a 1 μm layer of electrolytic copper are inserted between the wall and the gas volume.

The thermal neutron monitoring system has been installed in the LSM in November 2008. The detector was positioned a few meters away from the EDELWEISS-II setup. The close proximity to the wall provides a solid angle of 2π for the emerging thermal neutrons from the rock. The thermal neutrons coming from the other 2π are likely coming from materials inside the laboratory, especially from the anti-neutron massive polyethylene shielding of the EDELWEISS-II setup. The neutron detector makes possible a continuous day by day monitoring of the thermal neutron flux in the vicinity of the EDELWEISS-II experiment. This measurement yields to a flux of about $2{\cdot}10^{-6}$ $n{\cdot}\mathrm{cm}^{-2}{\cdot}\mathrm{d}^{-1}$.

Muon-induced neutron counter

A second neutron detector has been developed. So far the rate of muon-induced neutrons was evaluated with muon veto-bolometer coincidences. Despite its high efficiency, it is possible that some muons pass through the muon veto without being tagged as muon-like events, and induce neutrons, which can reach the bolometers. Furthermore, the total mass of bolometers is of few kg, the coincidence rate with the muon veto is very low and it dependes on the position of the bolometers inside the cryostat. Therefore, a dedicated detector was designed to access to the global rate of muon-induced neutrons.

The neutron counter registers two quantities: the events from thermalized neutrons in coincidence with the through going muons, and the multiple neutron events from muon-induced particle showers. The dedicated detector is based on a liquid scintillator of about 1 m^3 volume loaded with 2 g$\cdot$l^{-1} Gadolinium which is used as a core of the detector. This is a 1 t compact detector, with an expected count rate of 1 muon-induced neutron per day.

5.3 EDELWEISS-II results

The studied phase of the EDELWEISS-II experiment consisted of [13] ten hyper-pure Germanium crystals of cylindrical shapes with a diameter of 70 mm and a height of 20 mm. Five of these detectors have their edges beveled at an angle of 45 degrees and have a mass of 360 g. The mass of the other five detectors is 410 g. The detectors are in individual copper casings, stacked in towers of two to three ID detectors. During the entire data-taking periods, a dilution refrigerator maintains the detectors at a stabilized temperature of 18 mK.

After an initial cool-down of the cryostat in March 2009, the bulk of the data presented here was recorded over the following period of six months from April to September. An additional data set was recorded with two detectors during an initial run performed between July and November 2008.

In the first six-month running period, the data acquisition was running 80% of the time. Half of the losses are accounted for by regular maintenance operations and the other half by unscheduled stops. The fraction of running time devoted to detector calibration with γ and neutron sources is 6%. Among the 70 read-out channels, only five were defective or too noisy for use: four guards and one veto. Extensive calibrations performed in 2008 have shown that a signal on one of the guards is almost invariably accompanied by another one on either the other guard or a veto electrode, or by an imbalance in the charge collected on the fiducial electrodes. Relying on this redundancy is sufficient to attain high rejection factors even in the absence of a guard channel. Three detectors with one deficient guard signal are thus kept for the WIMP search. One detector had one deficient guard and one deficient veto electrode. In the absence of evidence that this particular combination of two missing channels can be efficiently compensated by the existing redundancies, it was decided a priori not to use this detector for WIMP searches. Thus only nine detectors were used.

The data were analyzed offline by two independent analysis chains. For each event, the amplitudes of the signals from the NTD-Ge thermistors and the six electrode signals were determined taking advantage of the synchronous digitization of all channels, and using optimal filters adapted to their time-dependent individual noise spectra.

The energy calibration of the ionization signal was performed with ^{133}Ba γ

sources. No gain variations were observed over the entire period, for a given polarization setting. The gain of the heat signal depends on the cryogenic conditions. It is measured as a function of time by monitoring the ratio of the heat and ionization signal for bulk γ events. The non-linearity of the heat gain as a function of energy is measured using γ calibrations. The baseline resolution on the different heat channels varies between 0.6 and 2 keV FWHM, with an average of 1.2 keV. The ionization baseline resolution for fiducial events varies between 0.8-1.2 keV FWHM, with an average of 0.9 keV.
The response of the ID detectors to nuclear recoils induced by neutron scattering was checked using an AmBe source.
In the six-month run, after all cuts, the nine ID detectors have a total exposure of 876.7 detector-days. The 2008 data with two of these nine ID detectors provides an additional exposure of 122.3 detector-days. With the average fiducial mass of 160 g, this corresponds to a total of 160 kg·d. Finally, taking into account the 90% C.L. region for nuclear recoils, this data set is equivalent to 144 kg·d.

Fig. 5.8 shows the distribution of Q as a function of recoil energy for the entire exposure. The average rate outside the nuclear recoil band in the 20-100 keV range is 0.16 counts·keV^{-1}·kg^{-1}·d^{-1}.
One event is observed in the nuclear recoil band at 21.1 keV.
The upper limits on the WIMP-nucleon spin-independent cross-section are calculated using the prescriptions of [32], and the optimal interval method [120] (see Fig. 5.9). A cross-section of $1.0{\cdot}10^{-7}$ pb is excluded at 90% C.L. for a WIMP mass of 80 GeV·c^{-2}. The EDELWEISS-II experiment ended up in July 2010. In these last months it has acquired a longer statistics with a twice bigger exposure (322 kg·d). The new presented limit (see Fig. 5.10) is $5.0{\cdot}10^{-8}$ pb is excluded at 90% C.L. for a WIMP mass of 80 GeV·c^{-2} [6].

5.4 ^{210}Pb source on ID detector

5.4.1 β rejection

In order to study the performances of the ID detector, the EDELWEISS collaboration setted up a system for testing the rejection power of β surface events. A ^{210}Pb source was created exposing a piece of copper to a high radon concentration. The goal was to obtain a copper matrix containing low energy β emitters. Lead-210

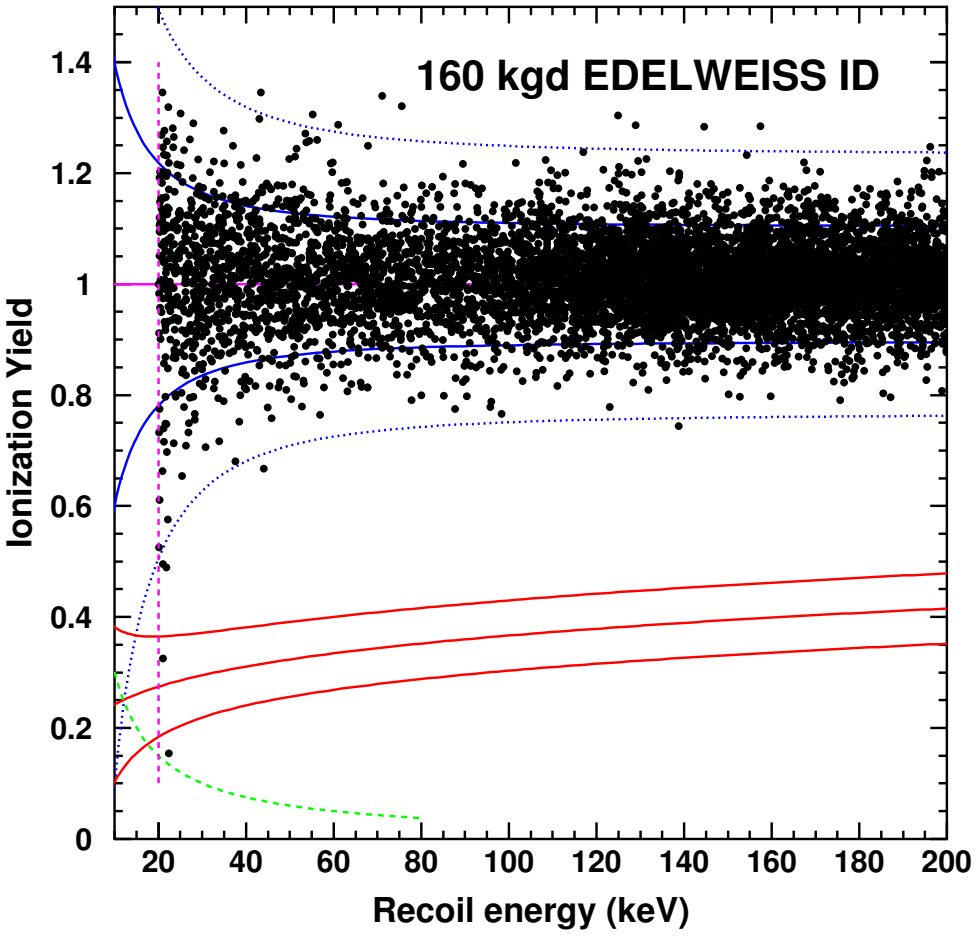

FIGURE 5.8: Ionization yield as a function of recoil energy of fiducial events recorded by EDELWEISS-II during an exposure of 160 kg·d. The WIMP search region is defined by recoil energies greater than 20 keV (vertical dashed line). The 90% acceptance nuclear and electron recoil bands (full blue and red lines, respectively) are calculated using the average detector resolutions. Also shown as dashed lines are the 99.98% acceptance band for the gamma (blue) and the 3 keV ionization threshold (green).

besides having a long half-life, compare to the other element of the radon chain, it is a tricky background source for DM experiment since in decaying it emits two β of 16.6 keV and 63.1 keV, together with a characteristic γ at 46.5 keV. These β have a penetration length in standard Germanium of a few μm, therefore if they are not flagged as surface events they might be consider as particles that: create a low heat signal (since they are low energy beta) and have a small quenching factor if the ionization signal is not completely collected (this is highly probable since they are events close to the surface where the field lines are not uniform), hence

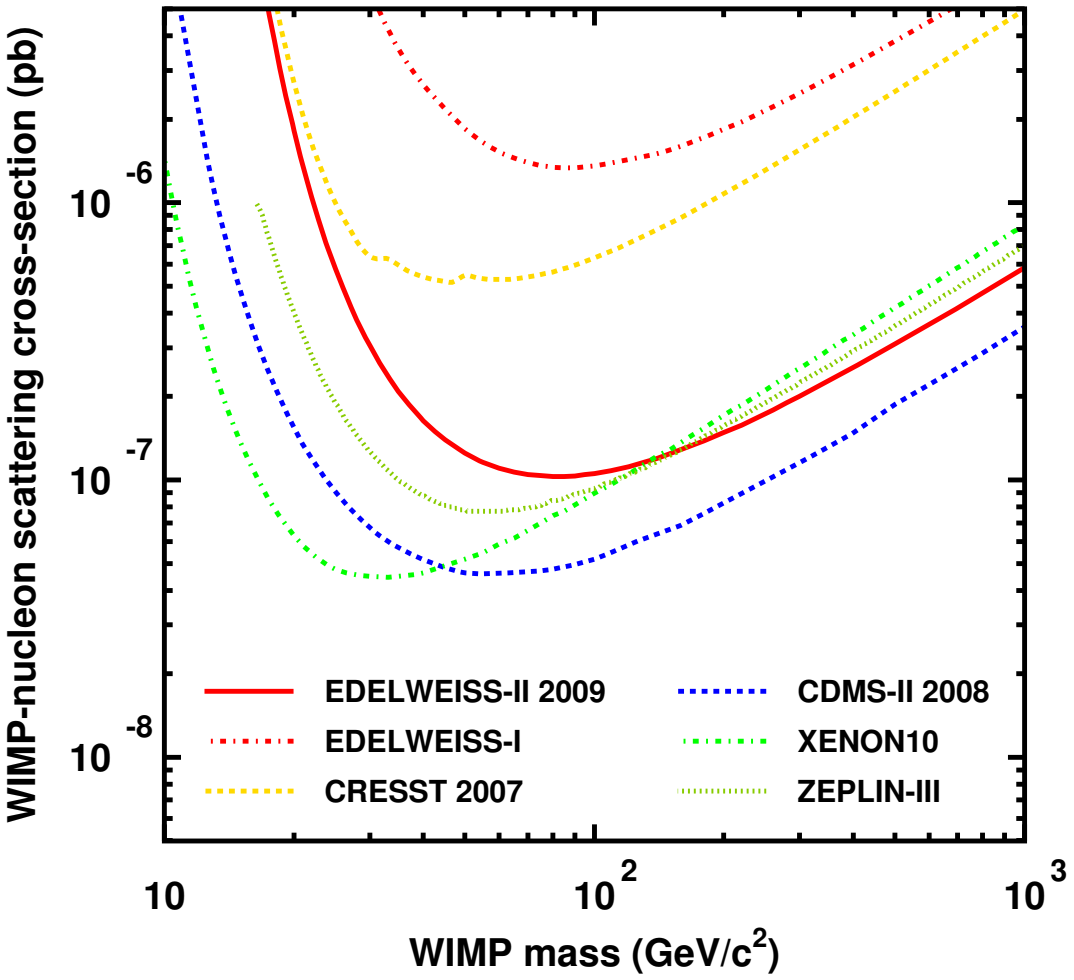

FIGURE 5.9: Limits on the cross-section for spin-independent scattering of WIMPs on nucleons as a function of WIMP mass, derived from the data presented in this letter, together with limits from other direct WIMP searches. The limits for CDMS, ZEPLIN, EDELWEISS-I, CRESST and XENON are from [7–11], respectively.

they can look like WIMP signals. This is one of the main reason for the development of ID detectors, bolometers able to discriminate surface events exploiting the shape of the electric field lines in the region close to the surface (see Fig. 5.4) After the exposure the copper sample was treated with a heat source and nitric acid in order to wash out any residual contaminant that was not well implanted on the matrix, since the ^{210}Pb source had to be installed in the cryostat facing an ID detector and we wished to prevent any possible contaminant migration from the matrix to the bolometer.

The detector chosen for performing the power rejection measurement of the ID

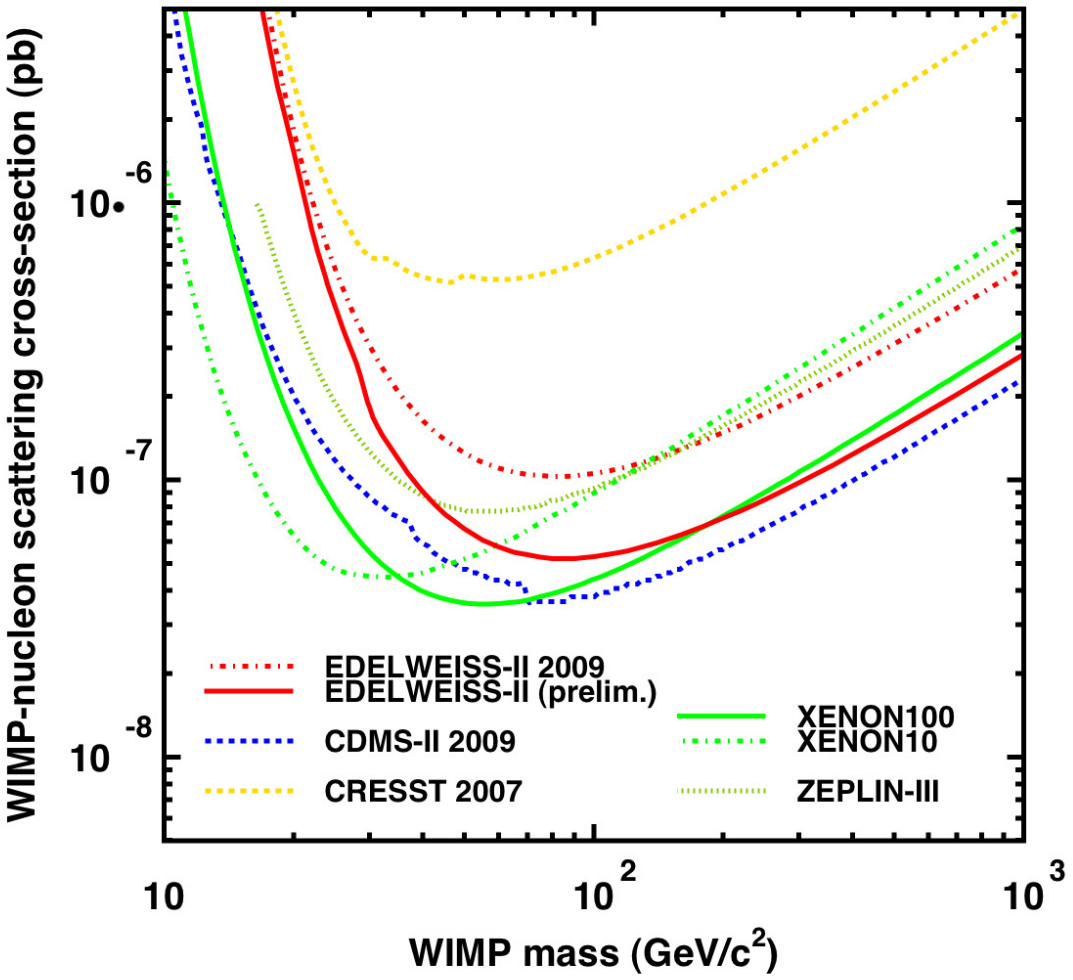

FIGURE 5.10: Preliminary new limits on the cross-section for spin-independent scattering of WIMPs on nucleons as a function of WIMP mass, presented by the EDELWEISS-II collaboration [6]. The new limits for CDMS, ZEPLIN, EDELWEISS-II, CRESST and XENON10-100 are also presented [8, 10–14].

detector generation was the ID201 (see Fig. 5.11). This detector has a mass of about 200 g, it is equiped with 10 electrodes on the top (and on the bottom), and the source was placed exactly in front of the detector. Looking at the top of Fig. 5.12 that represents the source events in the total volume of the detector on a Q-plot, we can make some statements regarding the Lead-210 source:

- there are three main populations in the plot:
  - αs in the high energy region with a Q value ranging from 0.2 to 0.5. In theory the expected Q value for these particle is 1, but since during the interaction in the detector they create a high density charged cloud, in

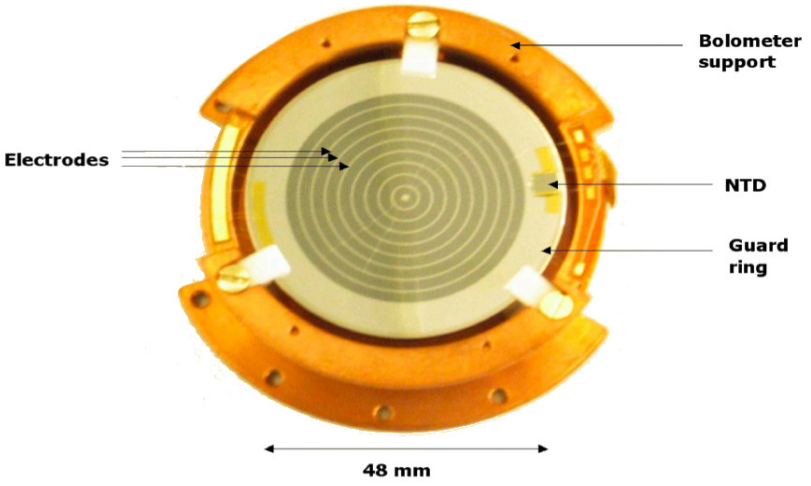

FIGURE 5.11: Picture of the ID201 detector.

fact there is a big energy deposit at the end of an alpha particle track where many recombinations can occur, leading to a Q value for alphas smaller than 1. The alphas are produced by ^{210}Po, one of the decay products of ^{210}Pb;

- βs that extend from low energy region (tens of keV) up to about 1 MeV, in the specific 1.17 MeV. Low energy betas (up to 16.5 keV) are produced by ^{210}Pb, while the higher energy ones are produced by ^{210}Bi (the energy transition for the disintegration of this nuclide is 1.17 MeV). As previously mentioned the electronic recoils are expected to have a Q value of 1. But in the plot it is clear that this is not the case. The reason for this behaviour is to be looked for in the poor charge collection of surface events. Charged impurities in the crystal can trap drifting electrons and holes and prevent them from reaching their intended electrodes. This results in an under-estimated ionization signal;
- γs that are in the region of $Q = 1$, are produced by the ^{210}Pb disintegration (46.5 keV);

- the contaminants are well implanted on the source. This is clearly visible looking at the α queue.

The low energy and low Q value regions are overwhelmed by events. This in principle could be an unavoidable background to the WIMP search. But if then we look at the bottom plot of Fig. 5.12, where there are represented just the

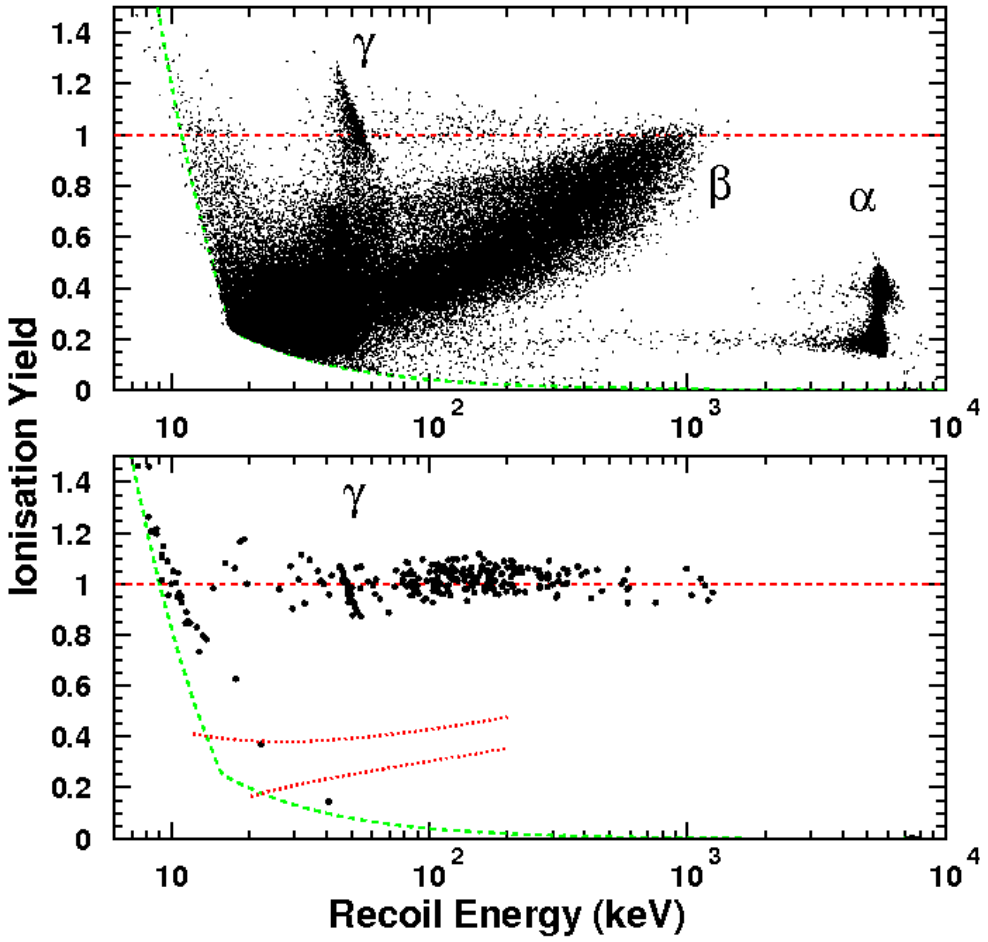

FIGURE 5.12: Q-plot for the ID201 detector equiped with a ^{210}Pb source. On the top the events in the total volume and on the bottom just the fiducial volume ones.

events that are in the fiducial volume of the detector, we understand the potential of the ID detector. The fiducial volume selection is done simply cutting the events that fall in the veto regions of the detector. The rejection potential for β events is thus estimated to be $3{\cdot}10^4$. To be more precise one event over $3{\cdot}10^4$ can be found in the nuclear recoil energy region.

After the fiducial volume cuts we can see that there are two "lines" in the electron recoil region: the K line at 10 keV due to the cosmogenic production of ^{68}Ge and ^{65}Zn isotopes, homogeneously distributed within the volume of the detector, and the 46.5 keV γ line. The intensity of the K line before and after the cuts allow us evaluating the fiducial mass of the detector.

5.4.2 ^{210}Po and ^{210}Bi diffusion

The studies about the Polonium-210 diffusion carried out in the frame of the CUORE collaboration pointed out that Polonium is the only element that diffuses inside copper, and this is a durative process. We have analyzed this employing a Silicon surface barrier detector at room temperature. Now we would like to carry out the same type of analysis but using a different detector and possibly looking at other elements.
The EDELWEISS detectors have the suitable features for analyzing the behaviour of different radioactive isotopes inside the source. In fact, as it was shown in Fig. 5.12 they have a good discrimination potential between the different types of interaction that occur in the detector.
As a first step we can see if there is still an evidence of ^{210}Po diffusion inside the copper (which is our matrix), and we can see if the diffusion profile changes as the time goes by. Simply looking at the alpha region of the top plot of Fig. 5.12 we see that ^{210}Po has diffused in the copper, the queue is quite long and it does extend to low energy, at least down to 1.17 MeV, then it fades out in the ^{210}Bi β region.
The detector was run with different polarization voltages of the electrodes in order to test its performances under different configurations. Concerning the diffusion profile for different polarizations of the detector, we see no major variations. Fig. 5.13 shows the ^{210}Po diffusion profile for two different detector voltages: -4 V and +4 V. This behavior tells us that, obviously, the electric field (about 10 V·cm^{-1} underneath the electrodes [115]) is not sufficient to stop the recoiling ^{210}Pb nucleus ($\sim$ 100 keV), preventing the diffusion of ^{210}Po, supposing that the diffusion mechanism is the recoil of the nucleus. The required electric field needs to be order of magnitudes more intense.

In the following, the durative diffusion of ^{210}Po was studied. Still the two +4 V and -4 V configurations have been studied (see Fig. 5.14). The analysis was carried out in the same way, comparing the diffusion profile of two Polonium-210 queue at different measurement times. Unfortunately the data at our disposal do not cover a long period of time (just few months), in fact we see no clear evidence of the durative diffusion.

Another nuclide that can be studied using EDELWEISS detectors is ^{210}Bi. This element has not be studied previously due to the lack of a suitable system. This analysis can help us in finding the real mechanism that leads to the Polonium-210

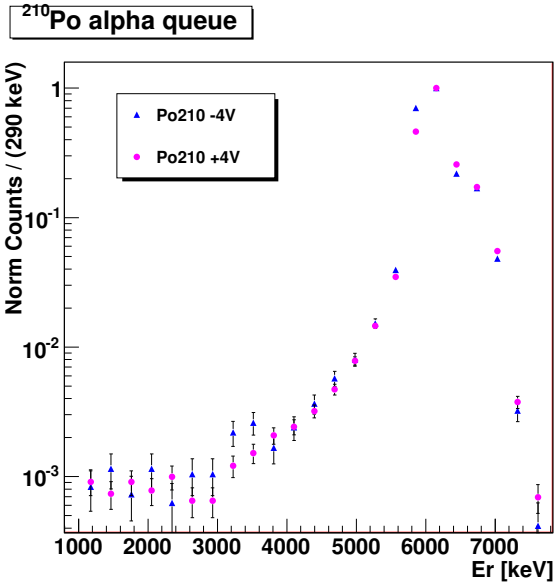

FIGURE 5.13: ^{210}Po diffusion profile of the same source for different polarizations of the detector.

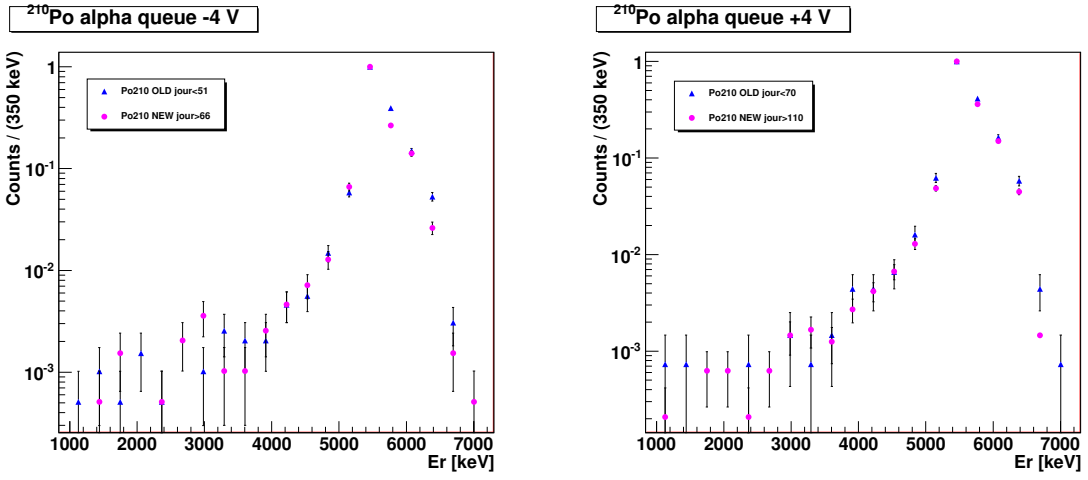

(a) (b)

FIGURE 5.14: ^{210}Po energy spectrum acquired at different time for a (a) negative and a (b) positive polarization of the detector.

diffusion. The electrons emitted by the ^{210}Bi emissions have a maximum energy of 1.17 MeV. The more the particles travel in the matrix the smaller will be the signal produced in the crystal, since the energy loss is uniform along the path length of the electron. This implies that there might be some problem in detecting low energy βs, expecially because they might be hidden by the ones produced by the ^{210}Pb. In Fig. 5.15 are represented the β spectra of ^{210}Bi acquired at different times, these have slightly a different shape from the theoretical one, because of the struggling of the electrons in the source, that tends to modify the lower energy part.

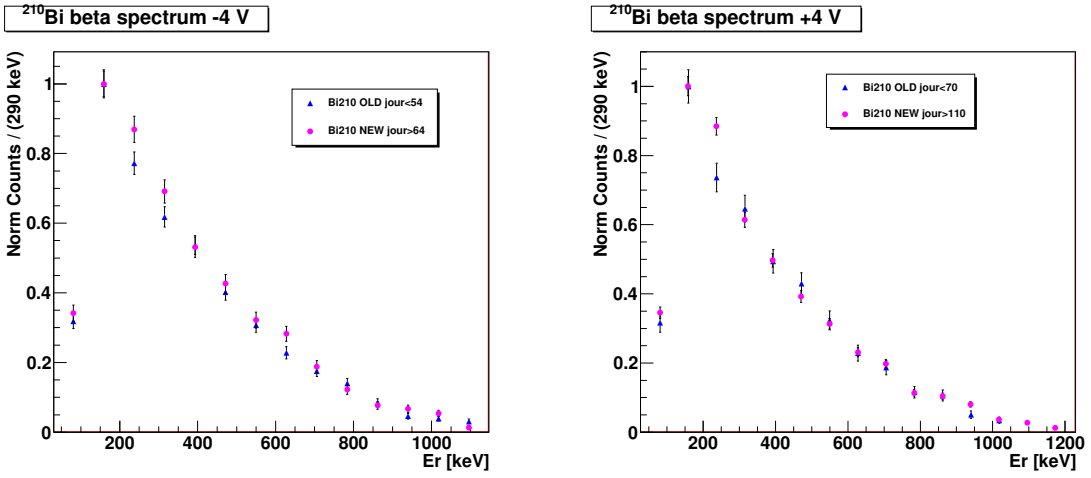

(a) (b)

FIGURE 5.15: ^{210}Bi β spectrum for two different detector voltages. In (a) the applied voltage is -4 V the plot shows a comparison between data acquired at different time ($\Delta t = 10$ d). In (b) the applied voltage is -4 V the plot shows a comparison between data acquired at different time ($\Delta t = 40$ d).

The initial energy of the spectra is about 70 keV, so that we are analyzing just Bismuth-210 electrons. In fact in the radon chain the only particles emitted after ^{210}Pb that have energy greater than 63.1 keV are the ^{210}Bi's electrons, the ^{210}Po α and γ (803.1 keV) emissions. Using the ID detectors we can easily flag and cut ^{210}Po alphas and neglect the gammas, since they have a small branching ratio ($\sim 10^{-3}$). In this way we are left with just ^{210}Bi events.

The evidence of Bismuth diffusion would come from the β distribution in the Q-plot, as already stated. Unfortunately we can not evaluate the implantation depth because we do not have enough information. In fact the β distribution depends both on the implantation depth of the source and on the charge collection profile, and we do not have enough information to untangle these two contributions. However, we can still analyze the durative diffusion of ^{210}Bi and see if its diffusion profile changes as a function of time. For the analyze time intervals (10 days and 40 days) it seems that there is no evidence of ^{210}Bi diffusion, as we have already shown in the analysis in §4.6.4.

5.4.3 Source characterization

We have seen that the source is characterized by the emissions of 3 radioactive nuclides: Lead-210, Bismuth-210 and Polonium-210. Unfortunately the source history is not well defined, also because after its handling (nitric acid cleaning

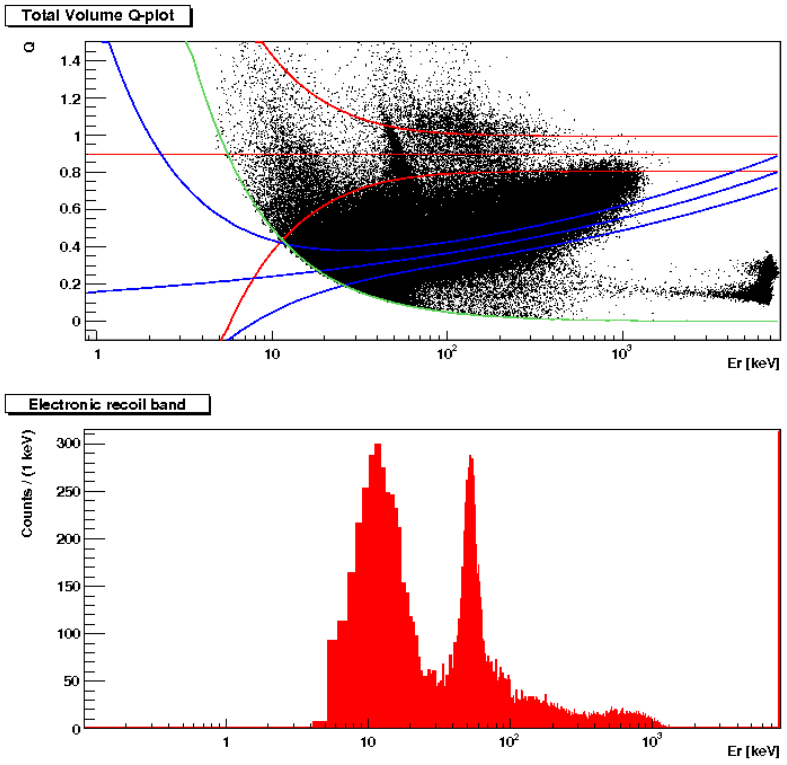

FIGURE 5.16: Top: Lead source total volume events on the ID201. Bottom: electronic recoil spectrum of the lead source on the ID201: the characteristic gamma line at 46.5 keV is clearly visible.

and warming up) any information concerning the mechanism of contamination has been lost. In this frame, we try to characterize the source, evaluating the relative abundance of the different detectable elements. This is possible thanks to the peculiarity of the EDELWEISS detectors, which are able to distinguish between the different types of interaction in the bolometer.

If we look at the recoil spectrum of the Q-plot of the source (Fig. 5.16 top), where the entire volume events are considered, we obtain the spectrum shown in Fig. 5.16 bottom. The 46.5 keV peak of ^{210}Pb is clearly visible and simply fitting the peak and the background we can calculate the number of Lead-210 gamma emissions. This is the best way to study the Lead concentration in the source, instead of looking at the low energy beta emissions.

The Bismuth-210 concentration in the source as been calculated using the Kurie plot of the beta spectrum. Since it is difficult to evaluate which events at low energy are produced by Bismuth and which by Lead (low energy betas), we extrapolate the low energy contribution of ^{210}Bi fitting the Kurie plot at lower energy. The integral of the function tells us the total number of bismuth beta events. In

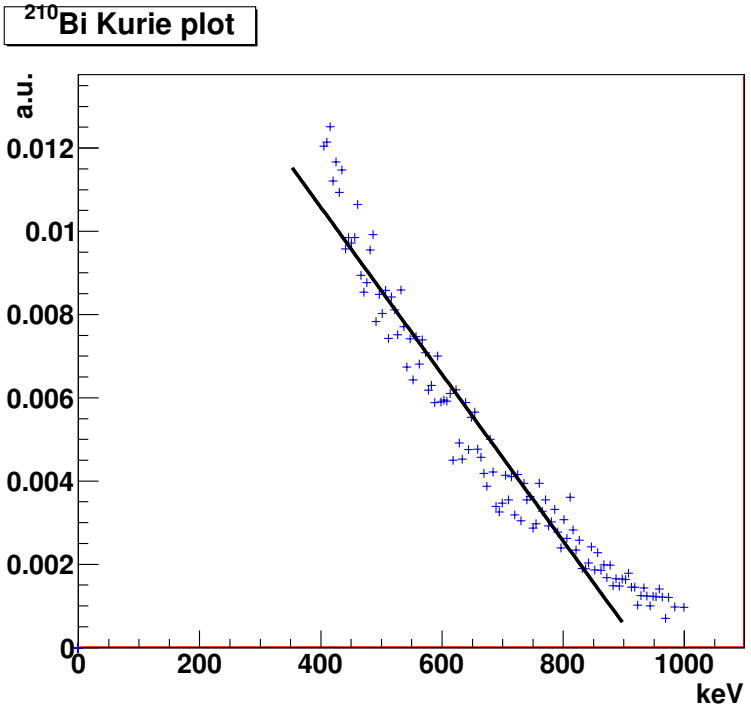

FIGURE 5.17: Kurie plot of the ^{210}Bi electrons of the source facing the ID201 detector. On the X-axis is represented the kinetic energy of the particles, while on the Y-axis a function of the momentum.

Fig. 5.17 is represented this analysis. The events were selected in the Q-plot applying the following cuts: recoil energy smaller than 1.17 MeV and greater than 100 keV (we get rid of low energy betas). We neglect the contribution of alpha events.

Finally the polonium concentration in the copper exposed to radon is computed simply applying a cut where E_r is required to be greater than 1.17 MeV. This will take into account just the ^{210}Po alpha emissions.

Now if we wish to evaluate the ratio between all three nuclides, we obtain the following result:

$$^{210}\text{Pb} \quad : \quad ^{210}\text{Bi} \quad : \quad ^{210}\text{Po} \tag{5.29}$$

$$1.0 \quad : \quad 0.95 \quad : \quad 0.86 \tag{5.30}$$

These ratios are evaluated normalizing the concentration per lead nuclide, since we assume the ^{210}Pb activity constant in time. Looking at those values we understand that the source is rather old, in a sense that the polonium has almost reached the equilibrium with the lead. At the same time we see that there is a problem concerning the values of bismuth concentration with respect to the polonium one. In fact, since the ^{210}Bi has a rather short half-life (about 5 days) compared to ^{210}Pb

(and ^{210}Po), we expect it to be in equilibrium with ^{210}Po. Thus there must be a problem in defining the α and β regions in the Q-plot.
Focusing our attention on the top image of Fig. 5.16 we see that in the region of small Q-value (smaller than 0.3) there is a sort of superposition between the Polonium-210 α queue and the Bismuth-210 β cloud: this does not allow us estimating the right abundances of the two elements. However this information tells us that polonium queues can extend to low energy (less than 1 MeV) and thus give some problems in the region of interest for the WIMP search. A better analysis about the possible contributions of alpha particles to the background of EDELWEISS is carried out with two other detectors ID401 and ID5, where the alpha source is less intense, and the beta background allows a lower energy study.

5.4.4 Low energy alphas

Two detectors were chosen for carrying out a low energy analysis for the alpha particles amoung the interdigitized EDELWEISS-II detectors. The parameters used for making the detector choice were the performances and the alpha contaminations. In fact we would like to use a detector with good baseline energy resolution and with a significant ^{210}Po contaminations (see Appendix B.1 and B.2). The good energy resolution is needed for allowing a good low energy analysis: in this way electronic and nuclear recoils bands will be much separated. The high alpha contamination is needed to avoid too poor statistics. The ID401 and ID5 were thus analyzed.

A first level analysis is performed consisting on the evaluation of energy and several pulse shape parameters associated to each raw pulse waveform recorded by the data acquisition system. Simple cuts on the χ^2 were applied, but we will not focus on this subject because it has not interesting connections with the analysis that we want to carry out. A second level analysis is carried out in order to determine the physics events in the detectors. The results obtained from the second level analysis is shown in Fig. 5.18 for the ID401 detector (the bolometer with the best baseline resolutions). The ID401 shows a significant contamination of ^{210}Po at a recoil energy of 5.3 MeV. As already seen in the ID201 bolometer the contaminant seems to be implanted in the source (Copper or Germanium), this is the explanation for the tail that extends to low energy regions.
In this section we will try to estimate if the Polonium-210 alpha contamination can be considered as a source of background in the WIMP energy region even after

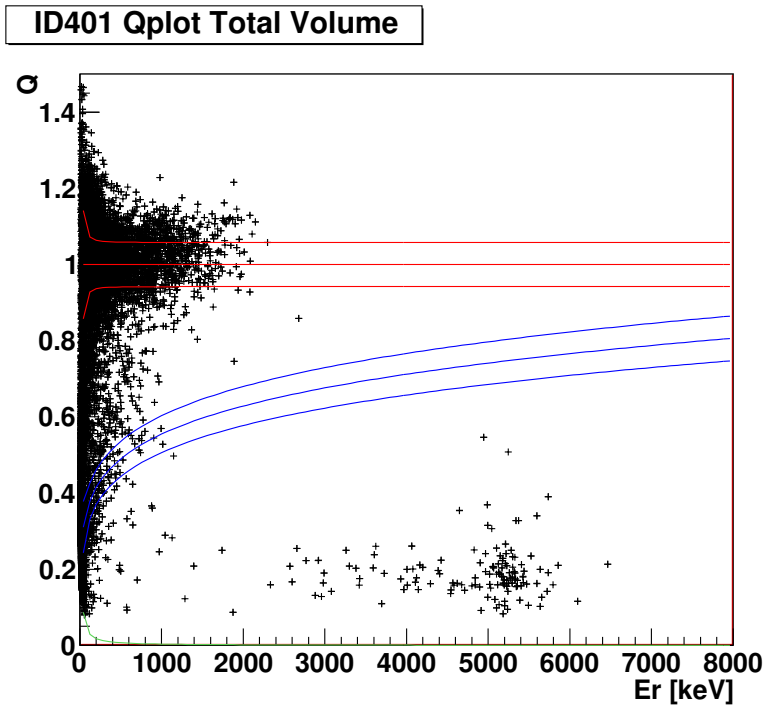

FIGURE 5.18: Q-plot of the total volume event for the ID401 detector.

the fiducial volume cuts. Actually all the alphas are expected to be stopped within the veto region, because of the large veto areas, but there might be a chance that an alpha produces an ionization signal in the fiducial electrodes bigger than the one produces on the vetos.

Here, to be more precise we will look for alpha events in the fiducial volume of the detector and see if the "α band" has an intersection with the nuclear recoil band, giving rise to problems of identification of events that lie in the intersection of the two regions.

Looking at Fig. 5.18 we will try to define an *alpha band*. The ID201 detector study demonstrated that alpha particle tails can extend to really low energy region ($<$ 1 MeV). So in order to define the alpha band we must consider this result, at the same time the alpha *cloud* occupies a rather large area.

We will apply a cut in such a way that all the events above an energy recoil of 1170 keV (transition energy for the disintegration of ^{210}Bi) will be taken into account. We assume that the only contribution to the alpha region (of non-alpha particles) is produced by leakage of beta events coming from the ^{210}Bi disintegration and neutron/WIMP events, but these will have a lower rate. The cut on the Q variable is applied in a way that maximizes (at a level of 98%) the number of alpha events considered (see Fig. 5.19). We apply no lower cut on the Q distribution because there is an undefined behaviour of low energy alphas. In fact an alpha that has an

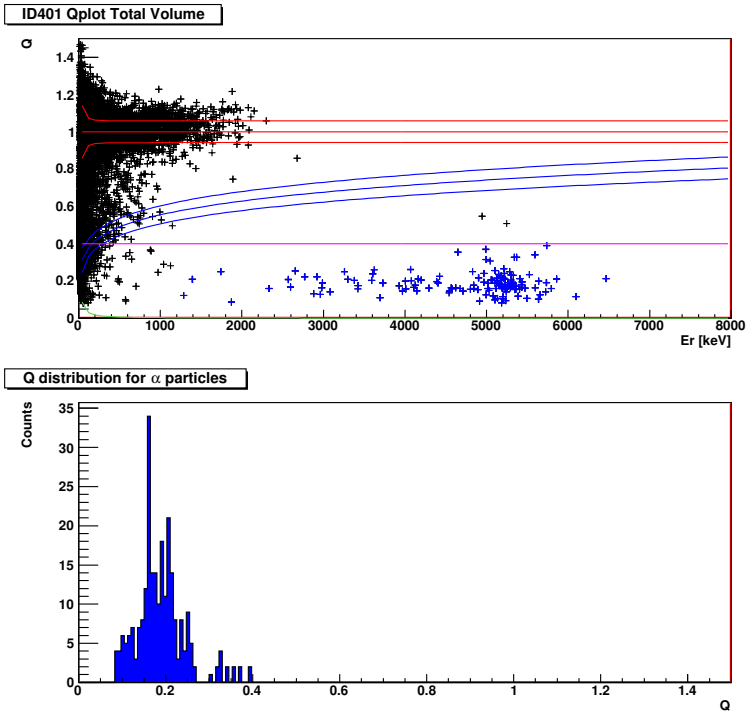

FIGURE 5.19: Top: Q-plot of the total volume events. Bottom: distribution of Q values for $E_r > 1170$ keV.

energy recoil smaller than 500 keV might not ionize like a 5.3 MeV alpha. This means that it is possible that the Q value for struggling alphas tends to zero as the energy recoil tends to zero. So the lower limit for the alpha Q value is set to 0 (conservative hypothesis). For the ID401 Germanium bolometer the applied cut corresponds to $Q < 0.4$.

For better analyzing the alpha events we select all two electrodes events using the variable:

$$\frac{\text{(Veto1 - Veto2)}}{E_i}, \tag{5.31}$$

where Veto1 (Veto2) is the energy of the ionization signal on the veto (one on the top and the other on the bottom surfaces) and E_i is the total ionization signal. Now if we want to look at just the fiducial volume events we ask that the Guard 1, Guard 2, Veto 1 and Veto 2 ionization energy signals are smaller than their baseline energy resolution, so all the fiducial volume events are kept. In addition for selecting just the two electrodes fiducial volume events we apply the cut that keeps all the events where the two collector electrodes show an equal value.

The distribution of the variable from equation 5.31 is shown in Fig. 5.20 and it allows distinguishing different types of events depending on their values:

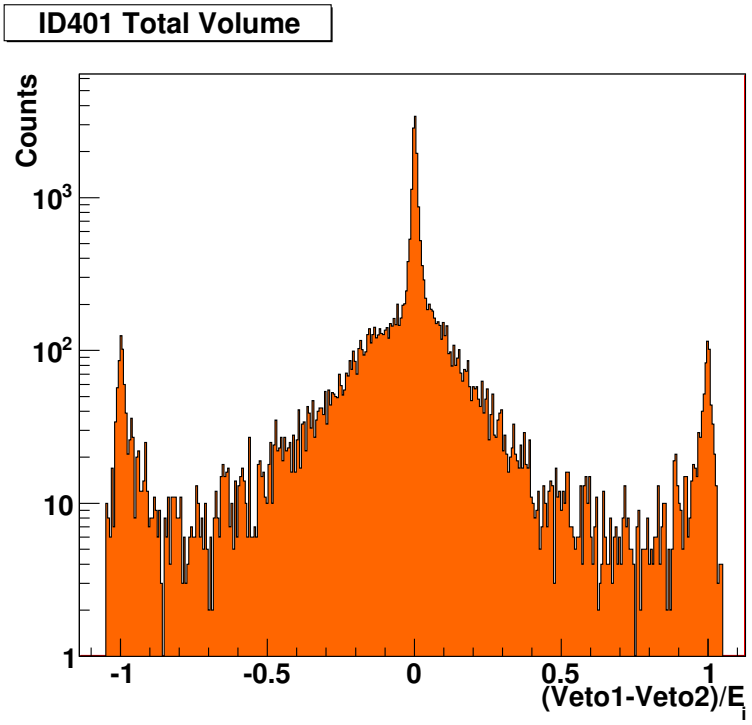

FIGURE 5.20: Distribution of the (Veto1 - Veto2)/E_i variable used for selecting two electrodes fiducial volume events.

- $= 0$, we select just the events that are triggered on the two fiducial collecting electrodes;
- $= \pm 1$, we select surface events (top or bottom surface of the detector), since all the energy is released on the veto electrodes;
- > 0 & < 1 (or $>$ -1 & < 0), we select events whose ionization signal is shared between more than 2 electrodes. This means that for sure one of the 2 electrodes is a veto (or guard) electrodes.

We are interested in selecting the events that have (Veto1 - Veto2)/$E_i = 0$. Applying all the cuts just mentioned we obtain for the ID401 the Q-plot for the fiducial volume shown in Fig. 5.21. Looking at the bottom of Fig. 5.21 we can make two major remarks. The first concerns the fact that there is an intersection between the alpha region and the nuclear recoil band. So there could be a chance that if there is an alpha in the fiducial volume this could be in the nuclear recoil band, so now we have to demonstrate that there are alphas in the bulk and thus alpha particles are a background source for the WIMP search experiment. The second remark is the presence of 2 events in the intersection between the two region. The higher energy event is in coincidence with the muon veto, so it can be excluded to

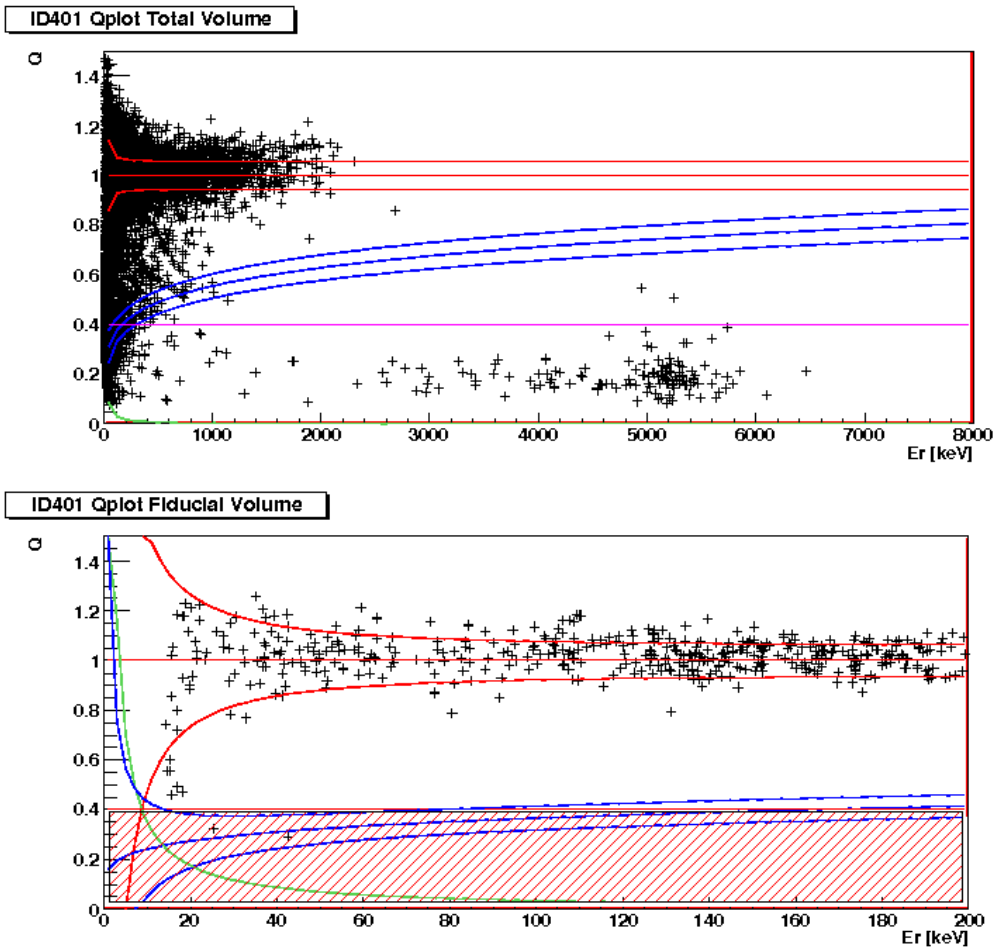

FIGURE 5.21: Top: total volume Q-plot. Bottom: fiducial volume Q-plot, and the red box represents the alpha region.

be an alpha or WIMP/neutron event. But still we have one event that could be considered either as a WIMP/neutron event but also as an alpha (or even a beta that has leaked). Unfortunately there are no further parameters that allow us to identify what kind of particle have produced this event.

The ID401 detector has really good performances but the alpha source was not enough intense for a high statistics analysis. We decided to study another detector with still high performances but with an alpha rate about 200 times more intense: this detector is the ID5. Even if this detector is missing one guard electrode, as already mentioned in section §5.3, the analysis is still possible by means of the fact that a guard event comes always with a signal on either the vetos or the collector electrodes. The analysis has been carried out exactly in the same way as it was done for the ID401 detector. In Fig. 5.22 is shown the Q-plot showing the total volume events. We see clearly that the alpha contamination is significant and that it extends to really low energies, well below 1 MeV. We apply a cut at the energy

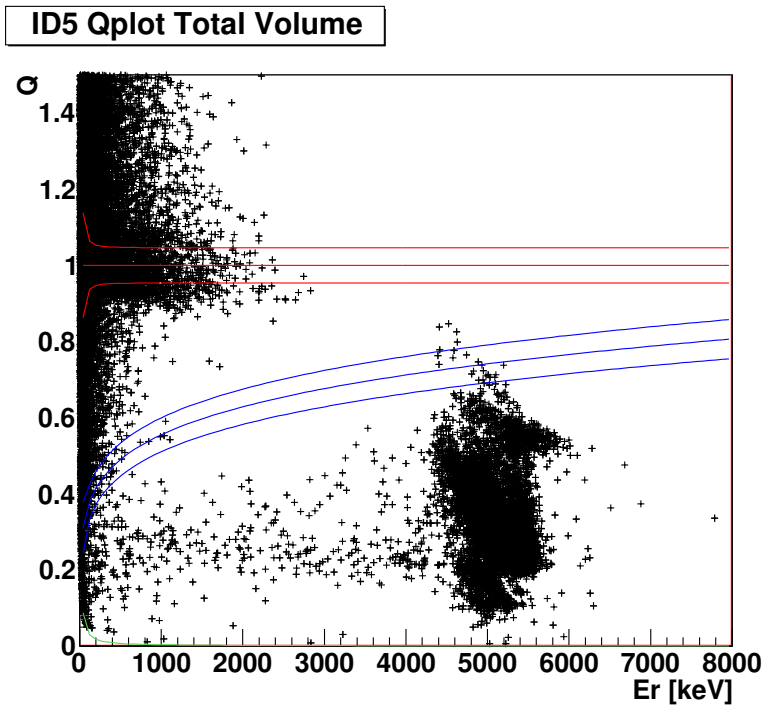

FIGURE 5.22: Q-plot total volume events for the ID5 detector.

recoil ($E_r > 2615$ keV), selecting the alpha particles in the Q-plot (see Fig. 5.23). As already explained we apply the cut $Q < 0.59$ (that includes the 98% of alpha events, under the same hypotheses of the study of the ID401 detector) together with $E_r > 1170$ keV. Thus selecting just the two electrodes fiducial volume events we obtain the Q-plot shown in Fig. 5.24.

In the alpha region there are 4 low energy events. The event labelled 2 and 3 can be neglected because they are in coincidence with the muon veto, so they are muon-induced neutrons. Event number 4 can be considered as a leak of the 10 keV X-ray, it is really close to the border line. But event number 4 can be considered as an alpha event, in fact it can not be neither a neutron or a WIMP because (at a 90% C.L.) it is out of the nuclear recoil band.

The presence of this event allows us to give an upper limit on the alpha rejection of alpha events on ID detectors. The limit is given by the number of alpha events in the fiducial volume over the total number of alpha in the total volume for an energy recoil higher than 1170 keV, since for lower energy recoil it is still possible to have some leak of γ (β) events in the alpha band. This result has to be considered together with the result of the analysis on the detector ID201. In fact this detector also shows an event at about 40 keV under the nuclear recoil band after the fiducial volume cuts. The two detectors with the highest ^{210}Po concentration have the same feature.

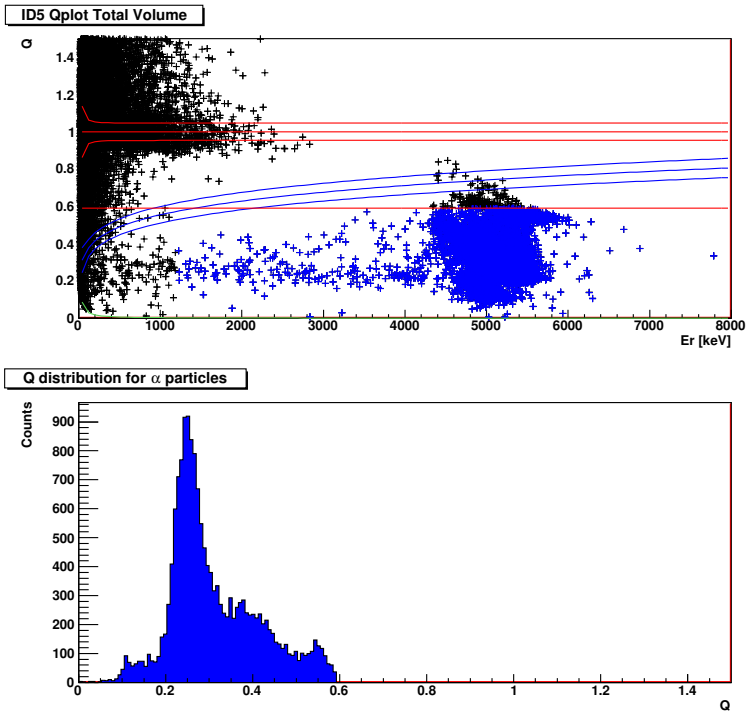

FIGURE 5.23: Top: Q-plot of the total volume events. Bottom: distribution of Q values for $E_r > 1170$ keV.

So for the ID5 detector, for a the total number of α events with E_r higher than 1170 keV (16873 events) in the total volume there is one that occurs in the fiducial volume. The alpha rejection power for the ID5 detector can be estimated to be 1/16873, for an alpha contaminant implantation of 300±100 nm, evaluated using Monte Carlo simulations. The uncertainty on the evaluation of the implantation depth is due to the poor energy resolution on the alpha peak, which hides the tail.

For better understanding the behaviour of the alpha queue, we analyse the energy alpha region where the energy recoil is greater than 1 MeV. We create various boxes around the alpha queue and we look at the distribution of events amoung the different electrodes. We expect to have some kind of relation between the contamination depth (hence the E_r) and the distribution of the event per number of electrodes. For example we expect to have more 3 electrode events as the E_r increases, or to be more precise that less energetic alphas have more chance to be collected on 2 electrodes instead of being collected on 3, because of their penetrating power. In Fig. 5.25 is illustrated the distribution of the variable:

$$\frac{\text{(Fid1 - Fid2)}}{E_i}, \tag{5.32}$$

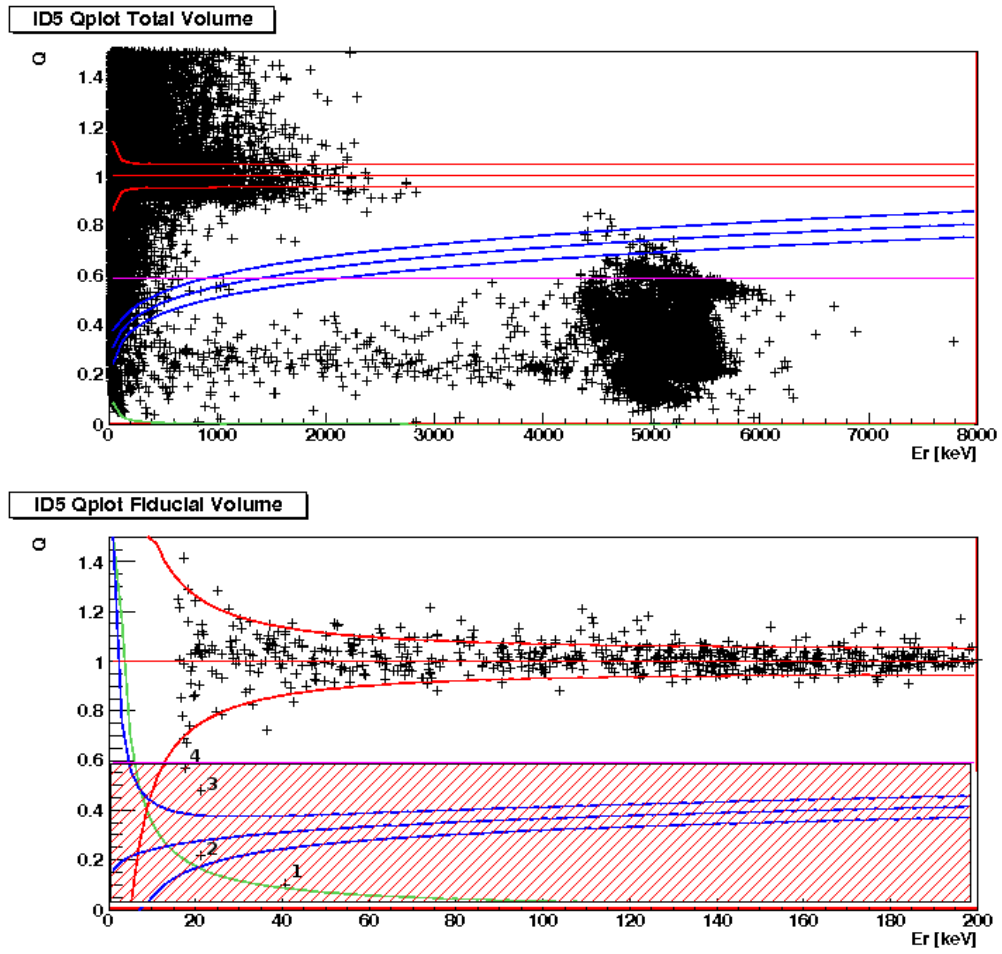

FIGURE 5.24: Top: total volume Q-plot. Bottom: fiducial volume Q-plot, and the red box represents the alpha region.

where Fid1 and Fid2 are the fiducial volume electrodes. This variable gives the same informations as the variable shown in equation 5.31. We see no major difference between the distribution of the 3 alpha *boxes* that we have built (each of them is 1 MeV large starting from 1.2 MeV and the height is $Q < 0.59$). They all show the same behaviour, the events in the alpha queue are not related to the number of electrodes that collect the charge, and thus at the depth that they reach.
The distributions of Fig 5.25 prove that the weak point in the power rejection of alpha particle in the interdigitized detectors is not due to the penetrating power of the particles, but instead it is due to the electric field distribution at the interaction site. We can imagine that the event has occured just underneath a fiducial electrode, the ionization signal produced has been mainly collected by the fiducial volume electrodes. Even if we are in a region with intense electric field, the event can occur around the electric field line that connects the two fiducial electrodes. In such a way that the signal produced on the fiducial eletrodes is much higher

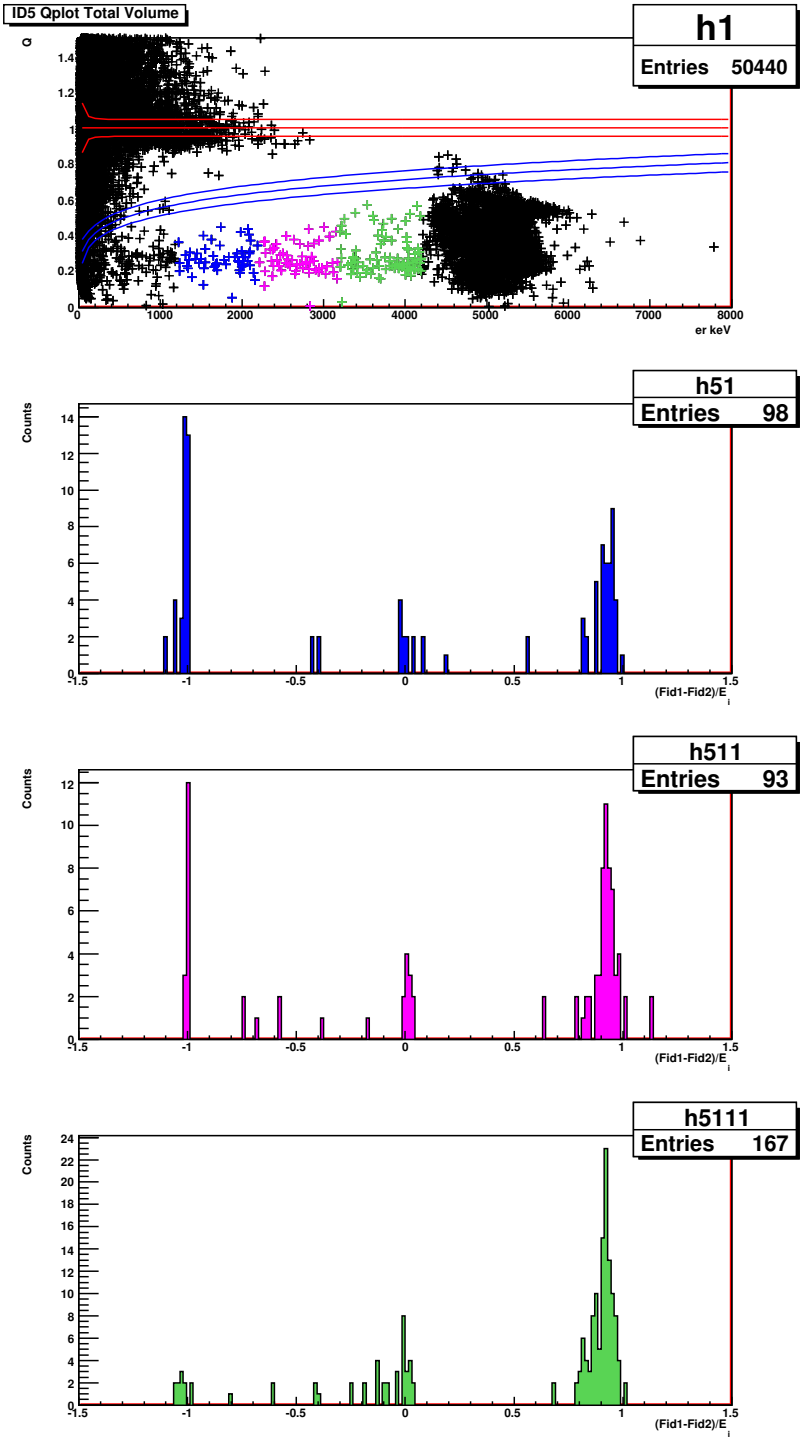

FIGURE 5.25: Top: Q-plot of the ID5 detector. Bottom: distributions of the (Fid1 - Fid2)/E_i variable for the three different selected regions.

than the ones produced on the vetos (see Fig 5.26).

In conclusion we can state at a confidence level of 90% the event at 40 keV can not be considered as a neutron or a WIMP, and thus it could be a degraded alpha particle. This implies that degraded alpha contaminations might be a background

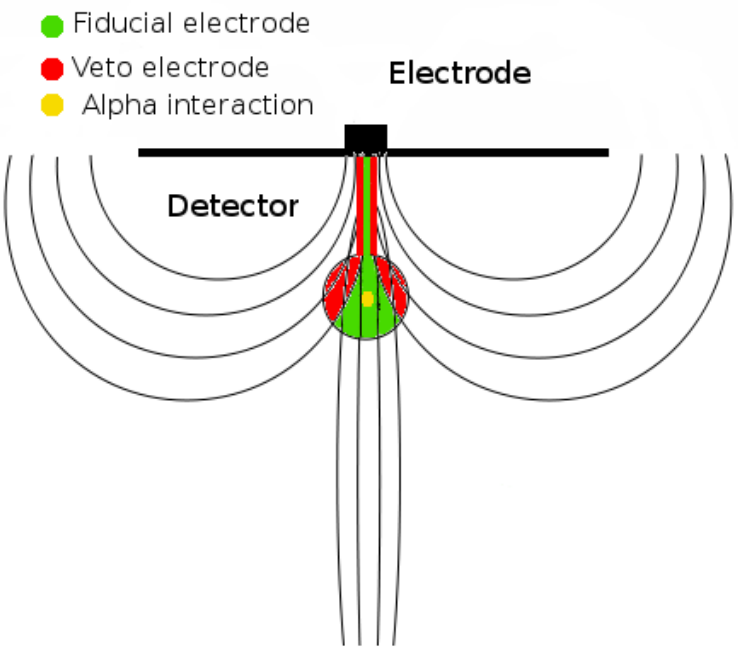

FIGURE 5.26: Sketch of the alpha event on the ID5 detector.

source in the region of interest of the WIMP search. The α rejection power is estimated to be $5.93 \cdot 10^{-5}$.

Chapter 6

Conclusions

In this thesis work we have presented the main background sources for rare event experiments like neutrinoless double beta decay and dark matter. We have had a closer look to the CUORE (and CUORICINO) and EDELWEISS experiments and we have understand that these experiments are affected by Radon-induced contamination (^{210}Pb, ^{210}Bi and ^{210}Po).

In the frame of the CUORE experiment we have demonstrated how surface contaminations are really a critical issue for the expected background of the experiment. One possible source of surface contaminations is the exposure of the CUORE detector to a non-controlled environment with a high Rn concentration. A thorough analysis has been carried out in order to understand the mechanisms of implantation of radionuclide on sensitive parts of the detector and the time evolution of the contaminants that leads to the production of background sources on the detector.

The exposure leads to a significant Polonium-210 contamination on the surface (less than 1 nm) and on the surface sub-layers ($\sim$ 300 nm). The implantation depth and the surface activity are strictly linked to the time exposure of the samples to Rn. Moreover the ^{210}Po activity changes has the time goes by, since it is trying to reach the equilibrium with other elements of the chain (^{210}Pb), but at the same time the diffusion depth evolves and the contaminants migrate towards the inside of the sample, causing a deeper contamination.

Wherever there is a Polonium-210 contamination there is also a Lead-210 contamination. But the mechanisms that leads to Lead-210 contaminations can be different. In fact we have seen that the ^{210}Pb gravimetric deposition is not the main source of contaminants but instead the implantation and sticking are the

main mechanism which cause a contamination four time larger.
All the previous results allowed us to estimate the constraints about the Rn concentration in all the environments (e.g. clean room) where the CUORE detector will be assembled and handled, in a way that the Rn exposure will not cause any production of surface contamination that can be a background source in our region of interest.

The problem of surface contaminations concerns not only neutrinoless double beta decay but also rare event experiments as dark matter experiments.
In the frame of the EDELWEISS collaboration we have still carried out the study of the contaminations induced by Rn exposure. The analysis has been managed in the same way as for CUORE, but together with the study of Polonium-210 diffusion profiles, we have tried to look for the same kind of features in ^{210}Bi. This was possible by means of the EDELWEISS detectors that are able to distinguish between various types of interaction in the detector according to the particle that is deposing energy. In fact EDELWEISS detector are able to distinguish between γ/β, α and neutrons particles.
In analyzing the contamination profiles of Bismuth-210 we have encountered the problem of low energy alphas, to be more precise alpha particles that leave in the detector small amount of energy either because of their struggling in the matrix source or because of surface contaminations on the detectors.
Through an accurate study of the alpha contamination on the EDELWEISS detectors, we have found out that there are alpha events that are not vetoed and thus can reach the fiducial volume, leading to an alpha background in the region of interest for the WIMP search. As a consequence, we have estimated the rejection power of the EDELWEISS detectors for alpha particles.
In the next generation experiments looking for DM and DBD0ν, where is foreseen an increase in the mass, the surface contaminations will become more and more important since a mass increase implies an increase of detector surfaces and passive material facing the detector. Thus the controll of the environment in which the detector is handled is crucial. At the same time a carefull analysis of degraded alpha is compulsory, this can be carried out using special calibrated source.
As the EDELWEISS shows, probably, the future of DBD0ν search is in the development of detector with double read-out of heat-charge or heat-light. Using this technique it might be possible to get rid of all alpha surface contaminations discriminating them from the beta signals.

Appendix A

Natural decay series

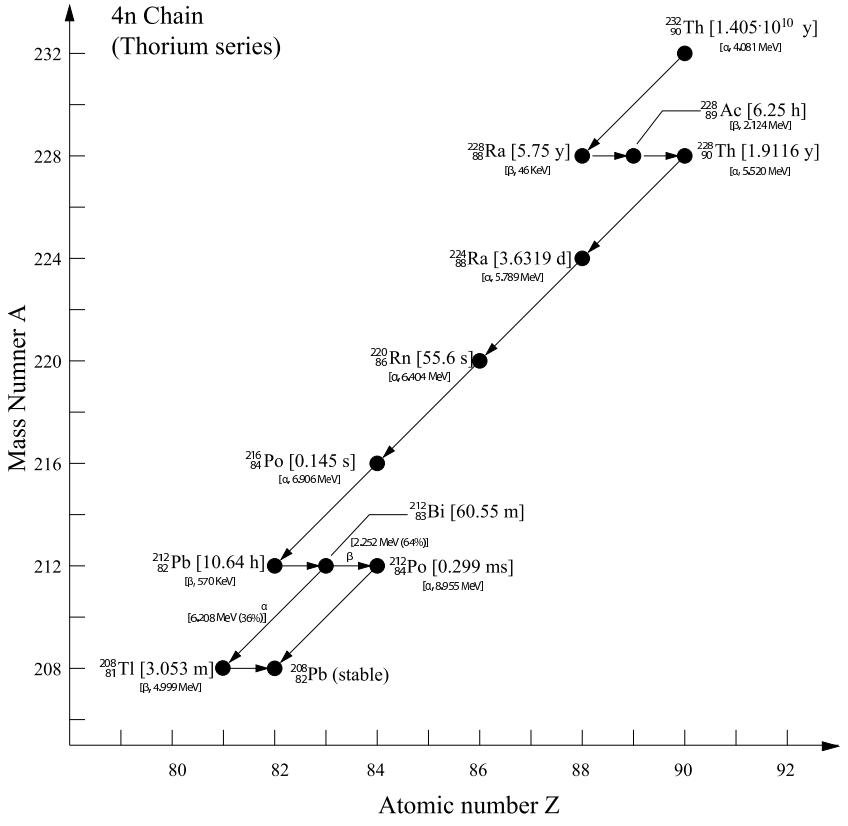

FIGURE A.1: ^{232}Th decay chain

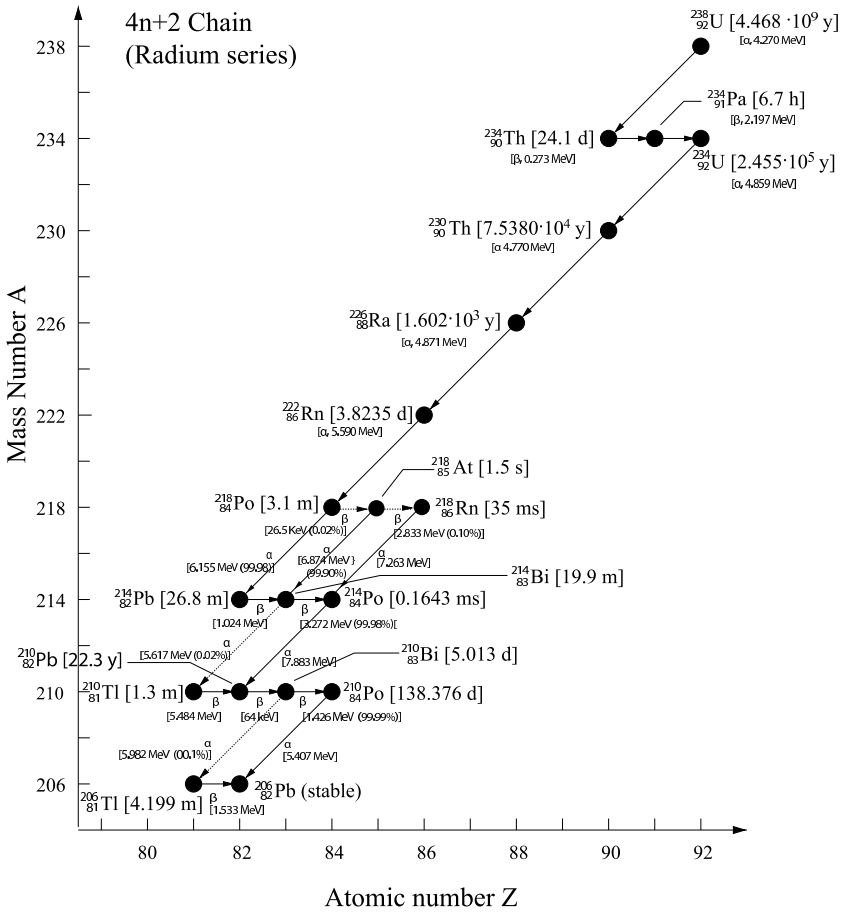

FIGURE A.2: ^{238}U decay chain

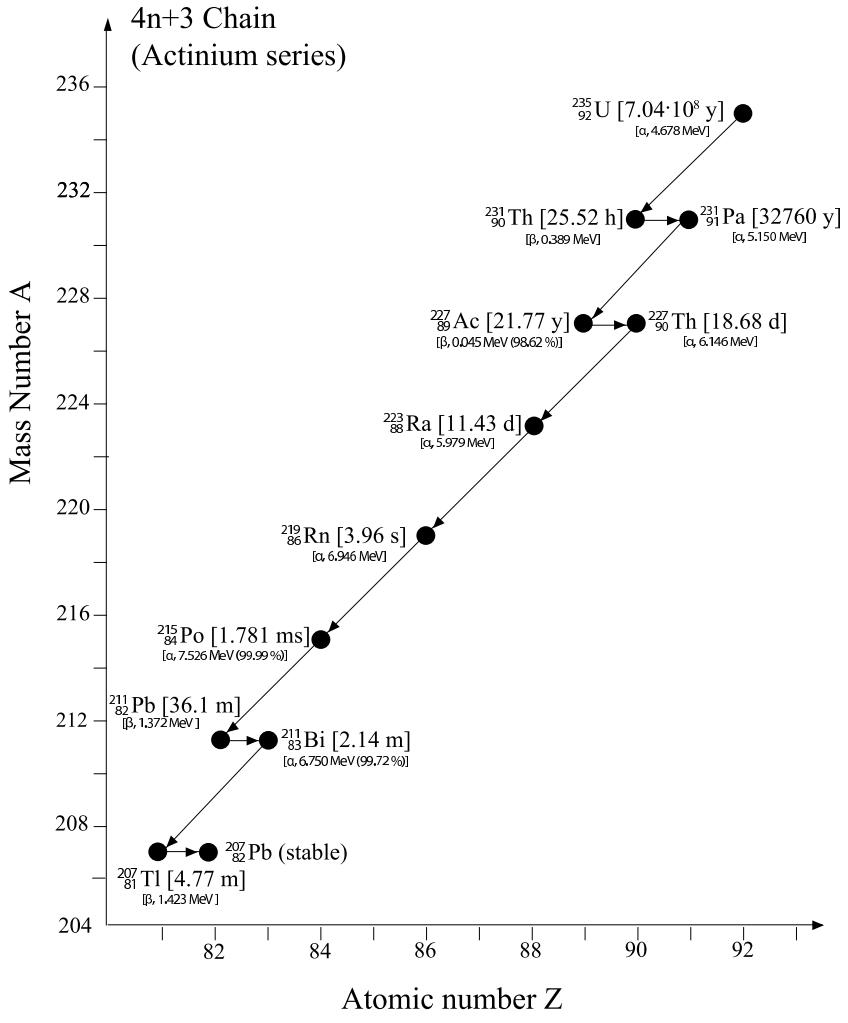

FIGURE A.3: ^{235}U decay chain

Appendix B

EDELWEISS-II Interdigitized detectors

	Heat	Coll 1	Coll 2	Veto 1	Veto 2	Guard G	Guard H
ID401	1.3	1.2	1.4	1.6	1.4	4.8	1.6
ID402	1.7	1.5	1.4	1.6	1.3	3.0	–
ID403	2.1	1.3	1.1	1.9	1.3	9.0	1.9
ID404	1.1	1.3	1.2	1.4	1.4	2.0	1.3
ID405	0.87	1.3	2.2	1.3	2.3	4.6	1.4
ID2	1.4	1.5	1.1	1.8	1.5	1.6	1.6
ID3	1.0	1.2	1.5	1.3	1.1	1.9	1.4
ID4	0.82	1.6	1.8	1.2	–	2.6	12.0
ID5	1.1	3.3	1.6	2.7	1.4	1.7	–
ID6	0.67	1.0	0.7	1.1	1.6	–	1.3

TABLE B.1: Baseline energy resolutions (FWHM in keV) for ID EDELWEISS-II detectors.

	Days	Total rate [c·d^{-1}]	Top [c·d^{-1}]	Bottom [c·d^{-1}]
ID401	134.8	2.55 ± 0.14	0.16 ± 0.03	0.22 ± 0.04
ID402	108.0	3.08 ± 0.17	0.65 ± 0.08	0.36 ± 0.06
ID403	103.1	3.10 ± 0.17	0.72 ± 0.08	0.19 ± 0.04
ID404	147.7	3.27 ± 0.15	0.60 ± 0.06	0.16 ± 0.03
ID405	61.8	4.68 ± 0.28	4.68 ± 0.28	0.23 ± 0.06
ID2	84.3	1.70 ± 0.14	0.42 ± 0.07	0.38 ± 0.07
ID3	138.8	2.23 ± 0.13	0.55 ± 0.06	0.27 ± 0.04
ID4	129.7	15.00 ± 0.34	0.05 ± 0.02	3.69 ± 0.17
ID5	138.5	149.00 ± 1.04	57.95 ± 0.65	59.60 ± 0.66
ID6	150.3	1.07 ± 0.08	0.25 ± 0.04	0.16 ± 0.03

TABLE B.2: Alpha rates per day (total, top side and bottom side).

Acknowledgements

Many people helped and guided me during this Ph.D. work. First of all I would like to thank my supervisors: Prof. Ezio Previtali for his constant support and for always having an answer to all my questions. I think he has transmitted to me a tiny part of his great passion for Physics; Prof. Corinne Augier for all the time she spent for making this Ph.D. work possible, and for showing me that Physics is not just about neutrinos, but there is something else. I owe her a lot.
I am really greatful to Dr. Massimiliano Clemenza for his huge patience and for all its precious suggestions about experimental Physics and other stupid things...
Obviously, the best supporters I had were the people I shared the office with. I had a great time with great people: Cecilia, Elena, Luca, Marco, Marcus and Silvia, grazie, especially for your infinite patience and your careness.
A special thank goes to the physicists I met during the last 3 years, people that try together with me to live "normal lives"in a strange world: Filippo, Michela, Lucia, Silvano, Giulia, Roberto, Viola, Abu, Luca and Johann.
There is something out there, which is not Physics. Thanks to Andrea, Stefano, Massimo and Matteo for showing me the rest of the World.
Finally I would like to thanks my parents for giving me the possibility to study and explore the World I live in, and my brother and sisters for always being in the right place at the right moment.

Bibliography

[1] A. Strumia and F. Vissani. Neutrino masses and mixings and... *Arxiv preprint hep-ph/0606054*, 2006. 1, 2.2.1, 2.4

[2] J. Menendez, A. Poves, E. Caurier, and F. Nowacki. Deformation and the Nuclear Matrix Elements of the Neutrinoless Double Beta Decay. 2008. 1, 2.5

[3] RH Sanders and KG Begeman. Modified Dynamics/MOND/as a Dark Halo. *Monthly Notices of the Royal Astronomical Society*, 266:360, 1994. 1, 2.8

[4] AC Fabian and SW Allen. Proceedings of the XXI Texas Symposium on Relativistic Astrophysics held on December 9–13 2002. *Florence, Italy [astro-ph/0304020]*, 2003. 1, 2.9

[5] K. Hagiwara, K. Hikasa, K. Nakamura, M. Tanabashi, M. Aguilar-Benitez, C. Amsler, RM Barnett, PR Burchat, CD Carone, C. Caso, et al. Review of particle physics. *Phys. Rev. D*, 66(1-I):010001–213, 2002. 1, 2.10, 4.4.2

[6] G. Gerbier. Edelweiss-ii: Searching for wimps. last results using ge cryogenic detectors with interleaved electrodes. In *Patras Workshop on Axions*, July 2010. 1, 2.13, 5.3, 5.10

[7] Z. Ahmed et al. CDMS collaboration. *Phys. Rev. Lett*, 102(011301):0802–3530, 2009. 1, 5.9

[8] VN Lebedenko, HM Araújo, EJ Barnes, A. Bewick, R. Cashmore, V. Chepel, A. Currie, D. Davidge, J. Dawson, T. Durkin, et al. Results from the first science run of the ZEPLIN-III dark matter search experiment. *Physical Review D*, 80(5):52010, 2009. 1, 5.10

[9] V. Sanglard et al. the EDELWEISS Collaboration. *Phys. Rev. D*, 71:122002, 2005.

[10] G. Angloher, M. Bauer, I. Bavykina, A. Bento, A. Brown, C. Bucci, C. Ciemniak, C. Coppi, G. Deuter, F. Von Feilitzsch, et al. Commissioning run of the CRESST-II dark matter search. *Astroparticle Physics*, 31(4):270–276, 2009. 1, 5.10

[11] J. Angle, E. Aprile, F. Arneodo, et al. XENON collaboration. *Phys. Rev. Lett*, 100(021303):0706–0039, 2008. 1, 5.9

[12] Z. Ahmed, DS Akerib, S. Arrenberg, CN Bailey, D. Balakishiyeva, L. Baudis, DA Bauer, PL Brink, T. Bruch, R. Bunker, et al. Dark Matter Search Results from the CDMS II Experiment. *Science*, 327(5973):1619–1621, 2010.

[13] E. Armengaud, C. Augier, A. Benoit, L. Berge, O. Besida, J. Blumer, A. Broniatowski, A. Chantelauze, M. Chapellier, G. Chardin, et al. First results of the EDELWEISS-II WIMP search using Ge cryogenic detectors with interleaved electrodes. *Arxiv preprint arXiv:0912.0805*, 2009. 5.1.2.2, 5.3

[14] E. Aprile, K. Arisaka, F. Arneodo, A. Askin, L. Baudis, A. Behrens, K. Bokeloh, E. Brown, JMR Cardoso, B. Choi, et al. First Dark Matter Results from the XENON100 Experiment. *Physical Review Letters*, 105(13): 131302, 2010. 1, 5.10

[15] PG Litovchenko, D. Bisello, A. Candelori, AP Litovchenko, AA Groza, AP Dolgolenko, VI Khivrich, LI Barabash, VF Lastovetsky, LA Polivtsev, et al. Radiation hardening of silicon for detectors by preliminary irradiation. In *Diffusion and defect data part B solid state phenomena*, pages 399–404. Scitec Publications Ltd, 2004. 2, 2.1

[16] O. Cremonesi. Double beta decay searches. In *Journal of Physics: Conference Series*, volume 202, page 012037. IOP Publishing, 2010. 2, 2.1

[17] HV Klapdor-Kleingrothaus, A. Dietz, IV Krivosheina, C. Dörr, and C. Tomei. Support of evidence for neutrinoless double beta decay. *Physics Letters B*, 578(1-2):54–62, 2004. 2, 1, 2.2.1, 2.2, 4

[18] M. Maltoni, T. Schwetz, M. Tórtola, and J.W.F. Valle. Status of global fits to neutrino oscillations. *New Journal of Physics*, 6:122, 2004. 2, 2.3

[19] Ardito R. et al. CUORE: A cryogenic underground observatory for rare events. *Arxiv hep-ex/0501010*, 2005. 2, 2.4, 4.5, 4.6.4

[20] DS Leonard, P. Grinberg, P. Weber, E. Baussan, Z. Djurcic, G. Keefer, A. Piepke, A. Pocar, J.L. Vuilleumier, J.M. Vuilleumier, et al. Systematic study of trace radioactive impurities in candidate construction materials for EXO-200. *Nuclear Instruments and Methods in Physics Research Section A: Accelerators, Spectrometers, Detectors and Associated Equipment*, 591(3): 490–509, 2008. 2, 2.4

[21] R. N. Mohapatra and A. Y. Smirnov. Neutrino Mass and New Physics. *Ann. Rev. Nucl. Part. Sci.*, 56:569–628, 2006. doi: 10.1088/1742-6596/53/1/003. 2.1

[22] G. L. Fogli, E. Lisi, A. Marrone, A. Palazzo, and A. M. Rotunno. Neutrino mass and mixing parameters: A short review. 2005.

[23] P. Fisher, B. Kayser, and K.S. McFarland. Neutrino mass and oscillation. *Annual Review of Nuclear and Particle Science*, 49(1):481–527, 1999.

[24] J.N. Bahcall and C. Peña-Garay. Solar models and solar neutrino oscillations. *New Journal of Physics*, 6:63, 2004.

[25] C. Bemporad, G. Gratta, and P. Vogel. Reactor-based neutrino oscillation experiments. *Reviews of Modern Physics*, 74(2):297–328, 2002. 2.1

[26] S. Pascoli, S. T. Petcov, and W. Rodejohann. On the neutrino mass spectrum and neutrinoless double-beta decay. *Phys. Lett.*, B558:141–156, 2003. doi: 10.1016/S0370-2693(03)00275-2. 2.1

[27] R. N. Mohapatra et al. Theory of neutrinos: A white paper. *Rept. Prog. Phys.*, 70:1757–1867, 2007. doi: 10.1088/0034-4885/70/11/R02.

[28] S. Pascoli, S. T. Petcov, and T. Schwetz. The Absolute Neutrino Mass Scale, Neutrino Mass Spectrum, Majorana CP-Violation and Neutrinoless Double-Beta Decay. *Nucl. Phys.*, B734:24–49, 2006. doi: 10.1016/j.nuclphysb.2005.11.003. 2.1

[29] D.Y. Akimov. Experimental Methods for Particle Dark Matter Detection (Review). *Instruments and Experimental Techniques*, 44(5):575–617, 2001. 2.1

[30] R.J. Gaitskell. Direct detection of dark matter. 2004. 2.1

[31] JR Primack, D. Seckel, and B. Sadoulet. Detection of cosmic dark matter. *Annual Review of Nuclear and Particle Science*, 38(1):751–807, 1988. 2.1

[32] PF Smith and JD Lewin. Dark matter detection. *Physics Reports*, 187: 203–280, 1990. 2.1, 2.2.5, 2.2.5, 5.3

[33] R. Bernabei, P. Belli, R. Cerulli, F. Montecchia, M. Amato, A. Incicchitti, D. Prosperi, CJ Dai, HL He, HH Kuang, et al. Investigating the DAMA annual modulation data in the framework of inelastic dark matter. *The European Physical Journal C-Particles and Fields*, 23(1):61–64, 2002. 1

[34] M. Goeppert-Mayer. Double beta-disintegration. *Physical Review*, 48(6): 512–516, 1935. 2.2.1

[35] P. Vogel and P. Fisher. Nuclear structure and double beta decay: Two neutrino mode. *Physical Review C*, 32(4):1362–1368, 1985. 2.2.1

[36] WH Furry. On transition probabilities in double beta-disintegration. *Physical Review*, 56(12):1184–1193, 1939. 2.2.1

[37] S. Umehara, T. Kishimoto, I. Ogawa, H. Miyawaki, K. Matsuoka, K. Kishimoto, A. Katsuki, H. Sakai, D. Yokoyama, K. Mukaida, et al. Neutrino-less double-beta decay of 48Ca studied by CaF2(Eu) scintillators. *Name: Physical Review. C, Nuclear Physics*, 78(5), 2008. 2.2

[38] HV Klapdor-Kleingrothaus, A. Dietz, L. Baudis, G. Heusser, IV Krivosheina, B. Majorovits, H. Paes, H. Strecker, V. Alexeev, A. Balysh, et al. Latest results from the Heidelberg-Moscow double beta decay experiment. *The European Physical Journal A*, 12(2):147–154, 2001. 2.2

[39] D. Gonzales et al. Current IGEX results for Neutrinoless Double-Beta Decay of Ge-76. *Nuclear Physics B*, 87(1):278–280, 2000. 2.2

[40] NEMO Collaboration: Arnold R. et al. First results of the search for neutrinoless double-beta decay with the NEMO 3 detector. *Physical review letters*, 95(18):182302, 2005. 2.2

[41] NEMO Collaboration: Arnold R. et al. Double beta decay of Zr-96. *Nucl. Phys., A*, 658:299–312, 1999. 2.2

[42] FA Danevich, A.S. Georgadze, VV Kobychev, BN Kropivyansky, AS Nikolaiko, OA Ponkratenko, VI Tretyak, S.Y. Zdesenko, Y.G. Zdesenko, PG Bizzeti, et al. Search for 2-beta decay of cadmium and tungsten isotopes: Final results of the Solotvina experiment. *Physical Review C*, 68(3): 35501, 2003. 2.2

[43] C. Arnaboldi, DR Artusa, FT Avignone, et al. First results on neutrinoless double beta decay of 130Te with the calorimetric CUORICINO experiment. *Physics Letters B*, 584(3-4):260–268, 2004. 2.2

[44] R. Bernabei, P. Belli, F. Cappella, R. Cerulli, F. Montecchia, A. Incicchitti, D. Prosperi, and CJ Dai. Investigation of beta-beta decay modes in 134Xe and 136Xe. *Physics Letters B*, 546(1-2):23–28, 2002. 2.2

[45] NEMO Collaboration: Argyriades J. et al. Measurement of the double-beta decay half-life of 150Nd and search for neutrinoless decay modes with the NEMO-3 detector. *Physical Review C*, 80(3):32501, 2009. 2.2

[46] E. Opik. Selective absorption of light in space, and the dynamics of the Universe. *Bull. de la Soc. Astr. de Russie*, 21:150, 1915. 2.2.3

[47] F. Zwicky. Die rotverschiebung von extragalaktischen nebeln. *Helvetica Physica Acta*, 6:110–127, 1933. 2.2.3

[48] D. Mihalas and PM Routly. Galactic astronomy (A Series of Books in Astronomy and Astrophysics, San Francisco, 1968. 2.2.3

[49] CL Bennett, M. Halpern, G. Hinshaw, N. Jarosik, A. Kogut, M. Limon, SS Meyer, L. Page, DN Spergel, GS Tucker, et al. First-year Wilkinson Microwave Anisotropy Probe (WMAP) observations: preliminary maps and basic results. *The Astrophysical Journal Supplement Series*, 148:1, 2003. 2.2.3, 2.2.4

[50] C. Hagmann, D. Kinion, W. Stoeffl, K. Van Bibber, E. Daw, H. Peng, L.J. Rosenberg, J. LaVeigne, P. Sikivie, NS Sullivan, et al. Results from a high-sensitivity search for cosmic axions. *Physical Review Letters*, 80(10):2043–2046, 1998. 2.2.4

[51] E.W. Kolb, D.J.H. Chung, and A. Riotto. WIMPzillas! *Arxiv preprint hep-ph/9810361*, 1998. 2.2.4

[52] G. Servant and T.M.P. Tait. Is the lightest Kaluza-Klein particle a viable dark matter candidate? *Nuclear Physics B*, 650(1-2):391–419, 2003. 2.2.4

[53] C. Boehm and P. Fayet. Scalar dark matter candidates. *Nuclear Physics B*, 683(1-2):219–263, 2004. 2.2.4

[54] G. Bertone, D. Hooper, and J. Silk. Particle dark matter: evidence, candidates and constraints. *Physics Reports*, 405(5-6):279–390, 2005. 2.2.4

[55] A. Kurylov and M. Kamionkowski. Generalized analysis of the direct weakly interacting massive particle searches. *Physical Review D*, 69(6):63503, 2004. 2.2.5

[56] R. Silberberg, CH Tsao, and AF Barghouty. Updated partial cross sections of proton-nucleus reactions. *The Astrophysical Journal*, 501:911–919, 1998. 2.3

[57] PD Martoff et al. COSMO-a program to estimate spallation radioactivity produced in a pure substance by exposure to cosmic radiation on the earth. *Computer Physics Communications*, 72(1):96–103, 1992. 2.3

[58] A. Alessandrello, C. Brofferio, DV Camin, O. Cremonesi, E. Fiorini, G. Gervasio, A. Giuliani, M. Pavan, G. Pessina, E. Previtali, et al. A search for neutrinoless double beta decay of 130Te with a bolometric detector. *Nuclear Physics B-Proceedings Supplements*, 28(1):229–232, 1992. 2.3

[59] J. Amaré, B. Beltrán, JM Carmona, S. Cebrián, E. García, H. Gómez, IG Irastorza, G. Luzón, M. Martínez, J. Morales, et al. Dark matter searches with NaI scintillators in the Canfranc underground laboratory: ANAIS experiment. In *Journal of Physics: Conference Series*, volume 39, page 123. IOP Publishing, 2006. 2.3

[60] M. Wójcik, W. Wlazo, G. Zuzel, and G. Heusser. Radon diffusion through polymer membranes used in the solar neutrino experiment Borexino. *Nuclear Instruments and Methods in Physics Research Section A: Accelerators, Spectrometers, Detectors and Associated Equipment*, 449(1-2):158–171, 2000. 2.3.2

[61] C. Bucci, S. Capelli, M. Carrettoni, M. Clemenza, O. Cremonesi, L. Gironi, P. Gorla, C. Maiano, A. Nucciotti, L. Pattavina, et al. Background study and Monte Carlo simulations for large-mass bolometers. *The European Physical Journal A*, 41(2):155–168, 2009. 2.4.1

[62] D. Budjás, M. Heisel, W. Maneschg, and H. Simgen. Optimisation of the MC-model of a p-type Ge-spectrometer for the purpose of efficiency determination. *Applied Radiation and Isotopes*, 67(5):706–710, 2009. 2.4.1

[63] M. Laubenstein, M. Hult, J. Gasparro, D. Arnold, S. Neumaier, G. Heusser, M. Köhler, P. Povinec, J.L. Reyss, M. Schwaiger, et al. Underground measurements of radioactivity. *Applied Radiation and Isotopes*, 61(2-3):167–172, 2004. 2.4.1

[64] JA Simpson. Introduction to the galactic cosmic radiation. *Composition and origin of cosmic rays*, 1983. 2.4.2

[65] A. Bettini. Underground laboratories. In *Journal of Physics: Conference Series*, volume 120, page 082001. Institute of Physics Publishing, 2008. 2.4.2

[66] E. Fiorini and TO Niinikoski. Low-temperature calorimetry for rare decays. *Nuclear Instruments and Methods in Physics Research*, 224(1-2):83–88, 1984. 3.1

[67] E. Previtali. 20 years of cryogenic particle detectors: past, present and future. *Nuclear Physics B-Proceedings Supplements*, 150:3–8, 2006. 3.1

[68] C. Arnaboldi, DR Artusa, FT Avignone, et al. First results on neutrinoless double beta decay of 130Te with the calorimetric CUORICINO experiment. *Physics Letters B*, 584(3-4):260–268, 2004. 3.1, 4

[69] A. Benoit, L. Berge, A. Broniatowski, B. Chambon, M. Chapellier, G. Chardin, P. Charvin, M. De Jesus, P. Di Stefano, D. Drain, et al. First results of the EDELWEISS WIMP search using a 320 g heat-and-ionization Ge detector. *Physics Letters B*, 513(1-2):15–22, 2001. 3.1, 5

[70] DS Akerib, J. Alvaro-Dean, MS Armel, MJ Attisha, L. Baudis, DA Bauer, AI Bolozdynya, PL Brink, R. Bunker, B. Cabrera, et al. New results from the cryogenic dark matter search experiment. *Physical Review D*, 68(8): 82002, 2003. 3.1

[71] M. Altmann, G. Angloher, M. Bruckmayer, C. Bucci, S. Cooper, C. Cozzini, P. DiStefano, F. Von Feilitzsch, T. Frank, D. Hauff, et al. Results and plans of the CRESST dark matter search. *Arxiv preprint astro-ph/0106314*, 2001. 3.1

[72] SH Moseley, JC Mather, and D. McCammon. Thermal detectors as x-ray spectrometers. *Journal of Applied Physics*, 56:1257, 1984. 3.1.1

[73] NF Mott and JH Davies. Metal-insulator transition in doped semiconductors. *Philosophical Magazine Part B*, 42(6):845–858, 1980. 3.1.2

[74] A. Miller and E. Abrahams. Impurity conduction at low concentrations. *Physical Review*, 120(3):745–755, 1960. 3.1.2

[75] E.W. Hoppe, A. Seifert, C.E. Aalseth, P.P. Bachelor, A.R. Day, D.J. Edwards, T.W. Hossbach, K.E. Litke, J.I. McIntyre, H.S. Miley, et al. Cleaning and passivation of copper surfaces to remove surface radioactivity and prevent oxide formation. *Nuclear Instruments and Methods in Physics Research-Section A*, 579(1):486–489, 2007. 3.2

[76] Wikipedia. Electrowinning, June 2010. http://en.wikipedia.org/wiki/Electrowinning. 3.2.1

[77] M. Clemenza. Ultra-sensitive naa measurement of th232 in copper. In *LRT2010*, August 2010. 3.1

[78] E.W. Hoppe. Reductions of radioactive backgrounds in ultra-high purity electroformed copper. In *LRT2010*, August 2010. 3.1

[79] R. MacLellan. Naa techniques and applications. In *LRT2010*, August 2010. 3.1

[80] A. Ng and C. Patterson. Natural concentrations of lead in ancient Arctic and Antarctic ice. *Geochimica et Cosmochimica Acta*, 45(11):2109–2121, 1981. 3.3, 4.6.6

[81] FB Ribeiro. A general solution for the diffusion of a radioactive isotope in homogeneous and isotopic solids. *Radiation Measurements*, 26(5):747–750, 1996. 3.3, 4.6.4

[82] E. Fiorini and TO Niinikoski. Low-temperature calorimetry for rare decays. *Nuclear Instruments and Methods in Physics Research*, 224(1-2):83–88, 1984. 4

[83] A. Alessandrello, C. Brofferio, DV Camin, O. Cremonesi, E. Fiorini, E. García, A. Giuliani, P. De Marcillac, A. Nucciotti, M. Pavan, et al. A new search for neutrinoless [beta][beta] decay with a thermal detector. *Physics Letters B*, 335(3-4):519–525, 1994. 4

[84] C. Arnaboldi, C. Brofferio, C. Bucci, S. Capelli, O. Cremonesi, E. Fiorini, A. Giuliani, A. Nucciotti, M. Pavan, M. Pedretti, et al. A calorimetric search on double beta decay of 130Te. *Physics Letters B*, 557(3-4):167–175, 2003. 4

[85] C. Arnaboldi, DR Artusa, FT Avignone III, M. Balata, I. Bandac, M. Barucci, JW Beeman, C. Brofferio, C. Bucci, S. Capelli, et al. A New Limit on the Neutrinoless DBD of 130Te. *Arxiv preprint hep-ex/0501034*, 2005. 4

[86] M. Pavan. Introduction to double beta decay experiments and CUORE. In *Neutrino 2010*, 2010. 4

[87] SP Ahlen, M. Ambrosio, G. Auriemma, A. Baldini, GC Barbarino, B. Barish, G. Battistoni, R. Bellotti, C. Bemporad, P. Bernardini, et al. Study of penetrating cosmic ray muons and search for large scale anisotropies at the Gran Sasso Laboratory. *Physics Letters B*, 249:149–156, 1990. 4.1

[88] P. Belli, R. Bernabei, S. d'Angelo, MP de Pascale, L. Paoluzi, R. Santonico, N. Taborgna, N. Iucci, and G. Villoresi. Deep underground neutron flux measurement with large BF 3 counters. *Il Nuovo Cimento A (1971-1996)*, 101(6):959–966, 1989. 4.1

[89] C. Arnaboldi, C. Bucci, S. Capelli, P. Gorla, E. Guardincerri, A. Nucciotti, G. Pessina, S. Pirro, and M. Sisti. The temperature stabilization system of CUORICINO: An array of macro bolometers. *IEEE Transactions On Nuclear Science*, 52(5), 2005. 4.1

[90] C. Arnaboldi, G. Pessina, E. Previtali, D.F. della Bicocca, I.N. di Fisica Nucleare, and I. Milano. A programmable calibrating pulse generator with multi-outputs and very high stability. *IEEE Transactions on Nuclear Science*, 50(4 Part 1):979–986, 2003. 4.1

[91] C. Arnaboldi, C. Brofferio, A. Bryant, C. Bucci, L. Canonica, S. Capelli, M. Carrettoni, M. Clemenza, I. Dafinei, S. Di Domizio, et al. Production of high purity TeO2 single crystals for the study of neutrinoless double beta decay. *Arxiv preprint arXiv:1005.3686*, 2010. 4.1

[92] A. Alessandrello, C. Arpesella, C. Brofferio, C. Bucci, C. Cattadori, O. Cremonesi, E. Fiorini, A. Giuliani, S. Latorre, A. Nucciotti, et al. Measurements of internal radioactive contamination in samples of Roman lead to be used in experiments on rare events. *Nuclear Instruments and Methods in Physics Research Section B: Beam Interactions with Materials and Atoms*, 142(1-2): 163–172, 1998. 4.1

[93] G. Heusser. Low-radioactivity background techniques. *Annual Review of Nuclear and Particle Science*, 45(1):543–590, 1995. 4.1

[94] GL Fogli, E. Lisi, and AM Rotunno. Probing particle and nuclear physics models of neutrinoless double beta decay with different nuclei. *Physical Review D*, 80(1):15024, 2009. 4.2

[95] M. Pedretti, C. Arnaboldi, M. Barucci, C. Brofferio, C. Bucci, S. Capelli, O. Cremonesi, A. Giuliani, P. Gorla, A. Nucciotti, et al. Measurement of thermal properties for modeling and optimization of large mass bolometers. *Physica B: Condensed Matter*, 329:1614–1615, 2003. 4.3

[96] F. Šimkovic, A. Faessler, V. Rodin, P. Vogel, and J. Engel. Anatomy of the $0\nu\beta\beta$ nuclear matrix elements. *Physical Review C*, 77(4):45503, 2008. 4.4

[97] O. Civitarese and J. Suhonen. Nuclear matrix elements for double beta decay in the QRPA approach: A critical review. In *Journal of Physics: Conference Series*, volume 173, page 012012. IOP Publishing, 2009.

[98] J. Menéndez, A. Poves, E. Caurier, and F. Nowacki. Disassembling the nuclear matrix elements of the neutrinoless $\beta\beta$ decay. *Nuclear Physics A*, 818(3-4):139–151, 2009.

[99] J. Barea and F. Iachello. Neutrinoless double-β decay in the microscopic interacting boson model. *Physical Review C*, 79(4):44301, 2009. 4.4

[100] C. Bradaschia, R. Del Fabbro, A. Di Virgilio, A. Giazotto, H. Kautzky, V. Montelatici, A. Passuello, et al. The VIRGO Project: A wide band antenna for gravitational wave detection* 1. *Nuclear Instruments and Methods in Physics Research Section A: Accelerators, Spectrometers, Detectors and Associated Equipment*, 289(3):518–525, 1990. 4.5.2

[101] A. Benoit, L. Berge, A. Broniatowski, L. Chabert, B. Chambon, M. Chapellier, G. Chardin, P. Charvin, M. De Jesus, P. Di Stefano, et al. Improved exclusion limits from the edelweiss wimp search. *Physics Letters B*, 545(1-2): 43–49, 2002. 5

[102] PCF Di Stefano, A. Benoit, L. Bergé, J. Blumer, A. Broniatowski, B. Censier, L. Chabert, B. Chambon, M. Chapellier, G. Chardin, et al. EDELWEISS dark matter search update. *New Astronomy Reviews*, 49(2-6):251–254, 2005. 5

[103] J. Lindhard, M. Scharff, and HE Schiøtt. Range concepts and heavy ion ranges (Notes on atomic collisions, II). *Name: Kgl. Danske Videnskab. Selskab. Mat. Fys. Medd*, 1963. 5.1, 5.1.3

[104] A. Benoit, L. Bergé, J. Blümer, A. Broniatowski, B. Censier, A. Chantelauze, M. Chapellier, G. Chardin, S. Collin, X. Defay, et al. Measurement of the response of heat-and-ionization germanium detectors to nuclear recoils. *Nuclear Instruments and Methods in Physics Research Section A: Accelerators, Spectrometers, Detectors and Associated Equipment*, 577(3):558–568, 2007. 5.1, 5.1.3, 5.1.3

[105] Knoll G.F. Radiation detection measurement, 1989. 5.1.1

[106] A. Broniatowski. A simulation code for the ionization and heat signals in low-temperature germanium detectors for Dark Matter research. *Nuclear Instruments and Methods in Physics Research Section A: Accelerators, Spectrometers, Detectors and Associated Equipment*, 520(1-3):178–181, 2004. 5.1.1

[107] B. Censier, A. Broniatowski, A. Juillard, L. Berge, and L. Dumoulin. Surface trapping and detector degradation in Ge bolometers for the EDELWEISS Dark Matter search: experiment and simulation. *Nuclear Instruments and Methods in Physics Research Section A: Accelerators, Spectrometers, Detectors and Associated Equipment*, 520(1-3):156–158, 2004. 5.1.1

[108] A. Benoit, L. Berge, A. Broniatowski, B. Chambon, M. Chapellier, G. Chardin, P. Charvin, M. De Jesus, P. Di Stefano, D. Drain, et al. Event categories in the EDELWEISS WIMP search experiment. *Physics Letters B*, 479(1-3):8–14, 2000. 5.1.1

[109] T. Shutt, J. Emes, EE Haller, J. Hellmig, B. Sadoulet, D. Seitz, BA Young, and S. White. A solution to the dead-layer problem in ionization and phonon-based dark matter detectors. *Nuclear Instruments and Methods in Physics Research Section A: Accelerators, Spectrometers, Detectors and Associated Equipment*, 444(1-2):340–344, 2000. 5.1.1

[110] B. Neganov and V. Trofimov. USSR patent No 1037771. *Otkrytia i izobreteniya*, 146:215, 1985. 5.1.2

[111] P.N. Luke. Low noise germanium radial drift detector. *Nuclear Instruments and Methods in Physics Research Section A: Accelerators, Spectrometers, Detectors and Associated Equipment*, 271(3):567–570, 1988. 5.1.2

[112] A. Juillard. *Résolution dans des bolomètres équipés de couches minces d'isolant d'Anderson pour des événements impliquant des reculs de noyaux.* PhD thesis, Université Paris XI, France, 1999. 5.1.2.1

[113] S. Marineros. *Couches minces d'isolant d'Anderson. Application à la bolométrie à très basse température.* PhD thesis, Université Paris XI, France, 1998. 5.1.2.1

[114] X. Defay. *Recherche de matière noire au sein de lexpérience EDELWEISS avec des bolomètres germanium à double composante Ionisation/Chaleur, rejet des évènements de surface avec la voie ionisation.* PhD thesis, Université Montpellier II, France, 2008. 5.1.2.2

[115] A. Broniatowski, X. Defay, E. Armengaud, L. Berge, A. Benoit, O. Besida, J. Blumer, A. Chantelauze, M. Chapellier, G. Chardin, et al. A new high-background-rejection dark matter Ge cryogenic detector. *Physics Letters B*, 681(200):305–09, 2009. 5.1.2.2, 5.4.2

[116] O. Martineau, A. Benoīt, L. Bergé, A. Broniatowski, L. Chabert, B. Chambon, M. Chapellier, G. Chardin, P. Charvin, M. De Jésus, et al. Calibration of the EDELWEISS cryogenic heat-and-ionization germanium detectors for dark matter search. *Nuclear Instruments and Methods in Physics Research Section A: Accelerators, Spectrometers, Detectors and Associated Equipment*, 530(3):426–439, 2004. 5.1.3

[117] S. Fiorucci. *Acquisition et analyse des données pour lexpérience de recherche de matière noire EDELWEISS.* PhD thesis, Université Paris XI, France, 2005. 5.1.4

[118] M. L'Hour and E. Veyrat. A mid-15th century clinker boat off the north coast of France, the Aber Wrac'h I wreck: A preliminary report. *International Journal of Nautical Archaeology*, 18(4):285–298, 1989. 5.2.0.2

[119] L. Chabert. *Étude du bruit de fond neutron induit par les muons dans lexpérience EDELWEISS-II.* PhD thesis, Université Lyon I, France, 2004. 5.2.0.2

[120] S. Yellin. Finding an upper limit in the presence of an unknown background. *Physical Review D*, 66(3):32005, 2002. 5.3

NOM : PATTAVINA Prénoms : Luca	DATE de SOUTENANCE 17 janvier 2011

TITRE : Radon-induced surface contaminations in neutrinoless double beta decay and dark matter experiments

Numéro d'ordre : 27-2011

DIPLOME DE DOCT.	DOCTEUR-INGENIEUR	DOCTORAT D'ETAT	DOCTORAT DE 3e CYCLE	Spécialité : Physics and Astronomy
X	☐	☐	☐	

Cote B.I.U. – Lyon : T 50/210/19 / et bis	CLASSE :

RESUME :

In experiments looking for rare events, like neutrinoless double beta decay (DBD0v) and dark matter search (DM), one of the main issues is to increase the experimental sensitivity through the material selection and production. In the specific the background contribution coming from the materials used for the detector realization has to be minimized. Moreover the net reduction of the background produced by the bulk part of the apparatus has raised concerns about the background contribution coming from the surfaces.
Many procedures and techniques were developed during the last years in order to remove and to minimize the presence of possible contaminants on detector surfaces. To succeed in this strategy a big effort was put in defining all possible mechanisms that lead to surface contaminations, as well as specific cleaning procedures, which are able to reduce and control the surface radioactivity.
The presence in air and gases of possible radioactive elements that can stick on the detector surfaces can lead to a recontamination process that will vanish all the applied cleaning procedures.
Here is presented and analyzed the contribution to the background of rare events experiments like CUORE (DBD0v) and EDELWEISS (DM) produced by an exposure of their detector components to a big activity of ^{222}Rn, radioactive daughter isotope from the ^{238}U chain.

MOTS-CLES : Double beta decay, dark matter, low background, surface contaminations, Radon

Directeurs de recherches : E. Previtali et C. Augier

Composition du jury : F. Piquemal – C. Bucci – S. Ragazzi – B. Ille	172 pages